Chemical Engineering Journal 489 (2024) 151016

Contents lists available at ScienceDirect

Chemical Engineering Journal

journal homepage: www.elsevier.com/locate/cej

Three-dimensional measurement method of binary particle collisions under dry and wet conditions

Falk Bunke *, Swantje Pietsch-Braune, Stefan Heinrich

Institute of Solids Process Engineering and Particle Technology, Hamburg University of Technology, Denickestraße 15, 21073 Hamburg, Germany

ARTICLE INFO

Keywords:
Restitution coefficient
Binary particle collision
Liquid layer
Rotation measurement
Agglomeration

ABSTRACT

The description, calculation and design of solids processes, such as fluidization, pneumatic conveying or mixing, require knowledge of collision dynamics between particles and apparatus walls or interparticle collisions without, but often also with the presence of an additional liquid. For the study of such dry and wet interparticle collisions, an experimental setup is presented that allows the performance of dry or wet free binary collisions of spherical particles down to a minimum diameter of 1 mm. The recording of the particle motions in all three spatial directions is provided by two synchronized highspeed cameras. Methods and algorithms are presented for analyzing the translational and rotational motion in three-dimensional space, as well as for measuring the amount of liquid on the particles in the case of wet collisions. Motion data from dry collisions between equal sized and unequal sized spherical particles are compared with a three-parameter collision model. In addition, a first series of measurements of wetted collisions is used to compare the collision dynamics with dry collisions.

1. Introduction

Many processes in the chemical, pharmaceutical or food industry, such as fluidization, pneumatic conveying or mixing, handle granular or particulate solids. These processes are characterized by particle–wall and interparticle collisions. Thus, the knowledge of collision dynamics is necessary for their calculation, design and modeling. In many cases, like during fluidized bed spray agglomeration, an additional fluid is added to the process, which significantly influences the collision behavior [1]. In wetted collisions, additional viscous and capillary forces induced by the liquid occur. If these mostly attractive forces dominate the recoil forces of the collision, liquid-induced agglomeration of the collision partners occurs. The extent of agglomeration in the process influences the further transport properties of the material, as well as the product properties, quality and morphology. Unintentional agglomeration in processes can also lead to blockages and thus to unplanned downtimes. Even from these few selected examples, the importance of understanding and describing the collision dynamics of both dry and wet collisions becomes clear.

Experimental collision studies under dry conditions have usually been carried out in two different ways. The first variant works with one moving collision partner, i.e. a spherical or aspherical particle or a round disk, and a fixed static collision partner, often a flat plate or bar [2–32]. In some cases, additional forms were applied to the static part [33,34]. In this way, particle–wall collisions could be examined in detail. In the second variant, particle–particle collisions are realized by two moving collision partners. Again, a distinction can be made between free and guided interparticle collisions. Guided collisions are characterized by the fact that the movement of the involved collision partners is restricted or influenced by additional guide devices and additional forces that do not occur in free collisions. A guided method that is often used is the Newtons cradle or pendulum [35–44], the advantage of which lies in the very low collision speeds that can be achieved [2]. In contrast, other guided approaches, like collisions inside a tube with a diameter slightly larger than that of the particles [45] or striking a particle resting on a holder with another particle [46], were used less frequently. Free collisions [34,47–49] have so far only rarely been carried out due to the high demands on the accuracy of the experimental setup and the high effort, although this type of investigation allows all degrees of freedom of movement and thus depicts real particle movements in apparatuses as realistically as possible. This advantage has not yet been fully exploited, since the free collisions were recorded with only one camera so far, which means that only a two-dimensional measurement is possible. The apparatus therefore had to be adjusted very precisely to ensure that the collision took place in the image plane. A measurement of the movement in the direction of the image depth or a direct check of the collision plane

* Corresponding author.
E-mail address: falk.bunke@tuhh.de (F. Bunke).

https://doi.org/10.1016/j.cej.2024.151016
Received 15 September 2023; Received in revised form 18 March 2024; Accepted 3 April 2024
Available online 5 April 2024

was therefore not possible. Furthermore, free collisions were performed between collision partners of the same size and under dry conditions exclusively. In contrast, particle–wall collisions [50–68] and interparticle pendulum experiments [69–75] have already been executed under wet conditions.

This work aims at eliminating the disadvantages of free collision investigations by means of an extended experimental setup. This includes firstly the extension of free collisions to binary collisions of spherical particles of the same and different diameters, where one or both particles can be dry or wet before the collision. Secondly, the use of two highspeed cameras enables the recording of particle motions in all three spatial directions. Last but not least, the minimum investigable particle diameter will be strongly reduced from 3 mm [48] to 1 mm compared to the free collision experiments performed so far. This offers much better investigation possibilities for e.g. agglomeration processes in the future as these processes often include particles smaller than 3 mm in industrial applications. In this work, special attention is paid to the analysis methods of the particle motion on the basis of the camera images. Up to now, this topic has only been analyzed and evaluated to a limited extent in this kind of collision experiments, despite its high relevance for ensuring reliable measurement data. In particular, additional liquid on the particles as well as previously unknown directions of rotation of the particles in three-dimensional space creates new challenges for the measurement of collision data and conditions, which are considered in detail. With the methods presented in this work, it is possible to measure the translational and rotational motion in all three spatial directions from the camera images with high precision, as well as the amount of liquid on wetted particles. The correct function of the presented methods of digital image analysis is proven by means of real comparative experiments and artificially created test image sequences. The combination of an extended experimental setup and strong image analysis methods allows a realistic reconstruction and measurement of binary interparticle collisions in apparatuses and processing plants.

The comparison of dry collisions of equal sized and unequal sized particles with the model of hard spheres according to Walton [76,77] confirms a valid prediction of the collision dynamics of the model for dry collisions. First series of measurements of wetted collisions between equal sized particles allow a direct comparison of the collision dynamics with the dry experiments.

2. Experimental setup

The setup is schematically shown in Fig. 1 and basically consists of the same two main parts as described by Labous et al. [49]. The collision unit generates the binary particle collision while the recording unit detects it.

The collision unit in turn consists of two main components: a vacuum tweezer connected to a vacuum pump and a particle accelerator driven by compressed air. The vacuum tweezer consists of a metal tube with a much smaller inner diameter than the particles to be measured. It holds a particle pointing downwards at its tip through the applied vacuum and is positioned above the particle accelerator. When a solenoid valve is actuated, the connection to the vacuum pump is interrupted and a slight overpressure is applied, which causes the particle to fall. The particle accelerator also consists of a metal tube, which has a slightly smaller diameter than the particle to be measured. The particle rests on the tip of the particle accelerator until a solenoid valve is actuated, which triggers a short blast of compressed air. This accelerates the particle upwards and towards the other particle dropped by the vacuum tweezer. In the case of a dry collision, the particles describe a ballistic trajectory after launch until they collide in the detection range of the recording unit. In the case of a wet collision, a so-called liquid ring is placed between the vacuum tweezer or particle accelerator and the collision zone. The liquid ring consists of a copper wire that is bent into a ring. Before starting the experiment, this ring is immersed in a liquid bath containing the liquid with which the particle is to be coated. The ring is then removed from

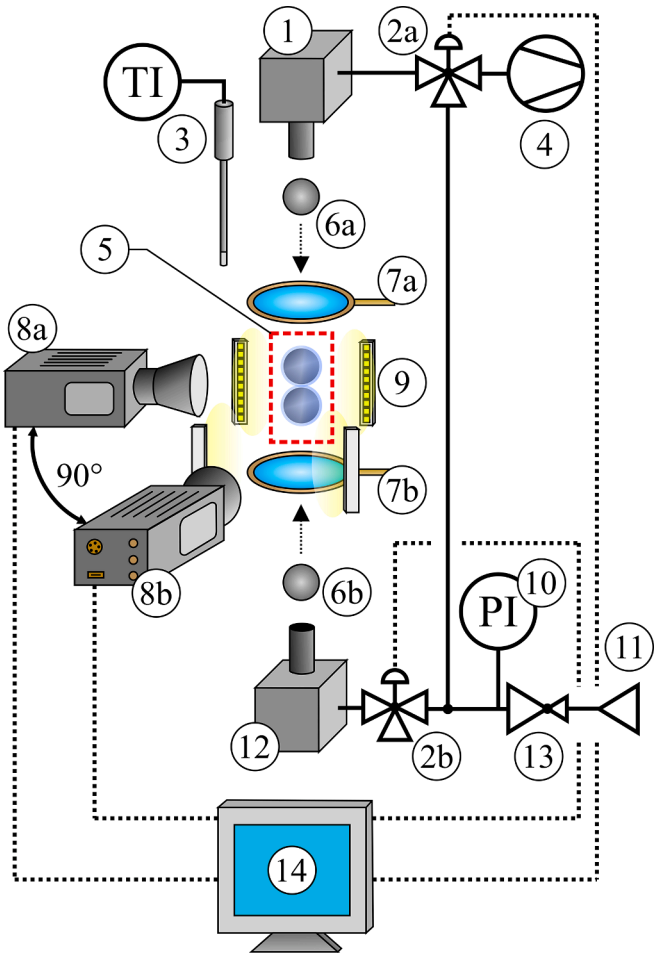

Fig. 1. Schematic of the experimental setup. 1) Vacuum tweezer; 2) Solenoid valve; 3) Temperature indicator; 4) Vacuum pump; 5) Collision zone; 6) Particle; 7) Optional liquid ring; 8) Highspeed camera; 9) LED illumination system; 10) Pressure indicator; 11) Compressed air source; 12) Particle accelerator; 13) Pressure regulator; 14) Control system.

the liquid bath, creating a liquid film inside the ring, similar to a soap bubble ring. During the experiment, the particle passes through the center of the ring and thus through the liquid film. The liquid ring and the wetting process are shown in Fig. 2. After the particle has completely passed through the liquid film of the ring, the liquid around the particle forms an almost ideal sphere after a short time due to the free fall and the low air resistance caused by the low velocities. As a result, the particle is coated completely with liquid before the particles collide. It must be mentioned that it cannot be verified that the particle is in the center of the liquid and therefore has an exactly uniform liquid film. This is because the liquid used does not form a sufficiently thick layer around the particle so that a distinct liquid layer is directly visible around the particle. The non-visibility of the liquid layer is in turn due to light refraction or lens effects that distort perception through the spherical liquid layer. These distortion effects will be discussed in more detail later. This wetting technique has already been successfully applied in the investigation of wetted particle–wall collisions by Buck et al. [52]. In their study it was also not possible to prove that the wetting is homogeneous. However, the results of the investigation of Buck et al. [52] do not clearly indicate inhomogeneous wetting. Therefore, homogeneous wetting is also assumed in this study.

In order to control and detect the collisions, precise positioning of the collision unit components and exact timing of the valve opening sequences are necessary. The solenoid valves in the collision unit are coordinated via a real-time control module, which makes it possible to

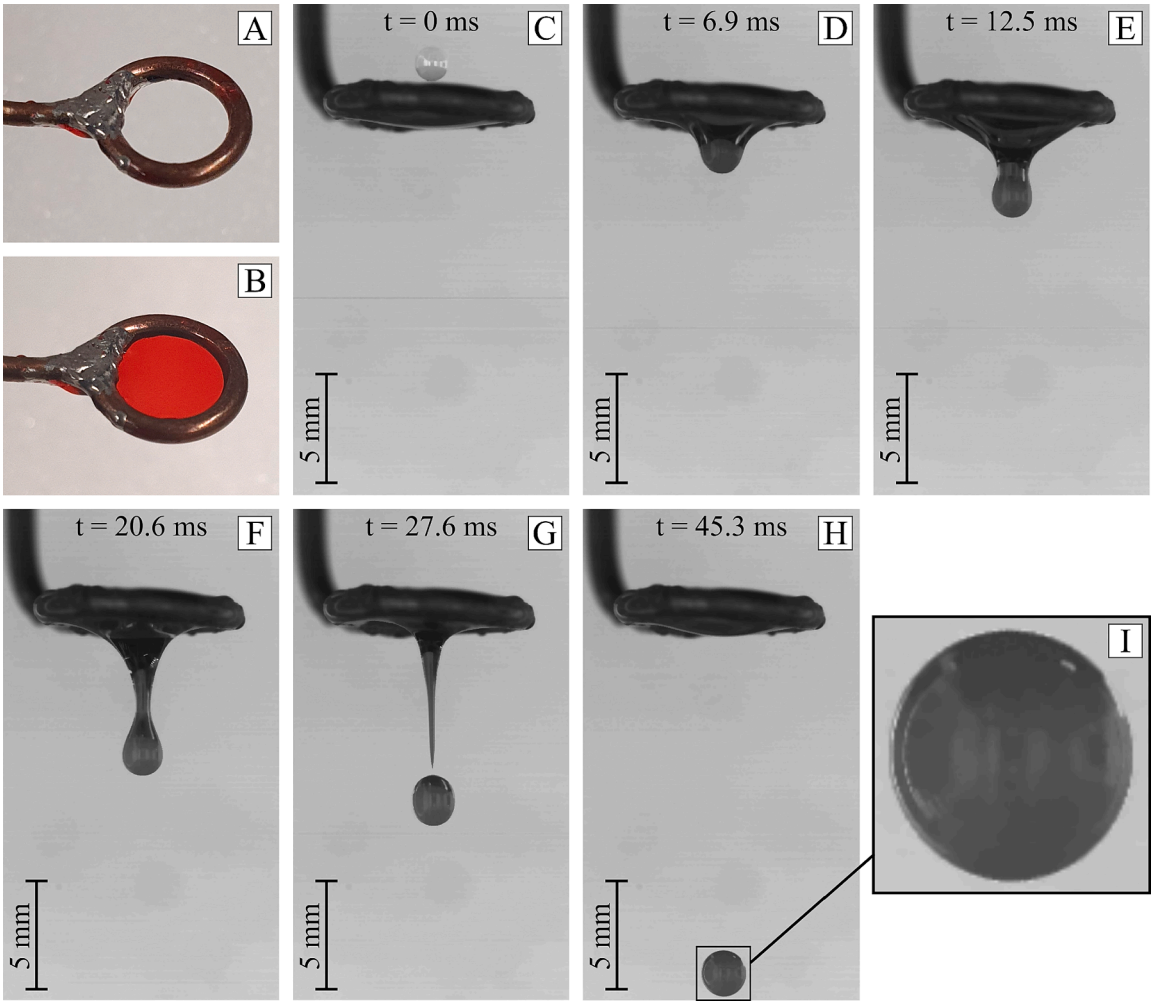

Fig. 2. Wetting procedure of a 1.5 mm ZrO_2 sphere with red colored liquid. A: Copper wire ring - empty liquid ring. B: Filled ring with red colored liquid. C-H: Grayscale highspeed camera image sequence of the wetting process. I: Close-up of the wet particle. (For interpretation of the references to color in this figure legend, the reader is referred to the web version of this article.)

program the sequence of valve activations, the time delay between activations and the duration of valve opening. For exact positioning, both the vacuum tweezers and the particle accelerator are each mounted on a positioning unit. Each unit consists of a micro positioning cross slide, which allows horizontal positioning along both horizontal axes, and three rotary tables, each allowing rotation around one of the three spatial axes. For the adjustment of the vertical position, both positioning units are mounted on a one meter long double leadscrew linear slide. This linear slide has two platforms, each of which can be moved separately by its own lead screw. This allows the distance between the vacuum tweezer and the particle accelerator to be adjusted, as well as their vertical position relative to the recording unit. The vertical distance of the vacuum tweezer from the collision zone determines the collision velocity of the dropped particle. The velocity of the particle shot by the particle accelerator can in turn be adjusted by the applied air pressure, which is set using a manual pressure reducer and can be checked by a digital barometer.

This collision unit enables high reliability in realizing a collision, especially for dry collisions. Even in dry collisions, slight fluctuations in the contact point of the particles can occur. Complete failed attempts due to missing particles are rare. As a rough estimate, a hit probability of 98 % can be assumed with a well-adjusted setup. In wetted collision experiments, the reliability of realizing a collision is still high, but lower than in dry collisions. It can happen more often that the particles miss each other with the same setup settings. The range of fluctuation of the contact point of wetted collisions is also slightly higher. This is due to the wetting process of the particles. When the particle passes through the liquid ring, the liquid exerts additional forces on the particle that can change its trajectory. To reduce this influence, the liquid ring needs to be precisely aligned so that the particle passes through the liquid film in the ring centrally and orthogonally.

The recording unit essentially consists of two highspeed cameras, the illumination system and the recording background. The cameras are positioned 90° offset on the horizontal plane, which enables a three-dimensional capture of the collision. The used cameras are a Series Y-4 camera and a Series NX-4 camera (Imaging Solutions GmbH, Germany). They allow the capture of monochrome images only. Both are equipped with a macro lens with 105 mm focal length from the company Sigma (Sigma Macro 105 mm F2.8 EX DG OS HSM). The cameras are synchronized and record at 5100 frames per second at a resolution of 576 x 1024 pixels (Y-4 series) and 400 x 1024 pixels (NX-4 series), respectively. In the collision plane of the Y-4 camera, the length of one pixel corresponds to a real length of 20.62 µm. Since the NX-4 camera is slightly further away from the collision plane due to the design of the experimental setup, the length of one pixel in this camera corresponds to a higher real length of 27.28 µm. A review of the influence of lens distortion using a checkerboard showed that it is negligible over the entire image area in both cameras. To prevent motion blur, the exposure time is kept low at 72 ms. Due to the large focal length of the lenses, the depth of sharpness is very narrow. By keeping the aperture as small as

possible, the depth of sharpness can be improved, but a small aperture in combination with a very short exposure time requires a high illumination intensity. This is realized with an LED-based illumination system, which is mounted around the collision area. The lighting is operated with 24 V DC from a rechargeable battery, which ensures a constant, flicker-free illumination. This fact is important, as AC-powered illuminants flicker at twice the AC frequency. This can lead to time-dependent brightness differences in the images depending on the recording and AC frequency, which makes later analysis more difficult. A black fabric background surrounds the entire viewing area of the cameras, reducing unwanted stray light and providing a strong contrast to the bright particles used in this investigation. Fig. 3 shows a sequence of raw images of a wet collision from the view of both cameras as an example. Additional example sequences can be found in the appendix. Depending on the speed of the particles, the movement of the particles is captured in around 60 to 150 images per camera, with approximately half of the images being recorded before the collision and half after the collision.

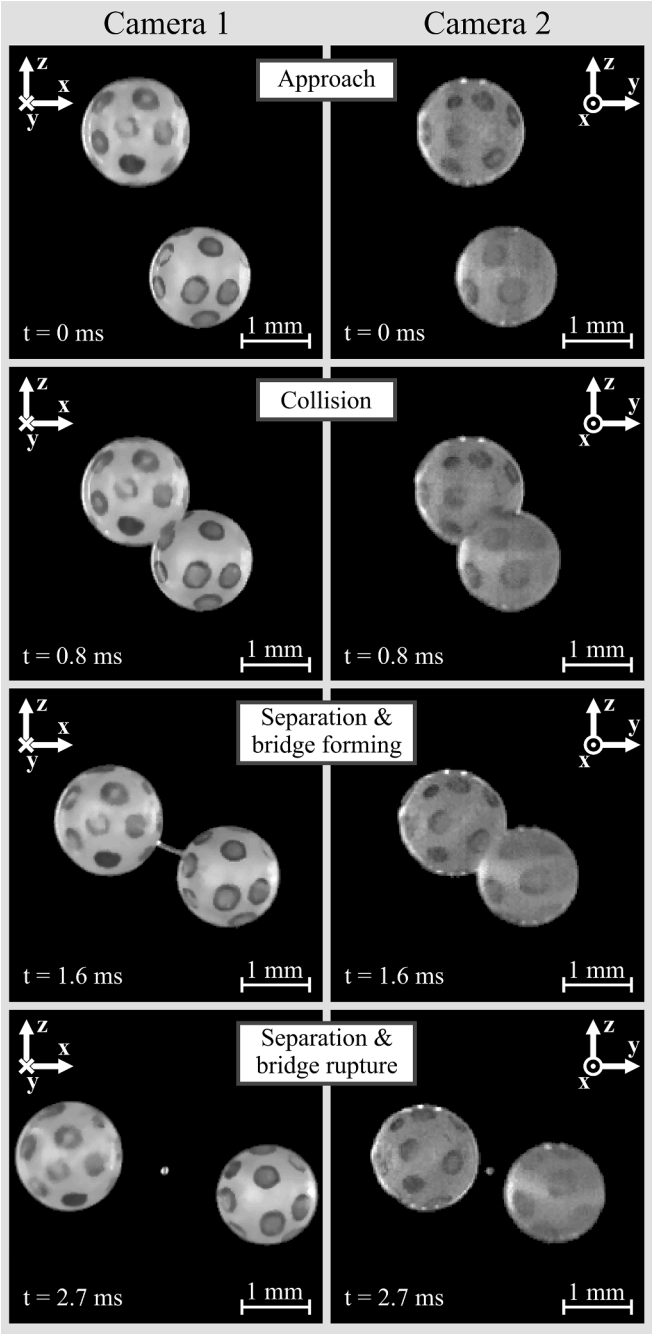

Fig. 3. Free, wet collision of two spherical ZrO_2 particles with a diameter of 1.5 mm out of the perspective of two perpendicular highspeed cameras. The upper particle is wetted with a silicone oil with a dynamic viscosity of 18.9 mPa•s at 25 °C. The lower particle is dry.

The entire setup, except for the two cameras, is shielded from the environment by an enclosure, which can be opened via a sliding door. The enclosure consists of aluminum profile frames with anti-reflective glass between them. This prevents reflections in the images and at the same time protects the collision unit from negative environmental influences such as air circulation in the laboratory. Wherever no cameras are placed, two additional layers of material are applied. The first additional layer consists of a reflective metal foil that enables more consistent illumination in the process area. In order to be able to change the viscosity and surface tension of the liquid during wet collisions, the process chamber can be heated. Therefore, the second additional layer consists of polystyrene foam sheets that serve as thermal insulation. The temperature inside the process chamber is monitored by a temperature sensor (OT150-A, Omni Elektronik GmbH, Germany). The opaque additional layers of the enclosure also ensure that no flickering stray light from outside can enter the process room.

In addition to the already mentioned aspects, the enclosure also serves as a reference frame. Since the frame is assembled into a rectangular cuboid by precise connecting angles, the cameras can be aligned with it so that their horizontal angle to each other is 90°. The cameras are positioned by using geared heads on which the cameras are mounted. These allow the cameras to be tilted around all three spatial axes. To perform the vertical adjustment, a plumb bob is placed in the collision zone and the vertical image axis is precisely aligned on the string of the plumb bob. A level is used to orient the cameras parallel to the horizontal plane.

3. Materials

3.1. Solid particles

The spherical particles used are made of yttrium-stabilized zirconium oxide. Precision bearing balls with a nominal diameter of 1.5 mm and 1 mm were used. Details on material properties, particle geometries and tolerances are summarized in Table 1. In the delivery state, the particles have a very low surface roughness with $R_z = 0.198 \pm 0.045$ µm, which leads to light reflections on the particles in the camera images. This in turn leads to detection problems of the particle rotation. By increasing the roughness to $R_z = 1.747 \pm 0.509$ µm, the reflection could be significantly reduced. The surface roughness of the particles was adjusted using a silicon carbide abrasive powder ($d_{50,3} = 5.32$ µm). To adjust the surface roughness of the particles, the silicon carbide abrasive powder was mixed with distilled water to form an abrasive paste. This paste was placed in a mortar together with the particles. The mixture of abrasive paste and particles was worked with a pestle until the entire surface was completely and uniformly roughened. The progress and status of the roughening process was checked every five minutes under an optical microscope. After complete roughening, the particles were cleaned with distilled water and measured with a micrometer screw series 293–821-30 (Mitutoyo, Japan) to determine the final particle size and to ensure that the sphericity of the particles was maintained. Microscope images of the surface before and after surface treatment are shown in Fig. 4. All roughness measurements and microscope images were taken using the VK-X160K 3D laser scanning confocal microscope (Keyence, Japan).

The particles are marked with point-like markers that are used for rotation detection. These markers are applied to the particles manually under an optical microscope. The paint is blue waterproof permanent marker ink diluted with thinner. This allows to create a visible layer of

Table 1
Particle properties according to [78].

Description	Symbol	Value	Unit
Material	–	ZrO_2 (95 %), Y_2O_3 (5 %)	–
Nominal diameter	d	1.5 (I) 1.0 (II)	mm
Maximum deviation from nominal diameter	–	±5.63 (I) ±9.75 (II)	μm
Maximum deviation from spherical shape	–	0.13 (I) 0.25 (II)	μm
Density	ρ_s	6000	kg/m^3
Young's Modulus	E	210	GPa
Hardness	–	89 ± 2	HRa

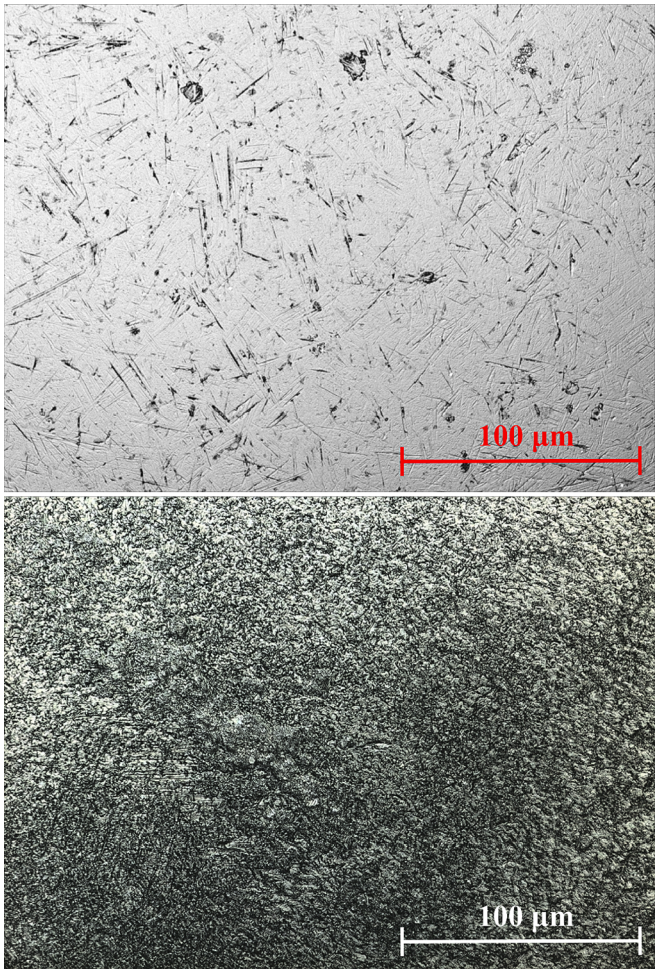

Fig. 4. Laser microscope images of the surface structure of the particles in delivery state (top) and after surface treatment (down).

ink that is at the same time so thin that its influence on roughness structure and sphericity of the particles is minimal, as illustrated in Fig. 5.

3.2. Liquids

The liquid used is silicone oil of various viscosities. The properties of the silicone oils are shown in Table 2. In contrast to water, silicone oil does not evaporate noticeably, which means that a constant quantity of liquid over time can be guaranteed.

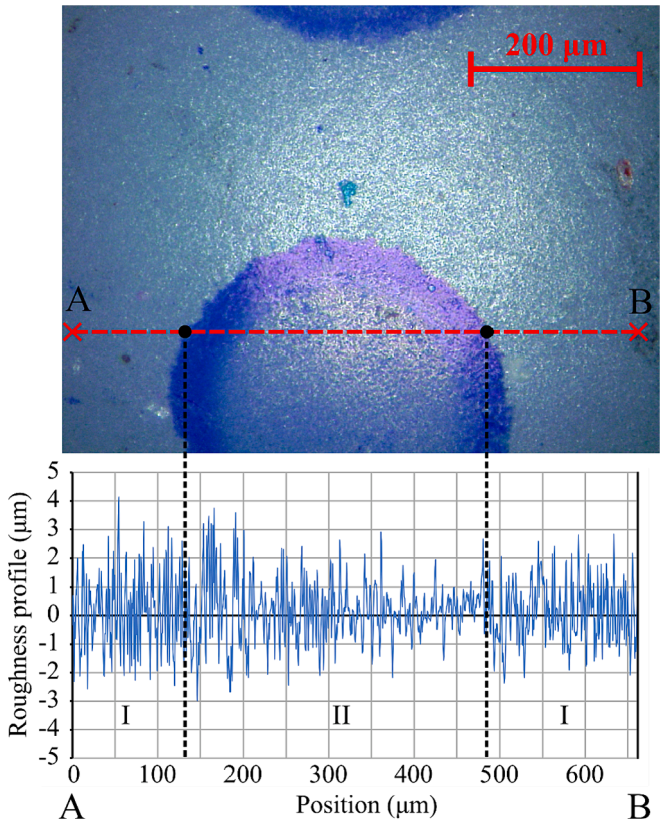

Fig. 5. Influence of the rotation markings on the surface structure. Optical microscope image of a 1.5 mm particle with rotational markings (top). Roughness profile of the section A-B. I: Free particle area. II: Rotation marker. (down).

4. Analytical methods

The camera images need to be analyzed to determine the motion and collision conditions of the particles. This includes the translational motion, the rotation, as well as in case of a wet collision, the liquid layer thickness on the particles. For this purpose, the pixel information of the images is converted into metric measurement data using various methods of digital image analysis with MATLAB® (MathWorks, Inc.). For the evaluation, only images in which both particles are in full view in both cameras are used. The images to be evaluated are digital grayscale images in 8-bit format.

4.1. Translational motion

The translational motion of the particles describes the particles position and their velocity over time. It is determined by locating the centers of mass of the particles in every image of the image sequence of both cameras. The procedure is shown in Fig. 6. In the first step, the image is segmented into the two classes background and foreground object. This is done by binarizing the image using a global threshold. The global threshold is constant for each image recorded from the same camera due to the uniform and temporally constant illumination in the experimental setup. It is set manually. The clear contrast from the background to the particles allows a reliable segmentation. The pixels in the image marked as foreground objects form contiguous clusters that represent the particles or other objects such as liquid droplets or the similar. Since the metric size of the particles as well as the scaling factors of the cameras for converting pixels into metric lengths are known, it is also known in advance how big a particle appears in the image. If a pixel cluster fits into the given size range, it is identified as a particle. This is always the case if the particles in the image are optically separated from

Table 2
Properties of the used silicone oil at 25 °C according to [79].

Description	Symbol	Value	Unit
Dynamic viscosity	η	18.9 (I) 193.2 (II)	$mPa \bullet s$
Density	ρ_f	945 (I) 966 (II)	kg/m^3
Surface tension	γ	20.6 (I) 21.0 (II)	mN/m
Refractive index	n_{liquid}	1.401 (I) 1.403 (II)	–

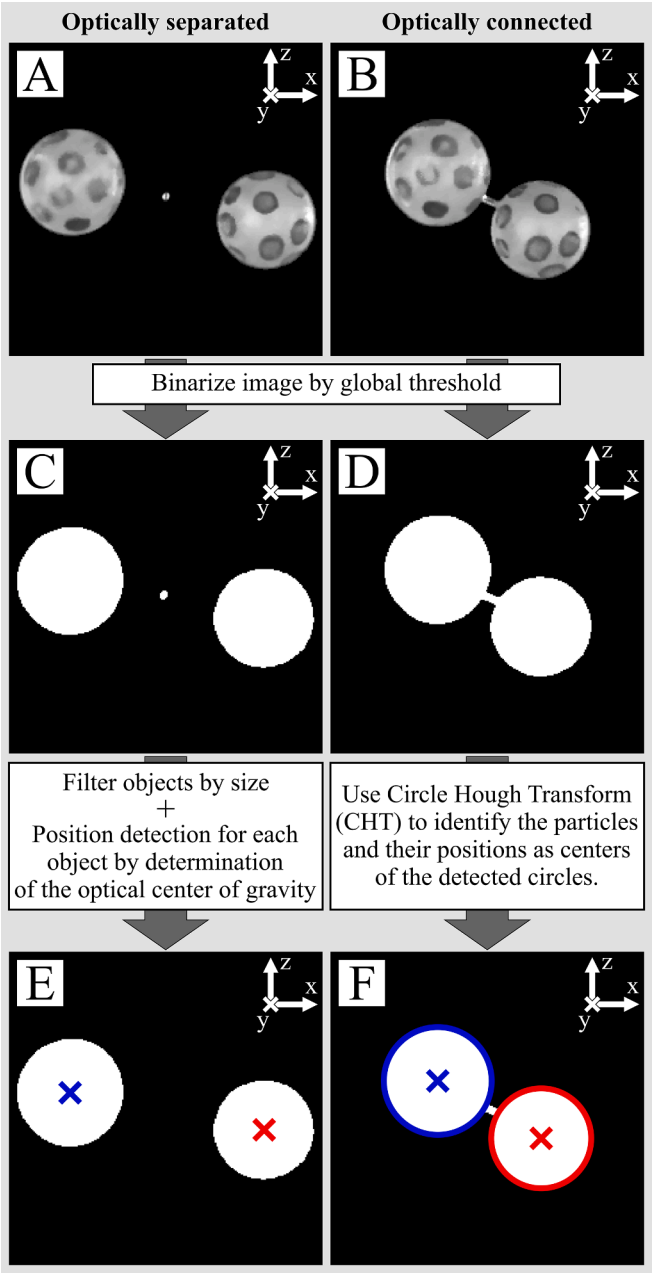

Fig. 6. Procedure of position detection for an optically separated (left) and connected (right) case. A and B: original images. C and D: Binary images. Detected foreground objects are shown in white. E and F: Filtered binary images with detected particle positions.

each other. If the particles are connected with a liquid bridge or if a particle in the image is partially covered by the other particle, there is only one big connected foreground object. These particles cannot be identified directly from the clusters. This is called an optically connected case. The optically connected case and the optically separated case are processed differently, as shown in Fig. 6.

The optically separated case occurs during a collision measurement in the majority of images. Here, two separated particles are detected in the image. Since the particles are dense spheres and if a liquid is involved, a uniform liquid distribution is assumed, the center of mass can be determined from the area centers of the two camera perspectives. The coordinates of the area center correspond to the coordinates of the center of mass. Each pixel i belonging to the particle p corresponds to a square partial area of the entire particle projection area. All partial areas have the same weighting. The first camera $C1$ captures the x-z plane and the second camera $C2$ the y-z plane as shown in Fig. 3. Accordingly, from the first camera, the x-coordinate $s_{x,C1,p}$ and the z-coordinate $s_{z,C1,p}$ of the center of mass of a particle can be calculated from the horizontal $x_{C1,p,i}$ and vertical $z_{C1,p,i}$ pixel coordinates, as well as the total number $N_{C1,p}$ of pixels i associated with the particle p:

$$s_{x,C1,p} = \frac{\sum_i x_{C1,p,i}}{N_{C1,p}}, \tag{1}$$

$$s_{z,C1,p} = \frac{\sum_i z_{C1,p,i}}{N_{C1,p}}. \tag{2}$$

Similarly, from the second camera, the y-coordinate $s_{y,C2,p}$ and the z-coordinate $s_{z,C2,p}$ of the center of mass of a particle are calculated from the horizontal $y_{C2,p,i}$ and vertical $z_{C2,p,i}$ pixel coordinates, as well as the number $N_{C2,p}$ of pixels associated with the particle:

$$s_{y,C2,p} = \frac{\sum_i y_{C2,p,i}}{N_{C2,p}}, \tag{3}$$

$$s_{z,C2,p} = \frac{\sum_i z_{C2,p,i}}{N_{C2,p}}. \tag{4}$$

Due to the camera constellation, the z-coordinate of the particles is determined twice. The camera that is closer to the collision point has a slightly higher resolution of the particles and is therefore more accurate than the camera that is further away. Therefore, the z-coordinate of the first camera is used to determine the coordinates of center of mass $\vec{s}_p$:

$$\vec{s}_p = \left[s_{x,C1,p},\ s_{y,C2,p},\ s_{z,C1,p}\right]. \tag{5}$$

This procedure allows the particle position to be determined with sub-pixel accuracy.

For the optically connected cases, this method is not suitable, since overlapping particles or particles connected with liquid bridges are detected as one large object during segmentation, as can be seen in Fig. 6. With the Circle Hough Transform after Atherton et al. [80] this problem can be solved for a wide range of optical particle overlapping. Circles are detected and their centers are also determined with subpixel accuracy, even if the circles partially overlap. Both methods in combination enable an almost complete detection of the particle positions over the entire recording period, as shown in Fig. 7 for both camera perspectives.

The Circle Hough Transform is carried out using the “imfindcircles” command in MATLAB®. The accuracy, with which the center of the circle is determined with this algorithm, depends primarily on the size of the selected search radius interval. The more precisely the radius of the searched particle can be restricted, the more precisely the center of the circle can be determined. In the case of dry collisions, the radius of the particles is known, which is why the search radius interval can be kept to a minimum. In the case of wetted collisions, a liquid layer with initially unknown thickness is added, so the upper end of the search radius

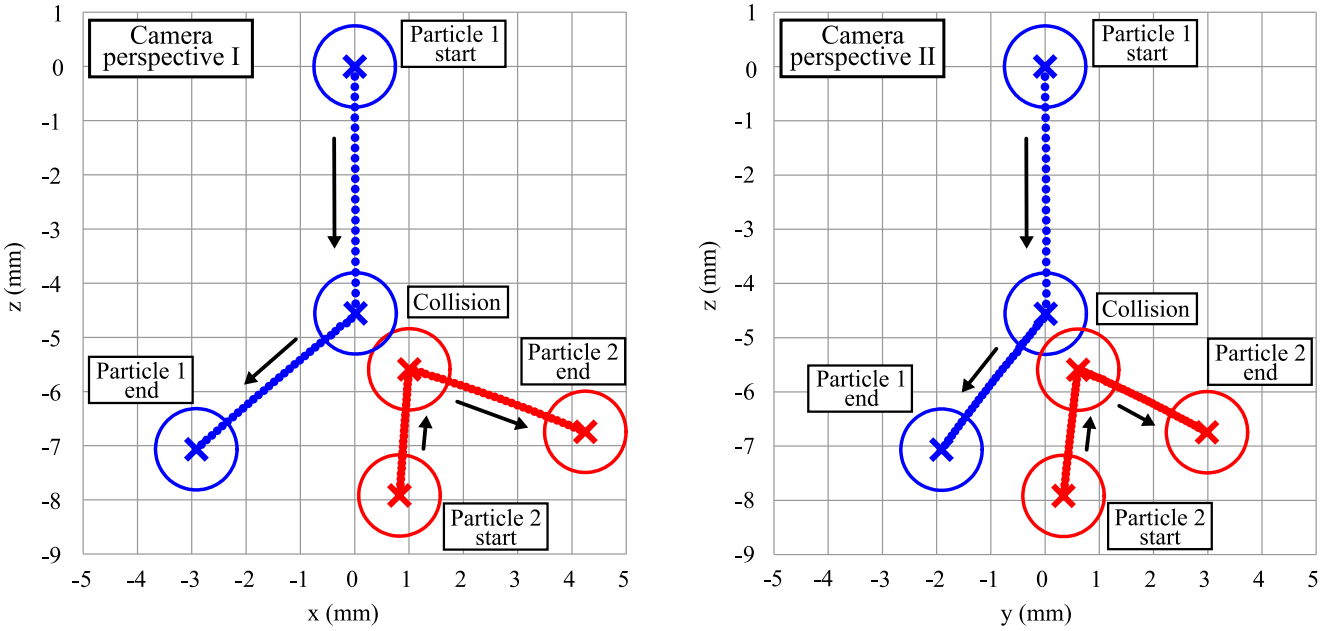

Fig. 7. Detected particle trajectories over the entire acquisition time from both camera perspectives.

interval needs to be extended. A maximum liquid layer thickness of 300 µm is assumed. A significant influence on the detection accuracy could not be determined even with an extended search radius interval.

Contrary to the center of mass method, the circular Hough transformation can be used for the optically separated case as well as for the optically connected case. The reason for the different procedure for the cases is the higher accuracy of the center of mass method. The difference in accuracy is especially significant in the determination of the velocity. From the position at time t and the previous time $t-1$, the velocity $\vec{v}_{p,t}$ of the particle p at time t is calculated with:

$$\vec{v}_{p,t} = \frac{\delta \vec{s}_p}{\delta t} \approx \frac{\vec{s}_{p,t} - \vec{s}_{p,t-1}}{\Delta t}\,, \tag{6}$$

where Δt is the time between two camera images, which can be determined from the frame rate of the recordings f:

$$\Delta t = \frac{1}{f}\,. \tag{7}$$

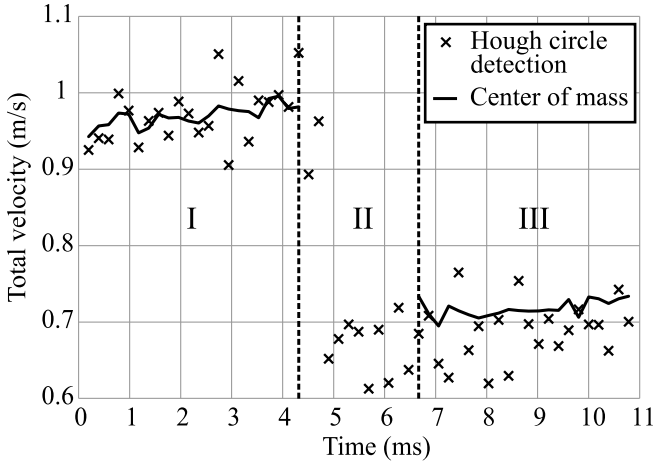

Fig. 8. Comparison of the scatter in the determined velocity over time depending of the position tracking method used. Example of a particle from the wetted collisions from Fig. 3 with three phases: I: Approaching. II: Collision and separation under bridge formation. III:Separation after bridge rupture.

In Fig. 8, the total value of the velocity of particle 1 from Fig. 7 is plotted against time. On the one hand, the position data from the Circular Hough Transform were used, on the other hand, the position data from the center of mass method were used. The significantly higher scatter of the data with the Circular Hough Transform is clearly visible. In addition, the detection gap of the center of mass method becomes clear with optically connected images shortly before and after the collision, while the Circular Hough Transform shows an uninterrupted detection. The results of both algorithms can theoretically be negatively influenced by strong irregularities in the particle profile caused by the liquid layer, e.g. shortly after the liquid bridge ruptures. However, no significant influence could be observed in the measurements carried out here.

Fig. 9 shows the time-resolved positions and velocities of the individual spatial directions for the collision from Fig. 3 for both particles. The velocities in the z-direction show a linear course both in the approach phase and in the separation phase after bridge rupture due to the gravitation acting in the negative z-direction. Due to the short period of time, the influence of gravity is small, but not neglectable. Accordingly, the position curves in the z-direction show a quadratic curve at corresponding sections. The velocities in x- and y-direction show a temporally constant course in the approach phase as well as in the separation phase after bridge rupture. Correspondingly, the position curves in the x- and y-direction show a linear course at corresponding sections. This indicates that before and after the particle interaction, external forces are neglectable except for gravity. Based on an assumed maximum velocity of a particle in the experimental setup of 3 m/s and a maximum rotational velocity of 1500 1/s, this assumption is confirmed by calculated estimation of the possible forces. The drag force on a particle is less than 5 % of the gravitational force, the Magnus effect is less than 10 % of the gravitational force and the buoyancy force is less than 0.01 % of the gravitational force due to the significant density difference between air and solid.

Due to the insufficient recording frequency of the cameras and the inevitable optical overlap of the particles in at least one camera perspective outside of a perfect head-on collision, neither the exact movement of the particles through the liquid layer nor the exact collision time of the particle surfaces can be directly observed. Due to the recognition that only gravity has a significant influence on the particle movement outside the particle collision, it is possible to determine the collision time and the exact collision and rebound velocity with high

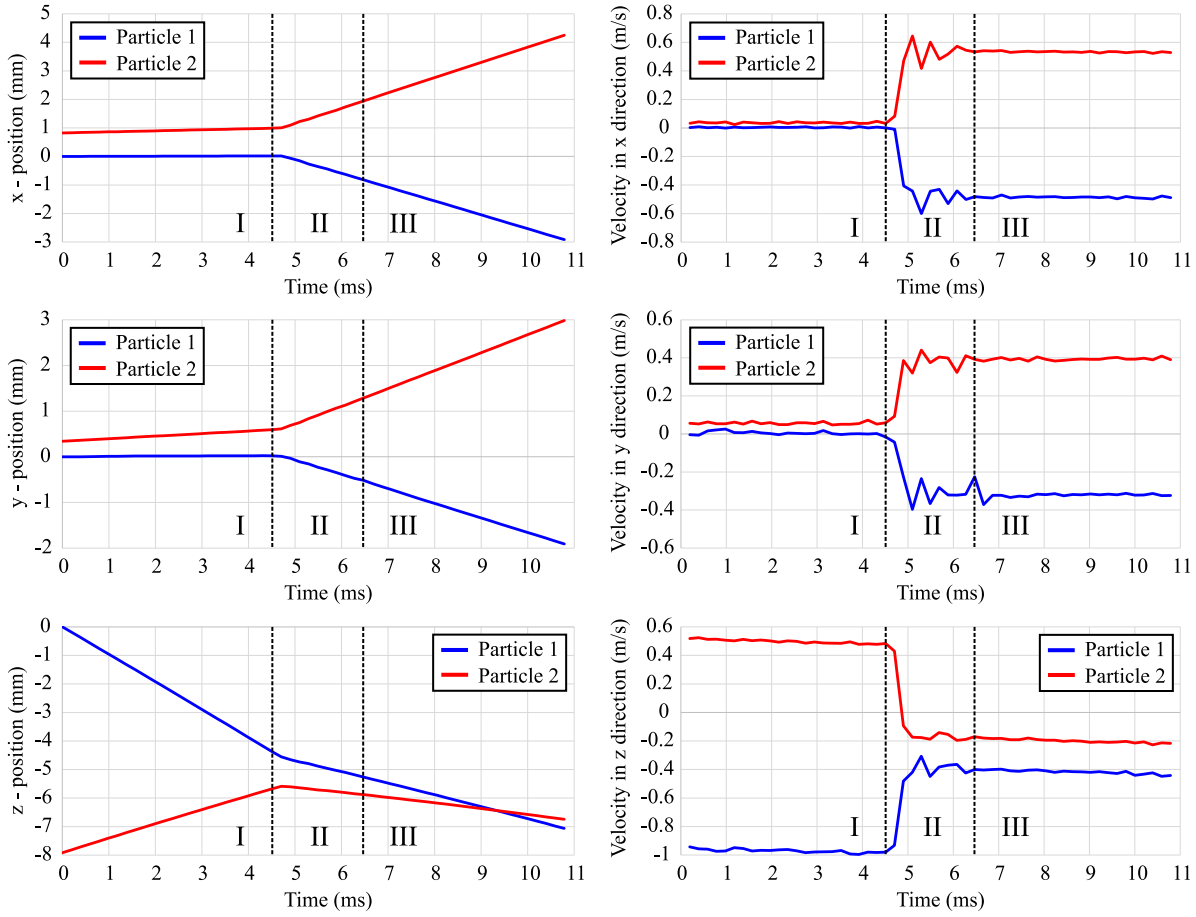

Fig. 9. Measured positions and velocities in all spatial directions over time of the wet collision shown in Fig. 3. I: Approaching. II: Collision and separation under bridge formation. III: Separation after bridge rupture.

precision. For this determination, the measured positions and velocities before and after the collision are used by execution of forward and backward extrapolation. Exclusively the data determined by the center of mass method is used for this purpose due to its high accuracy. The measurement with the center of mass method is possible from the beginning of the recording until shortly before the collision, as well as again after bridge rupture or collision, depending on whether the collision is dry or wetted, until the end of the recording. This ensures a valid database of movement from which extrapolation can be carried out with high accuracy. In addition, the time span to be overcome by extrapolation before the collision is extremely short, which further increases the accuracy. Due to the insufficient accuracy, the position data from the Circle Hough Transform is used solely to assign the position data before and after the collision to the correct particle, i.e. to enable continuous detection without losing the particle tracking.

4.2. *Particle size and liquid layer thickness*

The wetting method used in the experimental setup creates a layer of liquid around the particle. The thickness of the liquid layer around a particle influences the additional liquid induced energy loss in a wetted collision due to viscous and capillary forces [55]. This makes the determination of the liquid layer thickness a critical factor for a reliable collision investigation under wetted conditions.

In the following, a homogeneous liquid layer thickness is assumed because, as already mentioned in chapter 2, it is not possible to prove or negate this assumption. The reason for this is the optical distortion effect induced by the liquid. Due to the curved surface of the particles in relation to the orthographic view of the cameras in combination with the strongly different refractive index of the liquid to the surrounding air, significant refraction effects occur. This leads to a distorted view of the camera through the liquid layer onto the particle surface. Fig. 10 shows

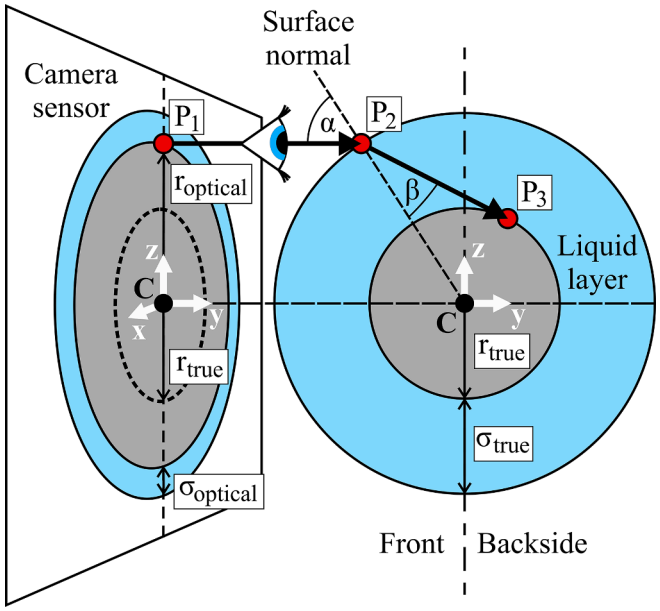

Fig. 10. Particle contour distortion in the image due to the liquid layer.

this effect. The point P_1 marks the spot in the image on the camera sensor where the particle and the liquid layer separate from each other. Thus, the distance of this point to the particle center C defines the optically detected particle radius $r_{optical}$. Starting from the point P_1, the path of the light is traced in the form of a visual line. The visual line runs orthogonally away from the sensor, towards the moistened particle, until it hits the liquid layer at point P_2 at an angle α to the surface normal. Due to the higher optical density of the liquid relative to the surrounding air, the visual line is refracted at a lower angle β to the surface normal according to Snells' law of refraction [81]. Continuing through the liquid layer, the visual line then hits the particle at point P_3, on the averted side of the camera, tangential to the particle's surface. The point P_1 in the image corresponds to the point P_3 on the particle surface. It is shown that the optically measured particle radius $r_{optical}$ does not correspond to the actual particle radius r_{true}. The particle appears significantly larger in the image than it actually is. This also means that up to a certain layer thickness, the liquid layer does not stand out optically from the particle and is therefore not directly visible.

However, the outer contour of the system consisting of particle and liquid layer is not significantly negatively influenced by refraction. The total radius, consisting of the sum of particle radius and liquid layer thickness, is displayed correctly in the image. The outer contour can thus be used to determine the particle size with or without a liquid layer. For subpixel-accurate contour detection, the edge detection algorithm according to Trujillo-Pino et al. [82] was used. In this way, as shown in Fig. 11, the outer contour is obtained in the form of points along which numerical integration is carried out in order to determine the projected area A of the particle. Ideally spherical particles and, in the case of a moistened particle, a uniform distribution of the liquid over the surface are assumed. So, the projection surface can also be assumed to be a circle, which allows the diameter d of the object to be calculated:

$$d = 2 \bullet \sqrt{\frac{A}{\pi}}. \tag{8}$$

The properties of the dry particles are used to calibrate the measurement. Measurements with wetted particles are performed with the calibrated particles. Thus, the diameter of the wetted particles d_{wet}, in combination with the known dry diameter of the particles d_{dry}, allows conclusions to be drawn about the liquid layer thickness σ:

$$\sigma = \frac{d_{wet} - d_{dry}}{2}. \tag{9}$$

The use of the presented method is based on certain further conditions. The system of particles and liquid must be clearly distinguishable from the background. The transparency of the liquid is not relevant. The measurement must take place in a calibrated focus plane of the camera, where the object edges are sharply imaged for edge detection and where the scaling factor from pixel to metric length is known. These conditions are very well satisfied during the approximation of the particles, allowing the liquid layer to be determined very reliably before the collision. After the collision, the particles may leave the narrow plane of focus quickly as in the case shown in Fig. 11. When leaving the focal plane, the particle becomes blurred and the particle grows optically. This leads to a fictitious increase in the thickness of the liquid layer in the measurement, which does not correspond to reality. This problem can be avoided if the collision plane lies exactly in the projection plane of a camera. Otherwise, a measurement of the film layer thickness after the collision is only possible with compromises in accuracy.

The measurement method is verified by gravimetric control measurements as shown in Fig. 12. For this purpose, a ZrO_2 particle with a diameter of 1.5 mm was attached to a 70 µm thin thread and placed in a precision balance. The balance is a K100 tensiometer (Krüss GmbH, Germany), which has a measuring precision of ± 15 µg. The balance is tared with the dry particle. Subsequently, the particle is moistened evenly with a silicone oil of a dynamic viscosity of 193.2 mPa•s at 25 °C

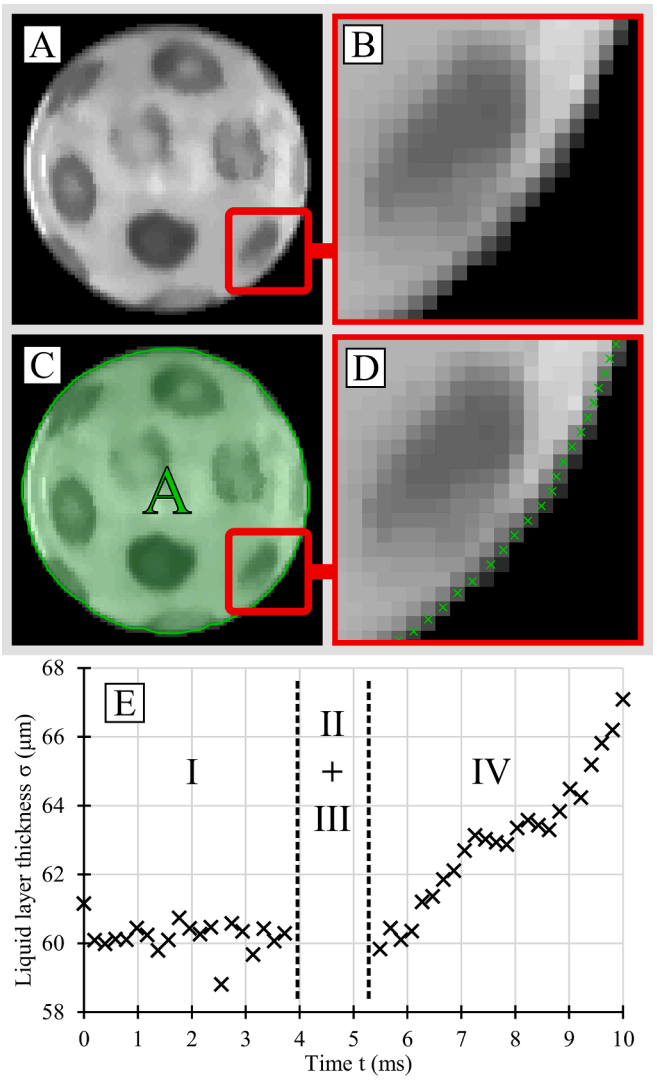

Fig. 11. Liquid layer detection. A: Original image of a particle covered by a 60 µm thick layer of silicone oil. B: Close-up of the edge region of the particle. C: Detected outer contour according to Trujillo Pino et al. [82] and the resulting projection area A of the particle. D: Close-up of the particle edge with detected contour points. E: Measured liquid layer thickness over time. I: Approaching. II: Collision. III: Separation under bridge formation (no measurement possible due to optically overlapping). IV: Separation after bridge rupture (particle is leaving the calibrated focus plane – measurement is less precise).

using the liquid ring method after Buck et al. [52]. The mass difference Δm is measured, which corresponds to the applied liquid mass. In addition to the gravimetric measurement, the particle is recorded by a highspeed camera. This is the same NX-2 series camera from Imaging Solutions GmbH used in the collision setup, with the same Sigma Macro 105 mm F2.8 EX DG OS HSM lens. The image resolution is slightly better with 13.05 µm per pixel due to the different space conditions. The size of the liquid layer is determined from the images using the method just described. The mass of the liquid is calculated via the density of the silicone oil. The comparison of the measured liquid masses of both methods in Fig. 13 shows a very good agreement. The measured liquid masses correspond to liquid layer thicknesses of 35 µm to 222 µm. During the optical measurement, care was taken to ensure that no liquid remained on the thread. In addition, the thread was attached to the back of the particle in order to avoid a distortion of the outer contour. Due to the small amount of adhesive used to attach the thread and the thread itself, the error estimate of smaller than 2 % does not lead to significant changes in the amount of liquid or liquid distribution compared to a

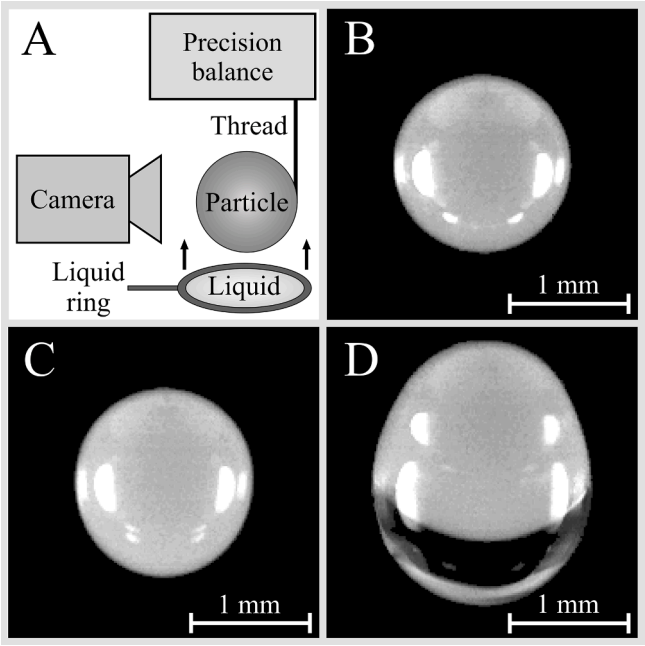

Fig. 12. Control measurement method for liquid layer thickness detection. A: Experimental setup for the control measurements. B: Dry ZrO_2 particle with a diameter of 1.5 mm. C: Wet particle with an average liquid layer thickness of 35 µm. D: Wet particle with an average liquid layer thickness of 222 µm.

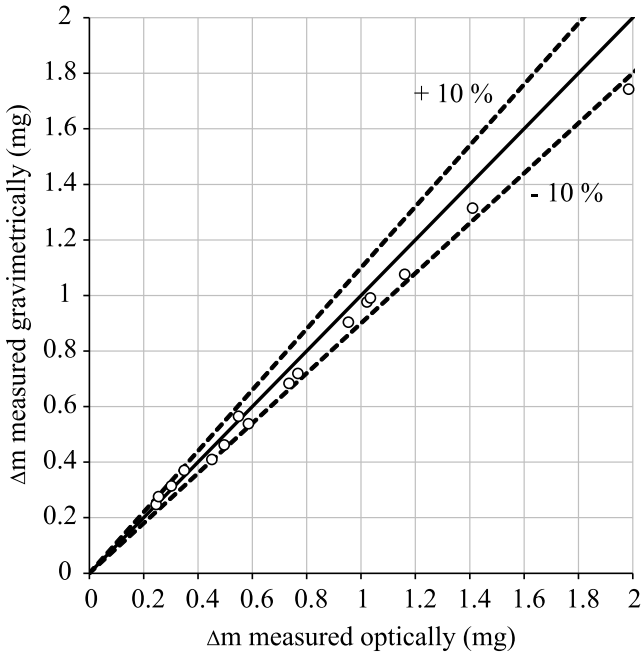

Fig. 13. Parity plot of the gravimetrically measurement of the mass of liquid against the optically measured masses.

clean particle. The larger deviation of the optical measurement compared to the gravimetric measurement at large layer thicknesses results from the increasing uneven distribution of the liquid over the particle. In the case of the particle on the thread in the balance, more liquid collects below the particle as the amount of liquid increases, as shown in Fig. 12. Thus, an increasingly non-spherical structure is formed. Since the measuring method assumes an ideal sphere, this results in increasing measurement errors. This effect, however, does not occur during the collision tests, since the particles are in free fall after wetting. The deviations from the ideal spherical shape that can actually be expected are therefore significantly smaller, and hence also the associated error.

Since the resolution of a particle in the image in this verification experiment is higher than in the actual collision setup, a sensitivity analysis of the measurement was carried out as a function of the particle resolution in the image. For this purpose, artificial images of particles were generated in the BLENDER® (Blender Foundation) animation program. These particles were both dry and provided with homogeneous liquid layers of varying thickness. The rendering was carried out with different resolutions, as shown in Fig. 14. Ten such image sequences were generated with different particles in order to include the influence of the point-shaped rotation markers on the measurements. The optical measurement method was applied to the artificially generated images. Due to the precisely known liquid layer, a direct comparison with the optical measurements was possible. The results in form of the maximum relative errors that occurred over the ten image sequences are shown in Table 3 as a function of the resolution and the liquid layer thickness. For better generalization, the resolution is shown in Fig. 14 and in Table 3 as the dry particle diameter resolution (DPDR). This value indicates how many pixels correspond to the diameter of the dry particle. The layer thickness of the liquid is given as the relative liquid layer thickness σ_R in relation to the dry particle radius. For better comparability with the present study, the corresponding scaling factors and layer thicknesses for a 1.5 mm sphere are also shown in Table 3. A clear trend is observable that the accuracy of the measurement increases with increasing particle resolution. Furthermore, the relative error of the measurement tends to decrease with increasing liquid layer thickness. Table 3 shows some deviations from the trend, which are due to the small sample size of ten sequences. It is therefore random whether, for example, rotational markings lead to small distortions of the detected outer contour of the particles or not. Nevertheless, basic trends and orders of magnitude are well represented. The layer thicknesses were determined both too large and too small, so a systematic error could not be detected. According to Table 3, based on the example particle with a diameter of 1.5 mm and the scaling factors of the highspeed camera recordings in the experimental setup of 20.62 µm per pixel and 27.28 µm per pixel, a very low random error of significantly less than 10 % is to be expected, even for very low layer thicknesses of 30 µm. This confirms the method presented as a highly reliable technique for optically determining the amount of liquid on a spherical particle.

4.3. Rotation

In a collision, the rotation has a significant influence on the movement of the particles after the collision and accordingly cannot be neglected. In contrast to previous studies on the influence of rotation, e. g. Buck et al. [53], the initial rotation, i.e. the axis of rotation and rotational speed of the particles, is not known in advance and thus needs to be measured. The rotation after the collision is subject of investigation and is accordingly also measured. For the detection and measurement of the rotation, rotation markers in the form of dots are applied to the particle. Due to the fact that the particle contour must be completely visible for the liquid layer thickness measurement just discussed, black markers, as in the investigations of Labous et al. [49], are not applicable. In combination with the black background, black markings would appear like holes on the particles and at the contour, so the contour would be strongly distorted. The markings applied here have a gray value between the white particle and the black background. Thus, the contour of the particle is preserved in the images, but makes reliable detection of the markers much more difficult, which will be discussed in detail later.

The measurement of the rotation runs in several steps and is illustrated in Fig. 15. First, a particle is cropped from the whole image to minimize the computational effort. In the second step, the image is segmented to identify the pixels that represent rotation markers. In the

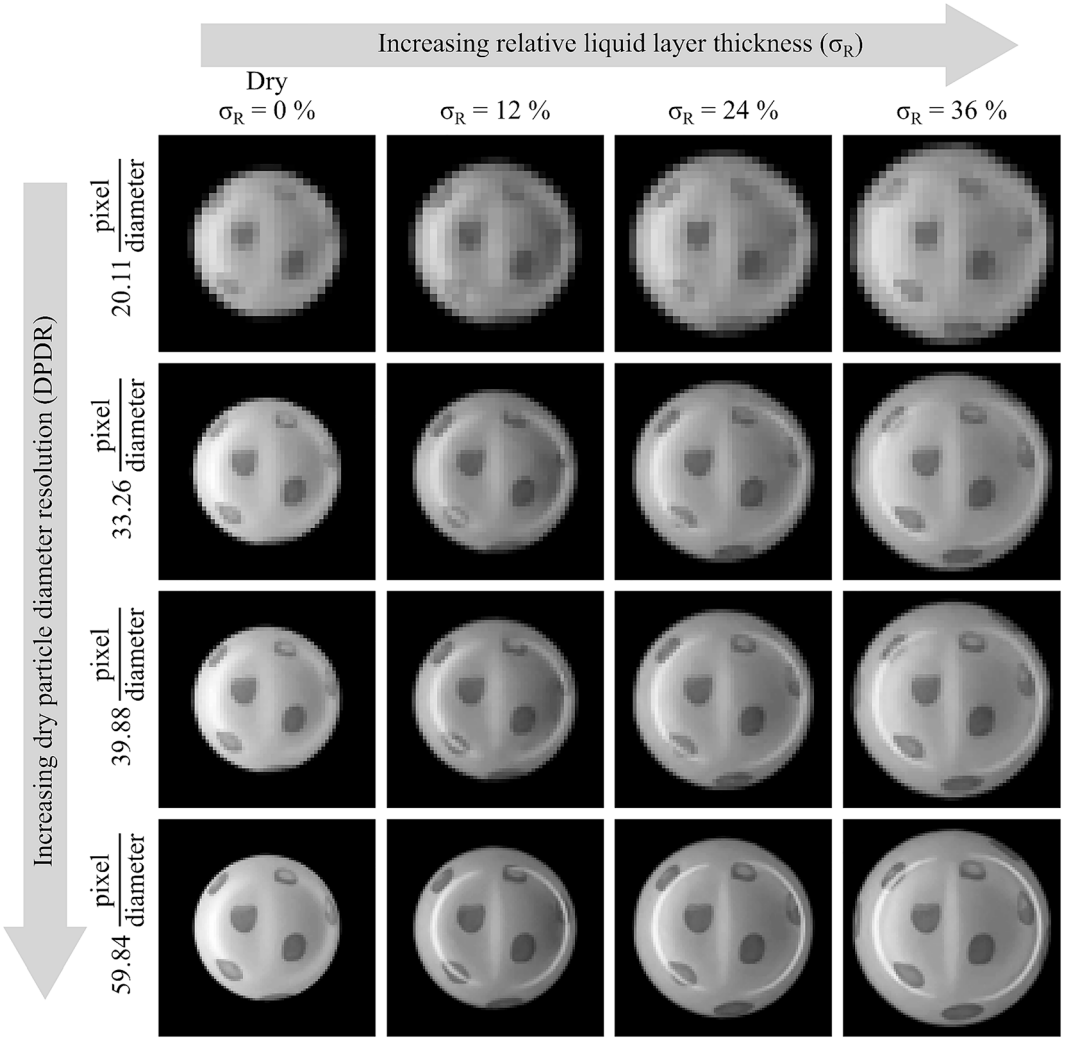

Fig. 14. Image sequence of a particle artificially created with BLENDER® for sensitivity analysis of the optical layer thickness measurement as a function of the image resolution. The particle is recorded at different resolutions in a dry and wet state with defined liquid layer thicknesses.

third step, the optical centers and the size of the pixel clusters representing the rotation markers are determined. These first three steps are performed for each particle and each image of the image series. The fourth step is to assort the detected rotation marker positions over the whole image series into trajectories of the same marker. Such a trajectory characterizes the path of a rotation marker over time. In the fifth step, optical distortions due to perspective and, if present, liquid layer are corrected. In the sixth and final step, the two-dimensional coordinates of the trajectories from both cameras are projected onto a three-dimensional spherical surface and mathematical optimization is used to determine the direction of the rotation axis and the rotation speed. These steps cannot be considered independently, as they influence and depend on each other. For this reason, the individual steps are not described below in chronological order, but in the order required for understanding.

4.3.1. Rotation axis

The following section describes the procedure for identifying the axis of rotation. The starting point for the determination is defined by the detected points of the rotation trajectories. They are projected and normalized onto a three-dimensional unit sphere for easier calculation, whereby the coordinate origin lies in the particle center. The identification of the rotation axis is an optimization problem, which cannot be solved analytically. The optimization condition is shown in Fig. 16 and will be explained in the following.

The measured individual points $\vec{O}_{i,j}$ of a trajectory j are projected perpendicularly onto the assumed axis of rotation $\vec{D}$, which runs through the coordinate origin and has the length of one. These projected points $\vec{P}_{i,j}$ are described according to the vectoral linear equation:

$$\vec{P}_{i,j} = \vec{D} \bullet \lambda_{i,j}, \tag{10}$$

where $\lambda_{i,j}$ is the distance from the coordinate origin along the assumed axis of rotation, which can be determined according to Ericson [83]:

$$\lambda_{i,j} = \frac{\vec{D} \bullet \vec{O}_{i,j}}{\vec{D} \bullet \vec{D}}. \tag{11}$$

The error sum of squares over all $\lambda_{i,j}$ and their mean value $\bar{\lambda}_j$ over all trajectories is minimal with optimally chosen rotation axis. The function to be minimized is thus:

$$minf(\vec{D}) = \sum_{j=1}^{M} \sum_{i=1}^{N_j} \left[\left(\bar{\lambda}_j - \lambda_{i,j} \right)^2 \right]. \tag{12}$$

To minimize the objective function, a particle-swarm algorithm after Kennedy and Eberhart [84] with modifications suggested from Mezura-Montes et al. [85] and Pedersen et al. [86] is used. Here, 100 starting

Table 3
Maximum occurred relative error of the liquid layer thickness measurement in dependence on dry particle diameter resolution and relative liquid layer thickness. Color coding: error < 3 % - dark green; 3 % < error ≤ 5 % - light green; 5 % < error ≤ 10 % - yellow; 10 % < error ≤ 15 % - orange; 15 % < error – red. *) Related to a sphere with a diameter of 1.5 mm.

DPDR	Scaling factor*	Relative liquid layer thickness [%]				
		4	8	12	24	36
$\left[\frac{pixel}{diameter}\right]$	$\left[\frac{\mu m}{pixel}\right]$	Liquid layer thickness* [μm]				
		30	60	90	180	270
20.11	74.58	±26.76 %	±18.90 %	±19.96 %	±14.53 %	±12.13 %
26.64	56.31	±16.78 %	±14.30 %	±10.60 %	±6.58 %	±5.40 %
33.26	45.10	±12.21 %	±12.03 %	±6.40 %	±3.54 %	±2.17 %
39.88	37.62	±12.42 %	±3.96 %	±3.04 %	±2.32 %	±3.04 %
46.52	32.25	±4.60 %	±4.01 %	±3.37 %	±2.20 %	±2.93 %
49.89	30.07	±6.58 %	±3.70 %	±3.16 %	±2.10 %	±2.28 %
53.22	28.19	±5.77 %	±4.23 %	±3.70 %	±2.37 %	±2.86 %
56.53	26.53	±3.82 %	±1.59 %	±2.96 %	±3.92 %	±3.53 %
59.84	25.07	±5.04 %	±5.74 %	±4.48 %	±3.40 %	±3.48 %
63.18	23.74	±5.78 %	±3.17 %	±3.16 %	±2.00 %	±1.97 %
66.49	22.56	±6.22 %	±4.65 %	±2.67 %	±1.79 %	±1.31 %
69.81	21.49	±7.63 %	±3.78 %	±2.85 %	±1.48 %	±0.86 %
73.13	20.51	±3.69 %	±2.09 %	±2.44 %	±1.45 %	±0.70 %
76.49	19.61	±4.21 %	±2.51 %	±2.28 %	±1.42 %	±0.59 %
79.80	18.80	±3.52 %	±2.59 %	±2.32 %	±1.41 %	±0.71 %
99.79	15.03	±1.33 %	±1.27 %	±1.78 %	±1.17 %	±0.53 %
133.09	11.27	±1.85 %	±1.89 %	±1.72 %	±0.85 %	±0.51 %

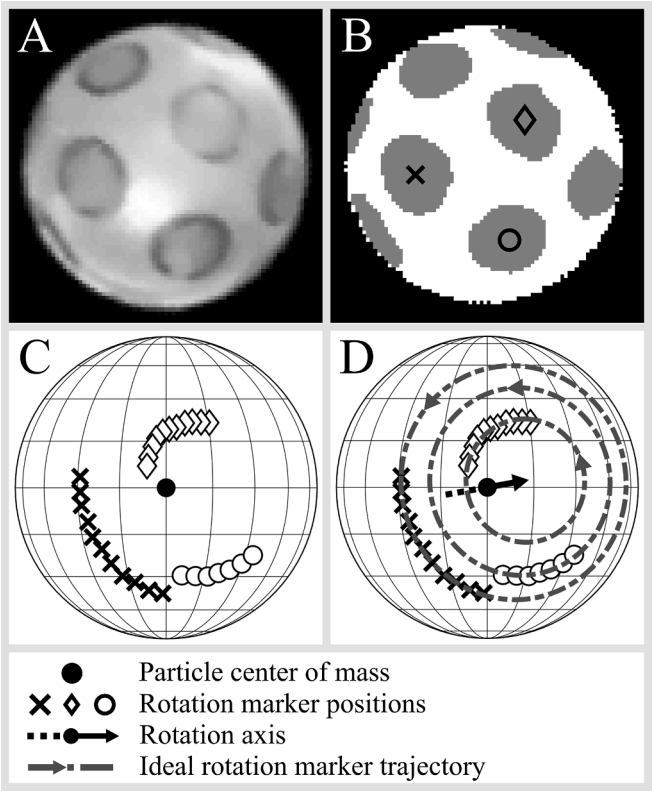

Fig. 15. Rotation measurement procedure. A: Cropped original image. B: Segmented image. The detected rotation markers are shown in gray. The positions of the fully visible markers are detected. C: Rotation marker trajectories – Rotation maker positions on a sphere tracked and assorted over time. D: Rotation axis determined from the measured rotational marker trajectories and the resulting ideal rotational marker trajectories.

points are distributed on only one hemispherical shell, according to the approximate uniform distribution of points on a spherical surface after Kogan [87]. This concentration on one hemisphere reduces the computational effort, because in the first moment it does not matter if the rotation axis shows in positive or negative direction of the final rotation vector.

For a further reduction of the computational effort, the rotation axis is additionally described in spherical coordinates for the optimization. This reduces the optimization variables from three spatial coordinates to two angles. By the reduction on a hemisphere the polar angle is limited to a value range from 0 to π/2, while the azimuth angle remains with a value range from -π to + π.

4.3.2. Angular velocity

After the axis of rotation has been identified, the rotational speed is determined like shown in Fig. 17. For this purpose, the trajectory points, which scatter around the theoretical rotation trajectory due to measurement deviations, are projected onto the theoretical rotation trajectory. The theoretical rotation trajectory of a measured trajectory is formed from the intersection of the shell of the unit sphere with the plane, which is defined in normal form by the support vector $\vec{M}_j = \vec{D} \bullet \bar{\lambda}_j$ and the normal vector $\vec{D}$. The theoretical rotation trajectory describes a circular path in three-dimensional space. According to Vranek et al. [88] all points $\vec{X}_j$ on this circle line can be described with:

$$\vec{X}_j(\omega_j) = \vec{M}_j + \vec{U}_j \bullet \cos(\omega_j) + \vec{V}_j \bullet \sin(\omega_j)\,. \tag{13}$$

Here $\vec{M}_j$ is the center of the circular path, which can be easily determined:

$$\vec{M}_j = \vec{D} \bullet \bar{\lambda}_j\,. \tag{14}$$

$\vec{U}_j$ and $\vec{V}_j$ are two vectors, which are orthogonal to each other and define a right-handed coordinate system together with the rotation axis

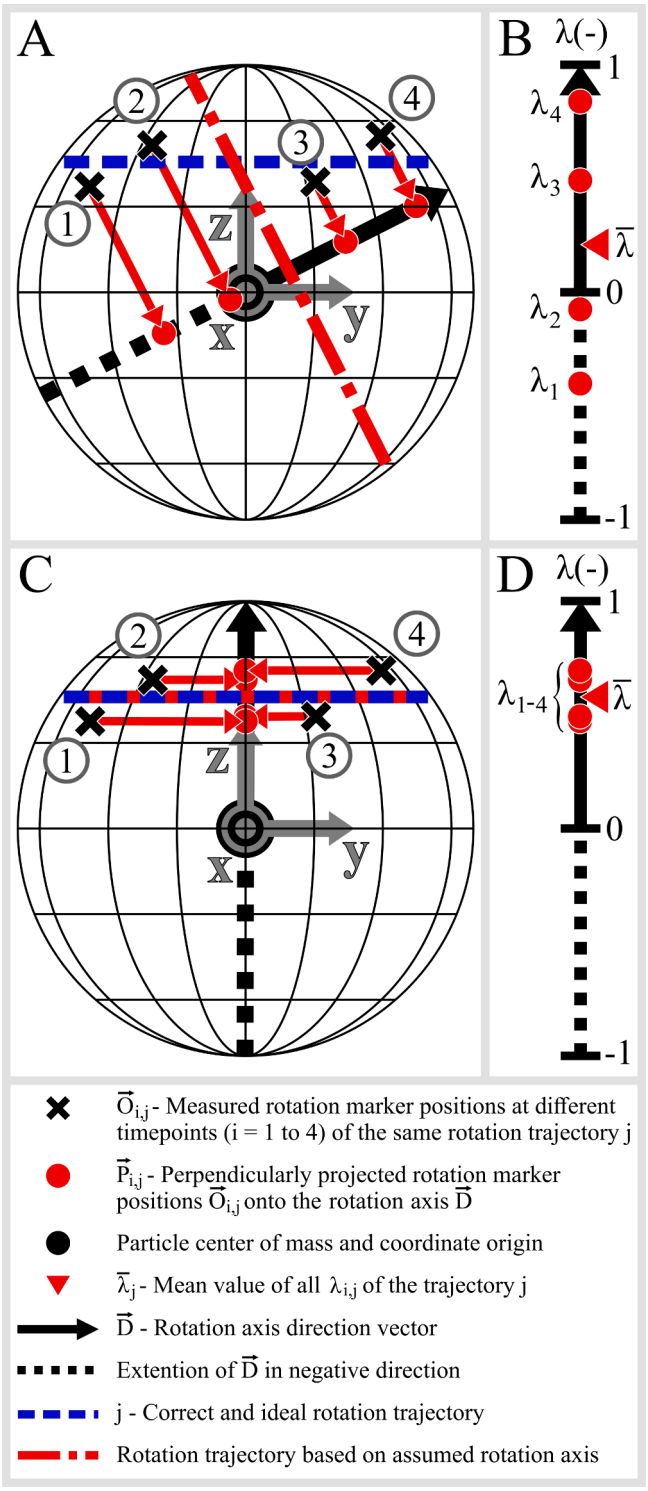

Fig. 16. Rotation axis identification. A: Rotation axis not optimally selected. B: λ coordinates on the rotation axis for a not optimally selected rotation axis – the individual values spread strongly around the mean value. C: Optimal rotation axis. D: λ coordinates on the rotation axis for the optimal rotation axis – the spread of the individual points around their mean value is minimal.

vector $\vec{D}$. The vectors are chosen so that the first measurement point of the trajectory $\vec{X}_{j,1}$ corresponds to an angle $\omega_{j,1}$ of 0°:

$$\vec{U}_j = \vec{X}_{j,1} - \vec{M}_j \,, \tag{15}$$

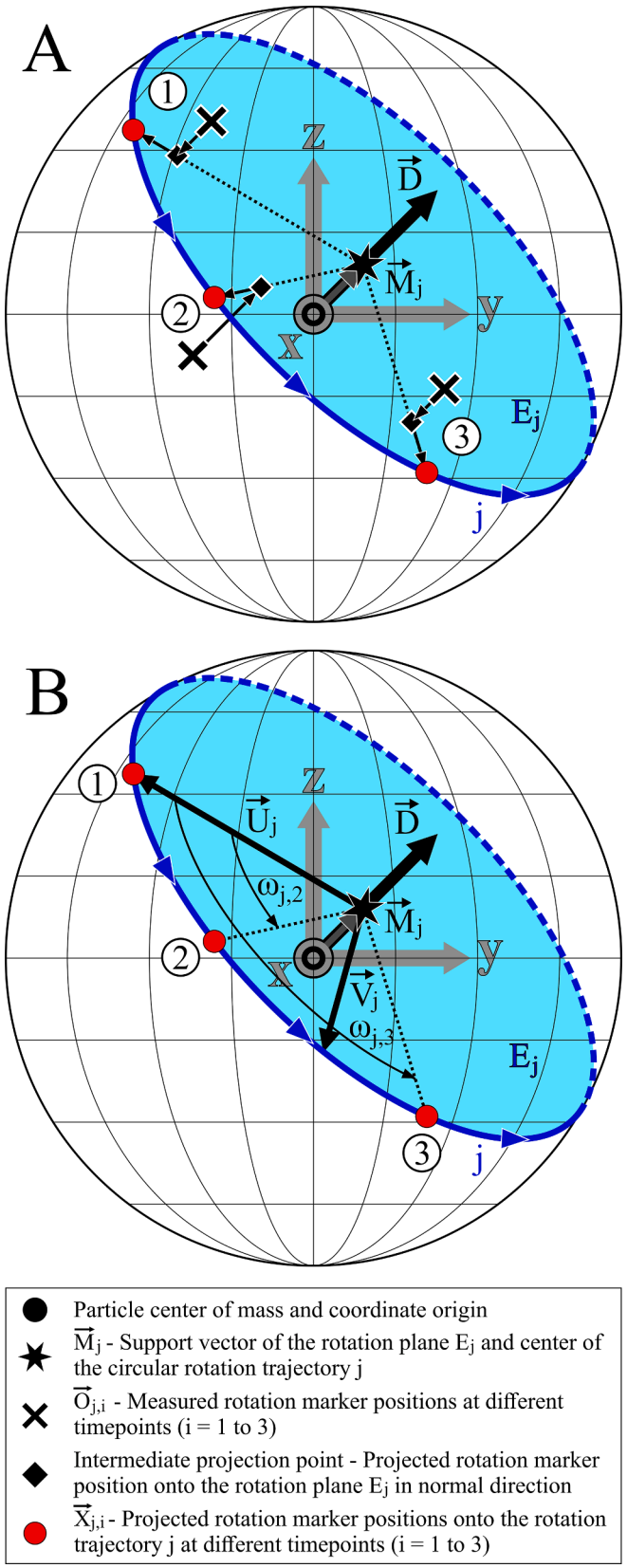

Fig. 17. Determination of the angular velocity. A: Projection of the measuring points onto the ideal rotation trajectory. B: Determination of the angles moved by the individual measuring points over time.

$$\vec{V}_j = \left|\vec{U}_j\right| \bullet \frac{\vec{D} \times \vec{U}_j}{\left|\vec{D} \times \vec{U}_j\right|} . \tag{16}$$

With the help of equation (13) the angle for each measuring point is identified numerically. The starting value for the numerical solution of the angle for the measuring point of the current time step $\omega_{j,t}$ is the angle of the previous measuring point $\omega_{j,t-1}$. This prevents the wrong direction of rotation from being determined for trajectories that cover an entire angular range of more than 180 degrees. The angular velocity $\dot{\omega}_{j,t}$ from one measured trajectory point to the previous one is calculated equivalent to equation (6):

$$\dot{\omega}_{j,t} = \frac{\delta\omega_{j,t}}{\delta t} \approx \frac{\omega_{j,t} - \omega_{j,t-1}}{\Delta t} . \tag{17}$$

The rotational velocity before and after the collision is different. Nevertheless, due to the lack of high, external moments on the particle and due to the short observation period, it is assumed that the rotation speed is constant over time during the approach phase as well as during the separation phase of the two particles. The resulting angular velocity $\dot{\omega}$ is determined from the weighted average of the angular velocities of all trajectories. The number of data points per trajectory serves as weighting. The more data points a trajectory has, the more it is weighted. Only trajectories that have more than a specified number of data points are taken into account. A minimum number of five data points was used. This is the case for the identification of the rotation speed as well as for the rotation axis. These determinations are an iterative process. Trajectories whose rotational speed deviates more than 50 %, but at least 25 1/s from the resulting rotational speed, are declared as false detections. These are ignored for the calculation of both the rotation axis and the rotation speed, so the iteration starts again. The rotation vector $\vec{\omega}$ of the particle results from rotation axis and angular velocity:

$$\vec{\omega} = \dot{\omega} \bullet \vec{D}. \tag{18}$$

The resulting angular velocity $\dot{\omega}$ can be either positive or negative. A negative angular velocity means that the calculated rotation axis is inverted compared to the true rotation axis. To obtain the correct rotation axis and a positive angular velocity, the following steps are carried out finally:

$$\dot{\omega} = \left|\vec{\omega}\right|, \tag{19}$$

$$\vec{D} = \frac{\vec{\omega}}{\left|\vec{\omega}\right|}. \tag{20}$$

4.3.3. Optical distortions

To confirm the algorithms presented for determining the axis of rotation and rotational speed, as well as for identifying interferences on the measurement, ten image sequences of rotating individual particles were created from two camera perspectives offset by 90° using the animation program BLENDER® as shown in Fig. 18. The image sequences correspond to an acquisition frequency of 5100 fps, which is the same as the acquisition frequency of the cameras in the collision test setup. Per sequence, 30 images per camera perspective were acquired. This corresponds to the observed minimum number of images in the experiment before or after the collision. Images are taken of 1.5 mm spherical particles at a resolution of 18.75 µm per pixel. The orientation of the rotation axis in space, as well as the rotation speed are known and thus serve as comparison values for the optical rotation analysis. The orientation of the rotation is selected randomly. The rotation speeds were set to ten fixed values from 25 1/s to 1200 1/s. The main difference between the synthetic images generated here and the real images is that

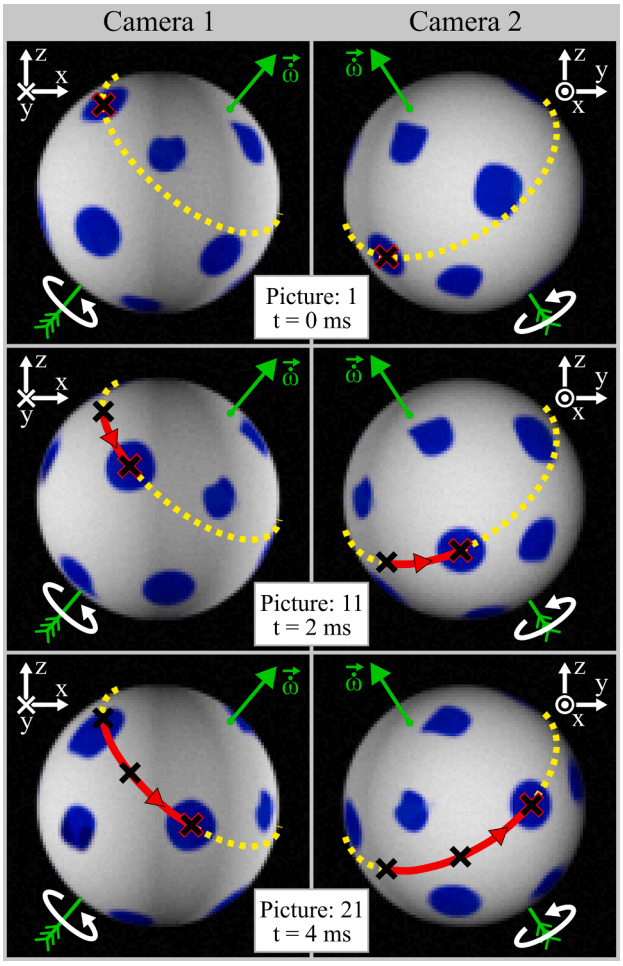

Fig. 18. Artificially generated image sequence of rotating particles with colored rotation markers from two camera perspectives offset by 90°. The rotation axis and speed are known. Rotation speed in the example shown: 400 1/s.

the synthetic images are taken as RGB color images.

While the particles are still white and the background is still black as in the original images, the rotation markers are applied in blue. This has the advantage that the rotation markers in the synthetic images can be segmented easily and reliably via the color information. This is done via the difference between the blue and red color channels of the synthetic RGB images. While this difference is zero for the background and clean particle surface, it is non-zero for the rotation markers. In this way, an exact detection of the rotation markers can be simulated. The shape, size, and spacing of the rotational markers on the synthetic particle surface in BLENDER® varies across sequences via a random algorithm to cover a broad spectrum. This is necessary to cover the irregularities of the rotation markers on the real particles, which are applied manually. The shape of the synthetic rotation markers varies between ideal circular points and random potato-like shapes.

Based on the color rotation markers of the synthetic images, the positions of the rotation markers were detected by segmentation and subsequent optical centroiding as previously described for the particle position detection. Only markers that are fully visible on the particle are used. Markers touching the particle edge are ignored.

4.3.3.1. Perspective distortion. A direct evaluation of the detected rotation trajectories leads to a systematic underestimation of the rotation speed, as shown in Fig. 19. This systematic underestimation of the rotation speed is due to the perspective distortion of the markers by the

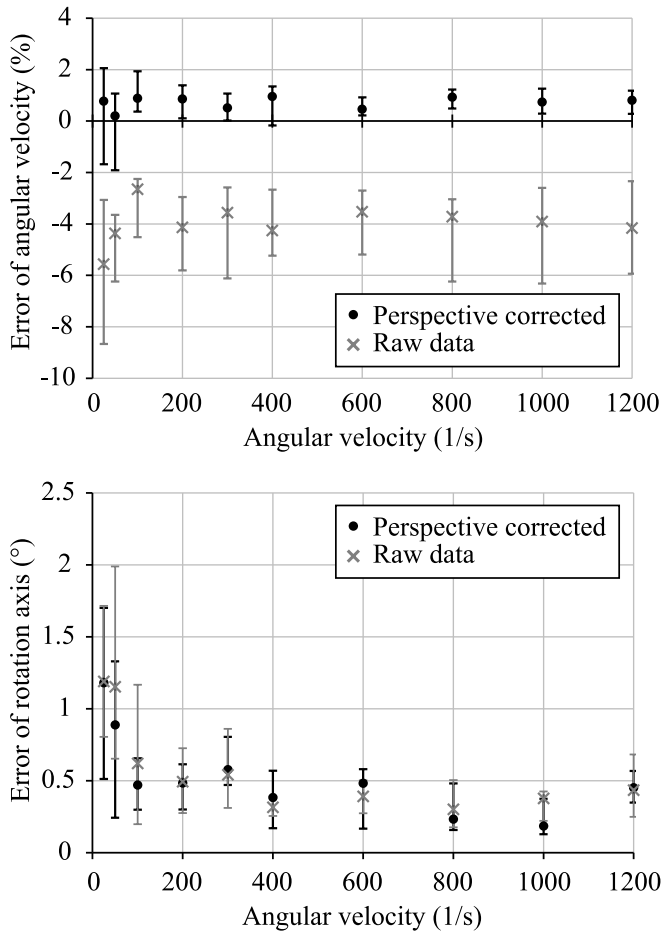

Fig. 19. Influence of the optical distortion on the rotation measurement. The median values are shown, the error bars represent the 25 % and 75 % quantiles.

curved surface of the particles, as illustrated in Fig. 20 for a two-dimensional case. Starting from an orthographic view on the surface of the particle, the optical centers of the rotational markers, shown in red, are detected by averaging. These optical center points are marked as full black dots in Fig. 20 and are located at the radial point $r_{optical}$. The real centers of the markers are marked with a cross and are located at the radial point r_{true}, which is always located further out on the particle in the radial direction than the optically measured center. The effect is stronger the larger the rotation marker is and the further away its center point is from the particle center point. The size effect is illustrated by the rotation markers 1 and 3 in Fig. 20, which have the same distance to the particle center, but marker 3 is larger than marker 1. The error Δr for marker 3 is significantly larger than for marker 1. The effect disappears when the marker becomes infinitely small or the center of the assumed circular marker is on a line with the observation point and the particle center, as in the case of rotation marker 2.

The distortion is corrected for each rotation marker on the particle in the two-dimensional image, as shown in Fig. 21 for a particle section with one rotation marker. Note that the coordinate origin is placed in the particle centroid, and all values are normalized to the particle radius. The optical marker centers detected in the image are shifted outward in the radial direction by the error distance Δr, whereby the correct two-dimensional coordinates of the marker center are achieved:

$$\vec{X}_2 = \vec{X}_1 \bullet \left(1 + \frac{\Delta r}{r_{optical}}\right). \tag{21}$$

In principle, ideal circular rotation markers are assumed. The error distance is a function of the marker size d_{marker} and the distance of the

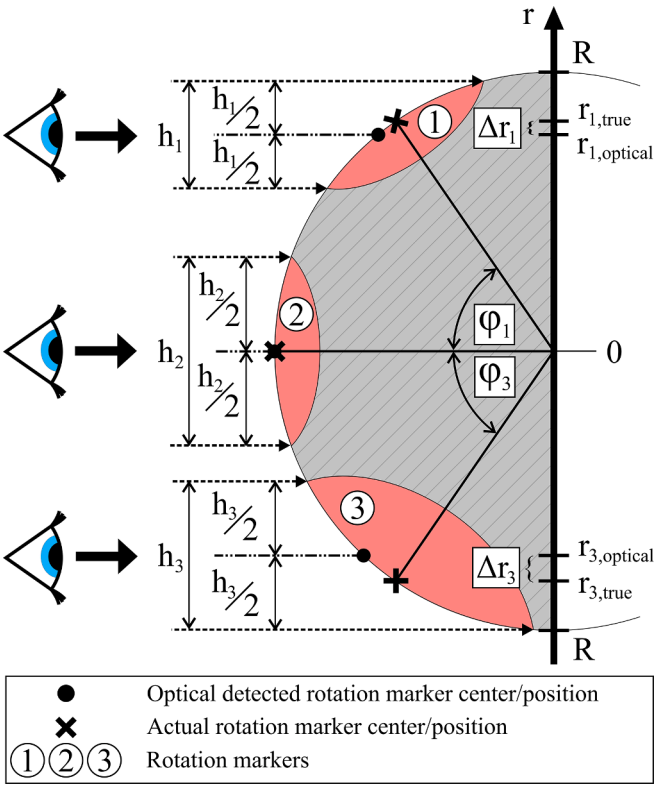

Fig. 20. Distortion of the measured rotation marker positions due to the perspective.

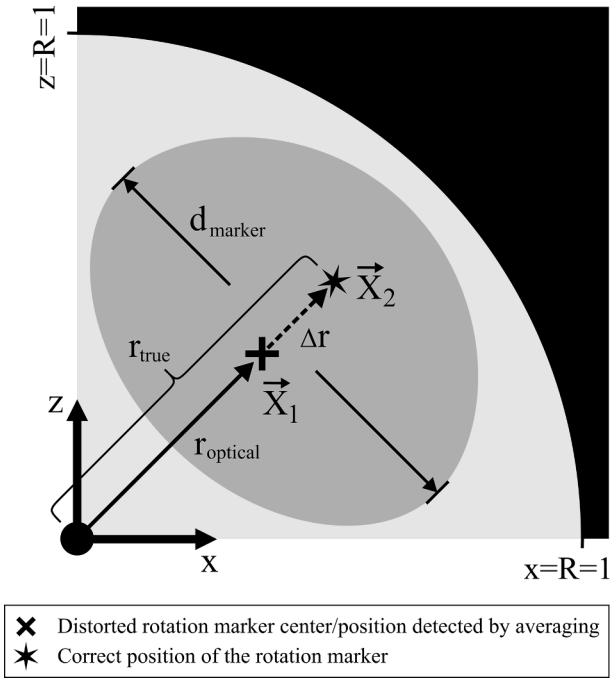

Fig. 21. Correction of the detected rotation marker position to the actual position in an image (not to scale).

optical center of the rotation marker to the particle center $r_{optical}$. From trigonometric considerations based on Fig. 20 results:

$$\Delta r = r_{optical} \bullet \left[\left(\sqrt{1 - \left(\frac{d_{marker}}{2} \right)^2} \right)^{-1} - 1 \right]. \quad (22)$$

By combining equation (21) and (22), a simple expression for the resulting marker position in the image follows:

$$\vec{X}_2 = \vec{X}_1 \bullet \left(\sqrt{1 - \left(\frac{d_{marker}}{2} \right)^2} \right)^{-1}. \quad (23)$$

The size of the rotation markers d_{marker} is determined by their width, perpendicular to the radial direction, since this is not affected by the perspective distortion. If the coordinates of the rotation points are corrected in this way, a significantly improved detection result of the rotation speed is obtained, as shown in Fig. 19. It also shows that the detection of the rotation axis is not significantly affected by this perspective distortion. The perspective correction is applied to all subsequent analyses.

4.3.3.2. Distortion caused by liquid layer. In the case of the presence of a liquid layer, the image of the particle surface is distorted by the refraction of light already discussed for the liquid layer detection. Thus, the rotation markings are also distorted in the image, which accordingly leads to an incorrect measurement. Fig. 22 illustrates this difference in marker detection using a direct comparison of the same particle in the dry and wet state. Computer generated images using BLENDER® were selected to enable the direct comparison. The distortion depends on the thickness of the liquid layer and was set to 400 µm in the example shown for a good visualization of the effect.

Fig. 23 shows the resulting influence of different liquid layer thicknesses related to a 1.5 mm particle on the rotation measurement. To ensure comparability, only a single series of images of a particle was taken here at four different rotation speeds from 100 1/s to 1000 1/s, each with a random rotation axis direction. As a comparative measurement, images were first taken without a liquid layer and then a homogeneous liquid layer of 37.5 µm to 187.5 µm was applied to the same series of images in five steps in order to investigate the influence of the liquid exclusively. The refractive index of the liquid, 1.4, corresponds to that of the liquid used in the collision experiments. Fig. 23 shows that the measurement error of the rotational velocity increases significantly with increasing liquid layer thickness. Thereby, the

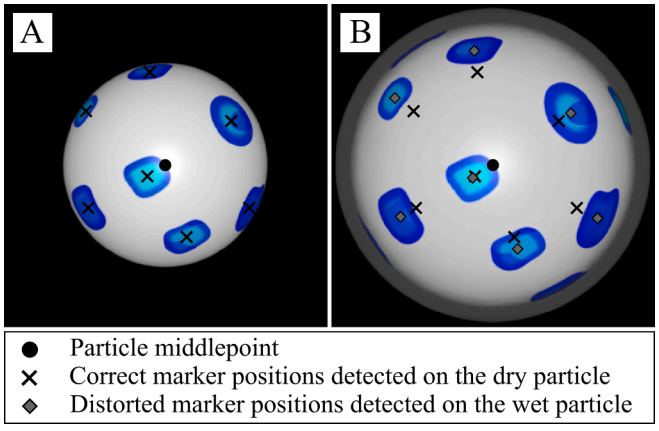

Fig. 22. Influence of the liquid layer on the detection of the rotational marker positions. A: Dry 1.5 mm particle with correct detected marker positions. B: The same particle as in A, wetted with a liquid layer thickness of 400 µm. Wrong detected and actually correct marker positions are shown compared to each other.

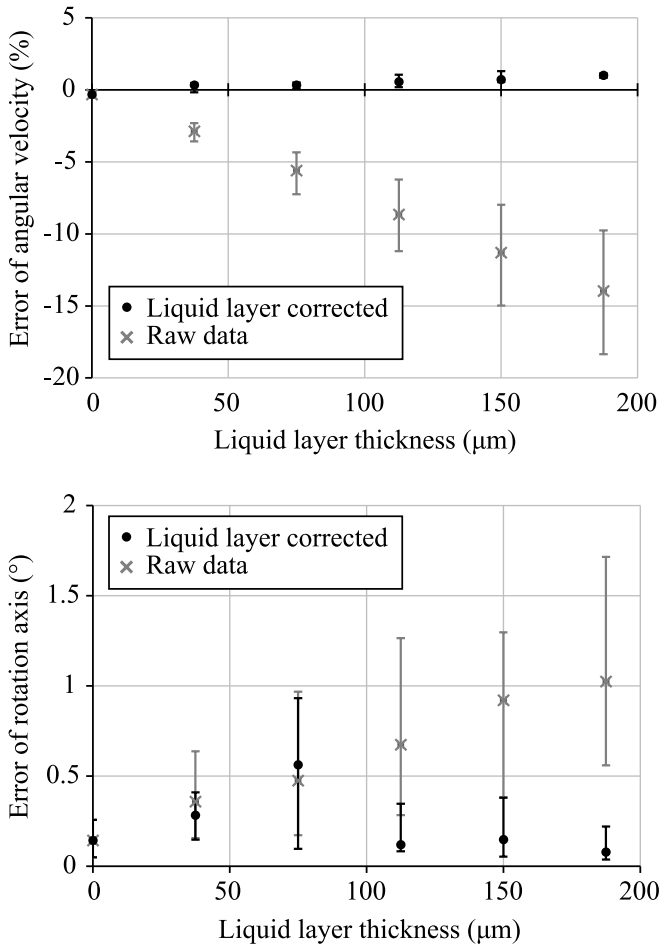

Fig. 23. Influence of liquid layer on rotation detection in dependence of the liquid layer thickness. The median values are shown, the error bars represent the 25 % and 75 % quantiles.

rotation speed is systematically underestimated. The measurement error of the rotation axis also shows a dependence on the liquid layer thickness, but the increase of the error in the range investigated here is still within an acceptable range in contrast to the error of the rotation speed. Nevertheless, the distortion due to the strong influence on the rotation speed cannot be neglected and must be corrected accordingly. Like the perspective distortion, this is a radial effect. This means that each pixel in the image belonging to the distorted particle is shifted in the radial direction, in contrast to the perspective distortion, towards the optical particle center. The procedure for correcting the distortion can be found in the appendix.

Fig. 23 illustrates that after correction, the measurement error for both the rotational speed and the rotational axis decreases to a level comparable to that of the dry particle, independent of the liquid layer thickness. Correction of the liquid film influence is done first, followed by perspective correction to achieve the accuracies shown.

4.3.4. Image segmentation

The presented methods are based on the reliable segmentation of the rotation markers on the particles. This step could be guaranteed in the previous sections by the synthetically generated color images and the thus simple and reliable segmentation of the colored rotation markings in contrast to the grayscale residue of the image. In the grayscale images of the collision experiments, no color is available for segmentation. The segmentation must be able to be performed reliably using gray value differences alone. This is a major challenge, especially for images with inconsistent illumination, which cannot be excluded in the tests carried

out here, most notably in the presence of liquid.

The segmentation of the grayscale images is done by semantic segmentation using a Convolutional neural network (CNN). The network structure used is a U-Net, as proposed by Ronneberger et al. [89], since it has already proven successful in the segmentation of medical grayscale images with significantly more complex patterns [90–99]. The neural network was trained exclusively with synthetic training data created in BLENDER®. This training data was created as a color image of individual particles with blue rotation markers of random size, random distance from each other and varying shape, similar to the creation of the synthetic rotation sequences. In addition, different and always changing illumination scenarios were used. These primary color images were reliably color-based segmented into the three classes of background, free particle area and rotation marker to create the primary label images. In parallel, the primary color images are converted into primary grayscale images to imitate the actual grayscale images from the highspeed cameras. The higher the number of training images and the broader the variation spectrum of the training images, the better the artificial neural network can be trained for general and diverse image situations. For this purpose, the primary grayscale images are changed multiple times by randomly adjusting the brightness, contrast and image sharpness, as well as by random image rotation and image noise. This process is called augmentation. As a result, many training data sets are created from just one primary color image. Each of these adjustments creates a completely new situation for the CNN and thus contributes to the improvement of training for arbitrary situations. All image adjustments that change the position and size of the rotation markers are applied equally to the label image. Finally, both the augmented grayscale images and the label images are cropped to the area of the particle and the image format is adjusted to 64x64 pixels using the nearest-neighbor method [100]. The training data generation process is shown in Fig. 24.

Cropping the image to the particle has a positive effect on the balancing of the classes in the image, since the otherwise strongly represented but contentless background in the image is reduced. Nevertheless, the classes are represented differently in the image. This leads in the training of the CNN to a higher focus on the more represented classes. The class of interest is the rotation marker class, which is usually underrepresented compared to the free particle area. This is balanced by weighting the classes based on their fractions across all training images. Thus, all classes are equally focused in the training process. The reduction of the image size has a positive effect on the training time of the CNN. The disadvantage is the loss of information due to the stretching or compression of the particle in the image to 64x64 pixels. This loss of information and thus also of accuracy of the measurement turns out to be acceptable in the following investigations of the functional efficiency of the semantic segmentation. The functional test is carried out on the one hand by comparison with manually labeled, real images from the collision tests and on the other hand on the basis of synthetic rotation images analogous to the previous sections. The matching with the real collision images is done on the basis of 500 manually segmented single images, comparatively segmented with the help of the CNN, as shown in Fig. 25.

The Accuracy and the Intersection over Union (IoU) [101] serve as comparison values, which are shown separately for each class in Table 4. It can be seen that the rotation marker class of interest has the lowest Accuracy and IoU at 91.485 % and 78.350 %, respectively. Fig. 25 shows an example image whose IoU with 77.892 % is very close to the mean. It is clear that the mismatched pixels of the rotation marker class are mainly in the edge region of the rotation markers and in the edge region of the particles. For the rotation analysis, the correct detection of the optical centers of the fully visible rotation markers is most important. Rotation markers that are too close to the particle edge or even touch it are not considered, which causes possible false detections at the particle edge to become irrelevant. Furthermore, the difference of the detected centers of the rotation markers, shown in Fig. 25 as a cross for the manually segmented images and as a circle for the CNN segmented images, is very small due to the almost uniform distribution of the differently detected rotation marker pixels along the rotation marker edges. The median value of the position differences of the marker centers of all markers detected as fully visible by both the CNN and manually across all images is 0.391 pixels. The 25 % quantile and the 75 % quantile are close to each other at 0.240 pixels and 0.629 pixels,

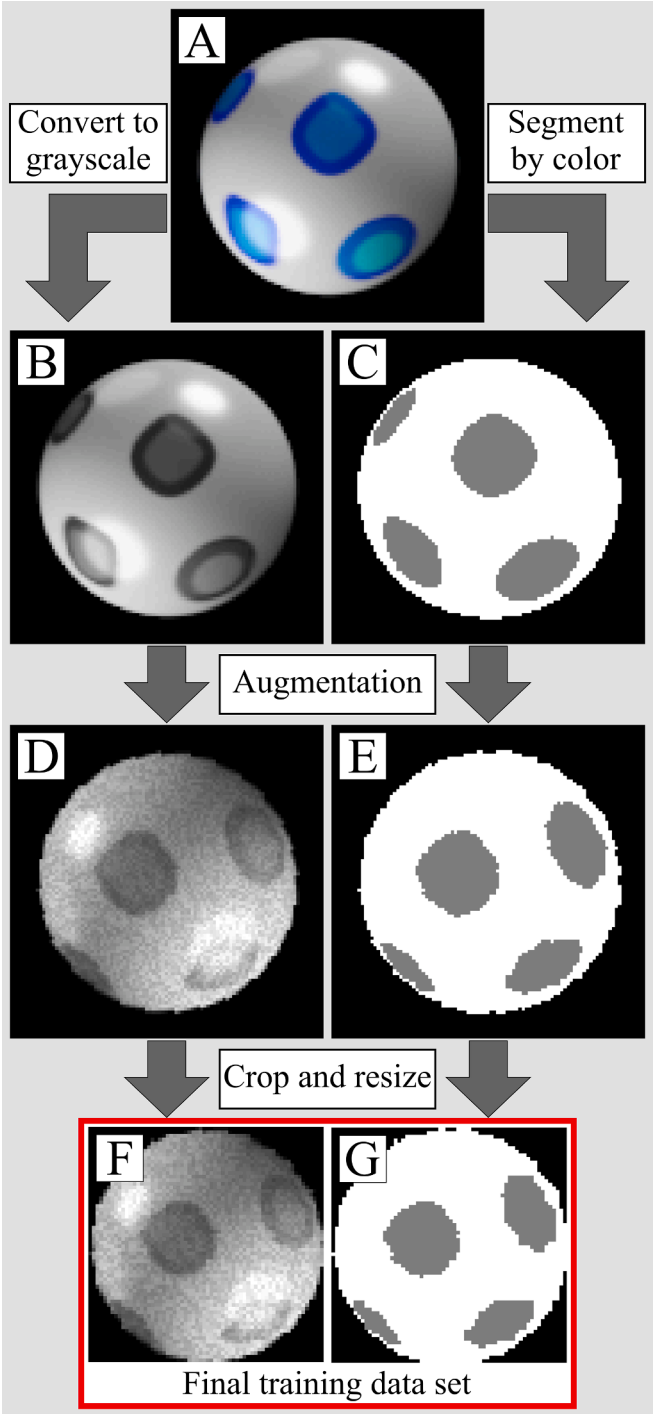

Fig. 24. Creation of synthetic training data for semantic segmentation. A: Original color image created in Blender. B: Primary grayscale image of the original. C: Primary label image: segmented image by color – rotation markers shown in gray. D: Augmented grayscale image. E: Augmented label image. F + G: Final training data set: Grayscale/label image cropped and resized to a resulution of 64x64 pixels.

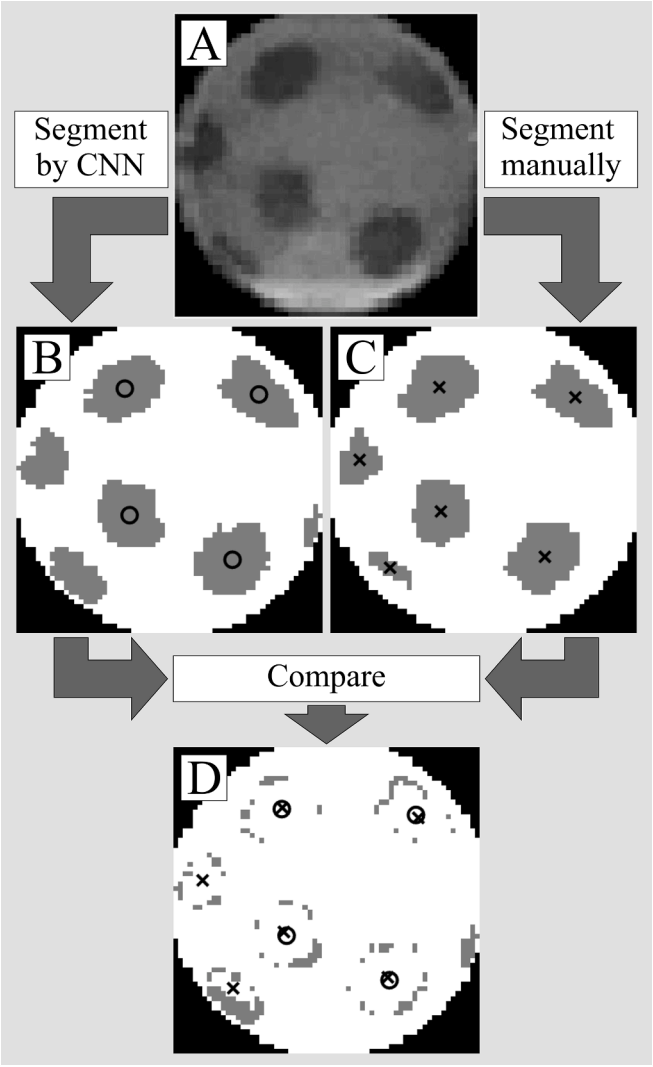

Fig. 25. Comparison of segmentation results of rotation markers of real images from collision experiments between manual segmentation and CNN based segmentation. A: Cropped and resized image to a resolution of 64x64 pixels of a particle from a collision experiment. B: By CNN segmented image. The rotation markers are shown in gray. Positions of the fully visible rotation markers are shown as black circles. C: Manually segmented image. Positions of the fully visible rotation markers are shown as black crosses. D: Comparison image of both segmentation methods. The differently assigned rotation marker pixels are shown in gray.

respectively, confirming a low scatter of the differences. Since the exact boundary between the rotation marker and the free particle surface is often not clearly recognizable and is therefore based on human estimation anyway, even the manually segmented images are not free of errors. As a result, rotation markers can be completely visible in the edge region of the particles according to manual segmentation, but not according to CNN segmentation, or vice versa, as can be seen in Fig. 25 based on the different number of detected, valid center points.

More important than the performance on the single images is the performance of the center point detection over a series of images of a rotating particle. For this purpose, two series of ten different rotating particles, each with colored rotation markers, were created in BLENDER®, with known rotation axis direction and rotation speed. The series is initially segmented based on the color and from this the rotation marker centers and subsequently the rotation is determined. Afterwards, the images of the series are converted into grayscale images, cropped to the particle and resized into the format suitable for the CNN, as already illustrated in Fig. 24. These grayscale images are then segmented by the CNN. Subsequently, the rotation marker centers are determined as well and from this the rotation. The difference in the two series is the illumination of the particles. In the first series, the illumination is kept uniform, there are no strong brightness gradients or reflection spots, which generally simplifies the segmentation of grayscale images. The images of the second series, on the other hand, show non-uniform illumination conditions, which make a usual grayscale image segmentation much more difficult. Example images of both series are shown in Fig. 26.

The results of color-based rotation detection and CNN-based detection are shown for the uniform and non-uniform illumination conditions in Fig. 27. The performance of the CNN-based detection is similar in accuracy and reliability to the color-based detection, both in determining the rotation axis and the rotation speed. Even though the CNN-based detection has a systematically higher error than the color-based method, the error is still within a reasonable range. This applies to both the uniform and non-uniform illumination conditions over the entire velocity range investigated. As with color-based detection, the largest deviations and the largest scattering of deviation for CNN-based detections occur at very low rotational velocities. In particular, under non-uniform illumination conditions, more severe false detections occur sporadically at rotation speeds of 25 1/s. The influence of these low rotation speeds on the collision is very small, which is why these errors are also evaluated as acceptable. Overall, the CNN-based segmentation method is evaluated as very accurate and reliable, both for uniform and non-uniform illumination conditions in grayscale images, whether synthetically created or real images.

5. Model

The measurement data of the particle collisions are compared with the widely used collision model of hard spheres according to Walton [76,77]. It is a simplified model with three model parameters based on the ideas of Maw, Barber and Fawcett [102]. A detailed derivation of the equations is given by Foerster et al. [48]. The main equations of the model are summarized in the following. The aim of the model is to describe the resulting motion quantities after the collision on the basis of the input motion quantities. The resulting quantities after the collision are marked with an apostrophe, input quantities are shown without apostrophes. Indices indicate the reference to particle 1 or 2. Fig. 28 shows a schematic of a collision with the corresponding input quantities used in the model.

The resulting translational velocity $\vec{v}'$ can be determined based on the input velocity $\vec{v}$, the particle mass m and the exchanged momentum $\vec{J}$:

$$\vec{v}_1' = \vec{v}_1 + \frac{\vec{J}}{m_1}, \tag{24}$$

$$\vec{v}_2' = \vec{v}_2 - \frac{\vec{J}}{m_2}. \tag{25}$$

The rotation vector $\vec{\omega}$ can be calculated:

$$\vec{\omega}_1' = \vec{\omega}_1 - \frac{d_1}{2 \bullet I_1}\left(\vec{n} \times \vec{J}\right), \tag{26}$$

$$\vec{\omega}_2' = \vec{\omega}_2 - \frac{d_2}{2 \bullet I_2}\left(\vec{n} \times \vec{J}\right), \tag{27}$$

where d is the diameter and I is the moment of inertia of the particle, which for spherical particles is calculated as:

$$I = \frac{m \bullet d^2}{10}. \tag{28}$$

Table 4
Performance indicators of the CNN compared with 500 manually segmented individual images from collision experiments.

Class	Accuracy (%)	IoU (%)
Background	99.995	99.960
Free particle area	93.493	90.506
Rotation marker	91.485	78.350
Mean	94.991	89.605

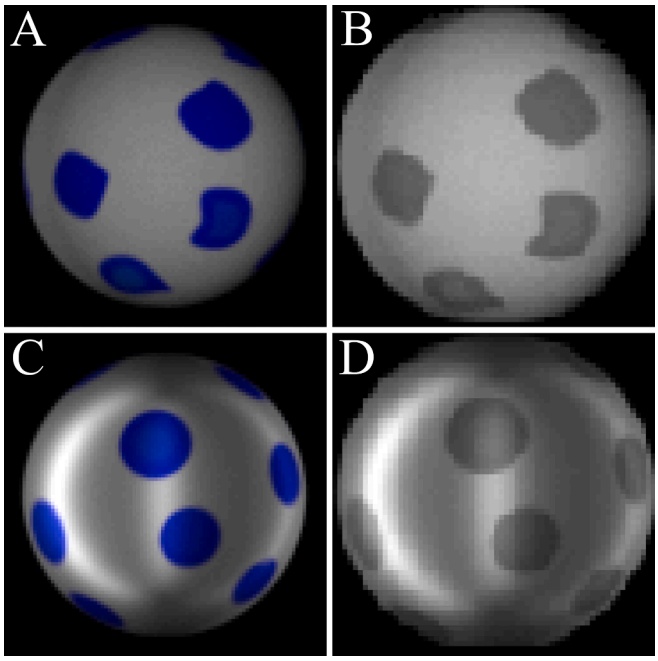

Fig. 26. Examples of synthetically generated test images for the correct function of the CNN. A + B: Uniform illumination conditions. C + D: Non-uniform illumination conditions. Original images (A + C) and corresponding 64x64 pixel grayscale images, which are handed over to the CNN (B + D).

$\vec{n}$ is the normal unit vector pointing from the center of mass of particle 2 to the center of mass of particle 1:

$$\vec{n} = \frac{\vec{s}_1 - \vec{s}_2}{\left|\vec{s}_1 - \vec{s}_2\right|}. \tag{29}$$

For the determination of the exchanged momentum, the slip velocity in the contact point $\vec{q}$ is introduced:

$$\vec{q} = \vec{v}_1 - \vec{v}_2 - \left(\frac{d_1}{2} \bullet \vec{\omega}_1 + \frac{d_2}{2} \bullet \vec{\omega}_2\right) \times \vec{n}. \tag{30}$$

This slip velocity is composed of two velocity components. Firstly, the collision speed in the normal direction $\vec{v}_n$:

$$\vec{v}_n = \vec{n} \bullet (\vec{q} \bullet \vec{n}), \tag{31}$$

and secondly the collision speed in tangential direction $\vec{v}_t$. The tangential direction is defined by the tangential unit vector $\vec{t}$. Both variables can be determined with the help of the following equations:

$$\vec{t} = \frac{\vec{q} - \vec{n} \bullet (\vec{q} \bullet \vec{n})}{|\vec{q} - \vec{n} \bullet (\vec{q} \bullet \vec{n})|} = \frac{\vec{q} - \vec{v}_n}{\left|\vec{q} - \vec{v}_n\right|} = \frac{\vec{v}_t}{\left|\vec{v}_t\right|}. \tag{32}$$

The collision angle γ is defined as the included angle between $\vec{q}$ and $\vec{n}$:

$$\gamma = arccot\left(\frac{\vec{q} \bullet \vec{n}}{|\vec{q} \times \vec{n}|}\right). \tag{33}$$

This angle can vary from 90° to 180°, with 180° corresponding to a head-on collision without relative initial rotation. This angle serves as an indicator of the type of contact, i.e. rolling or sliding. According to the model, if the angle is greater than the critical angle γ_0, the surfaces of the particles adhere to each other and roll off each other, which is referred to as rolling. If the angle is smaller than the critical angle, the particle surfaces slip on each other, which is defined as sliding. The critical angle is determined by:

$$\gamma_0 = arccot\left(-\frac{2}{7} \bullet \frac{(1+\beta_0)}{(1+e) \bullet \mu_0}\right), \tag{34}$$

where e is the coefficient of restitution in the normal direction, β_0 is the maximum coefficient of restitution in the tangential direction, and μ_0 is the maximum coefficient of friction. These three values are the parameters of the model. The exchanged momentum $\vec{J}$ can be calculated with:

$$\vec{J} = -m^* \bullet (1+e) \bullet \vec{n} \bullet (\vec{q} \bullet \vec{n}) + Z \bullet [\vec{q} - \vec{n} \bullet (\vec{q} \bullet \vec{n})], \tag{35}$$

where m^* is the reduced mass:

$$m^* = \left(\frac{1}{m_1} + \frac{1}{m_2}\right)^{-1}, \tag{36}$$

and Z is a coefficient that can be calculated according to the contact type:

$$Z = \begin{cases} -\frac{2}{7} \bullet m^* \bullet (1+\beta_0) & rolling\ \gamma > \gamma_0, \\ \mu_0 \bullet m^* \bullet (1+e) \bullet \frac{\vec{q} \bullet \vec{n}}{|\vec{q} \times \vec{n}|} & sliding\ \gamma \le \gamma_0. \end{cases} \tag{37}$$

Furthermore, Foerster et al. [48] defined two dimensionless metrics Ψ_1 and Ψ_2, which can be plotted against each other for model validation:

$$\Psi_1 = -\frac{\vec{q} \bullet \vec{t}}{\vec{q} \bullet \vec{n}} = \frac{\left|\vec{v}_t\right|}{\left|\vec{v}_n\right|} = |\tan(\gamma)|, \tag{38}$$

$$\Psi_2 = -\frac{\vec{q}' \bullet \vec{t}}{\vec{q} \bullet \vec{n}} = \mathrm{sign}\left(\vec{q}' \bullet \vec{t}\right) \bullet \tan(\gamma') \bullet e. \tag{39}$$

According to the model, Ψ_2 depends on Ψ_1 as follows:

$$\Psi_2 = \begin{cases} -\beta_0 \bullet \Psi_1 & rolling\ \gamma > \gamma_0, \\ \Psi_1 - \frac{7}{2} \bullet (1+e) \bullet \mu_0 & sliding\ \gamma \le \gamma_0. \end{cases} \tag{40}$$

It should be noted that, depending on the contact type, the actual tangential coefficient of restitution β does not necessarily correspond to the model parameter β_0. β is defined as:

$$\vec{n} \times \vec{q}' = -\beta \bullet (\vec{n} \times \vec{q}) \tag{41}$$

which can also be formulated as:

$$\beta = -\frac{\Psi_2}{\Psi_1}. \tag{42}$$

By substituting equations (38) and (40) into equation (42), the dependence of β on the collision angle becomes clear:

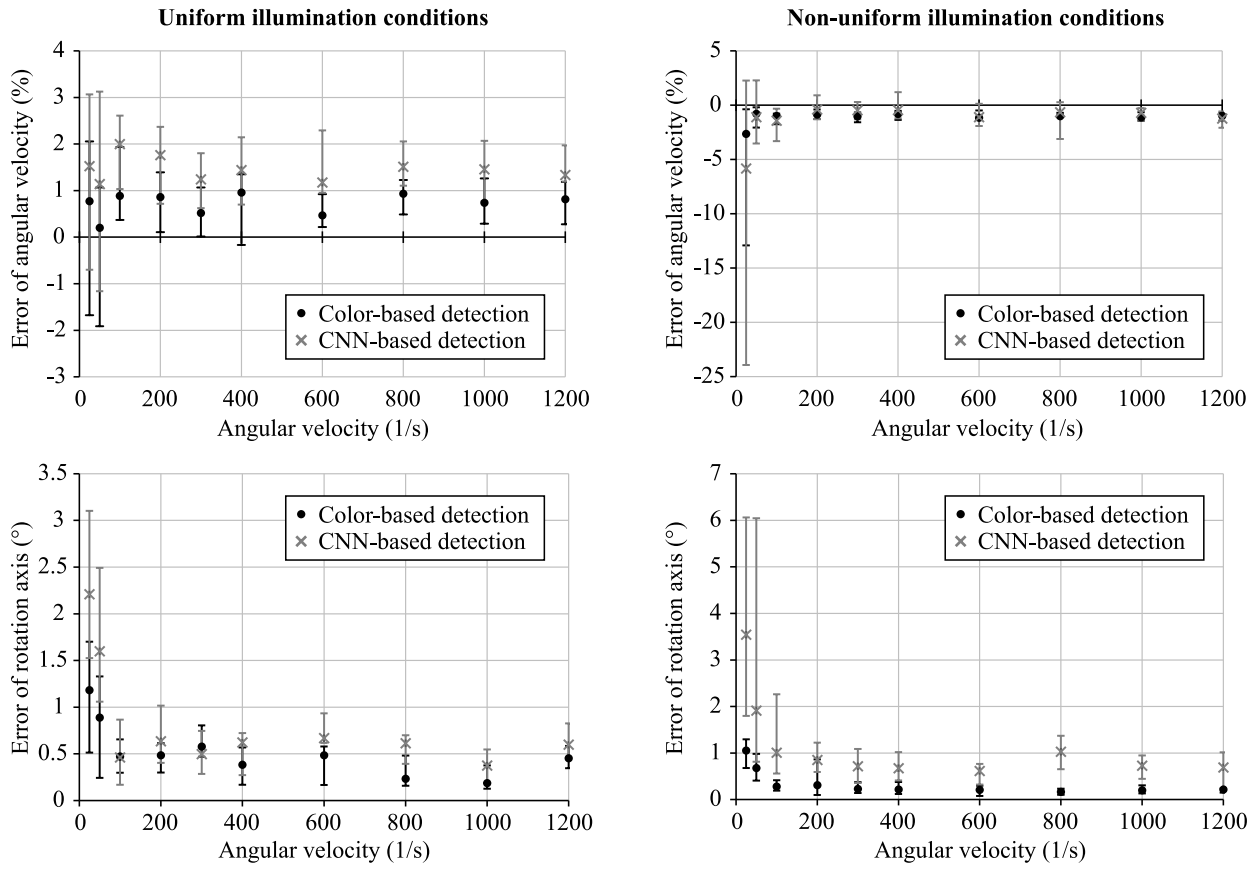

Fig. 27. Function test results of CNN-based rotational marker detection compared with color-based detection using artificially generated test images with uniform and non-uniform illumination conditions. The median values are shown, the error bars represent the 25 % and 75 % quantiles.

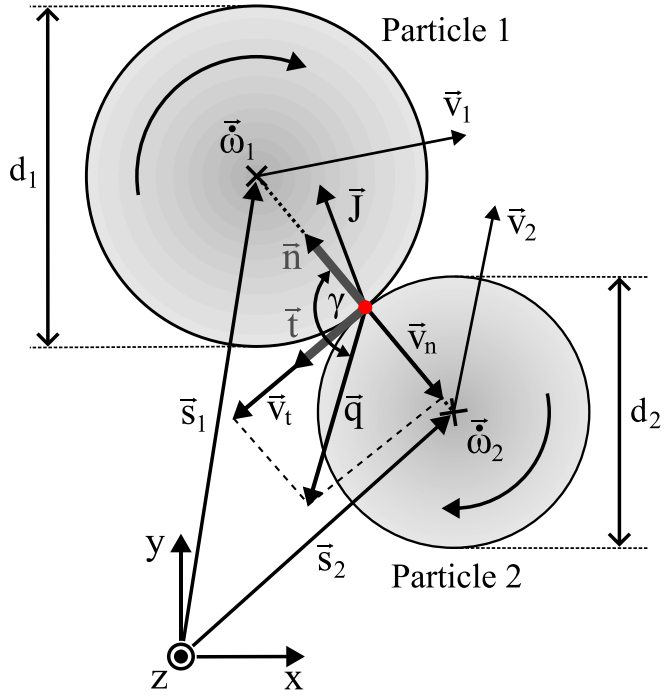

Fig. 28. Typical gemoetry of a binary collision between spheres. The collision plane lies in the x-y plane. The rotation vectors point into the image plane in the negative z-direction. All values are shown before the momentum exchange.

$$\beta = \begin{cases} \beta_0 & \text{rolling } \gamma > \gamma_0, \\ \dfrac{7 \bullet (1+e) \bullet \mu_0}{2 \bullet |tan(\gamma)|} - 1 & \text{sliding } \gamma \le \gamma_0. \end{cases} \tag{43}$$

Similarly, the actual coefficient of friction μ is not constant over the entire collision angle range. It is defined as the ratio of the tangential component of the exchanged momentum to the normal component of the exchanged momentum:

$$\mu = \frac{\left|\vec{n} \times \vec{J}\right|}{\left(\vec{n} \bullet \vec{J}\right)} = \frac{\left|\vec{J}_t\right|}{\left|\vec{J}_n\right|}. \tag{44}$$

According to Luding [103], this results in a theoretical course of μ as a function of the collision angle:

$$\mu = \begin{cases} \mu_0 \bullet \dfrac{tan(\gamma)}{tan(\gamma_0)} & \text{rolling } \gamma > \gamma_0, \\ \mu_0 & \text{sliding } \gamma \le \gamma_0. \end{cases} \tag{45}$$

In contrast, according to the model, the coefficient of restitution in the normal direction e does not depend on the collision conditions and is equal to the model parameter. It is defined as:

$$\vec{n} \bullet \vec{q}' = -e \bullet (\vec{n} \bullet \vec{q}). \tag{46}$$

The total kinetic energy E of the particle system is composed of the kinetic energy of the translational motion and the kinetic energy of the rotation of both particles:

$$E = \frac{m_1}{2} \bullet \left|\vec{v}_1\right|^2 + \frac{m_2}{2} \bullet \left|\vec{v}_2\right|^2 + \frac{I_1}{2} \bullet \left|\vec{\omega}_1\right|^2 + \frac{I_2}{2} \bullet \left|\vec{\omega}_2\right|^2. \quad (47)$$

According to Santos et al. [104], the energy loss $\Delta E = E^{'} - E$ due to the collision can be described as a function of the model parameters, the collision angle, the input velocities and input rotations with:

$$\Delta E = -\frac{m^*}{7} \bullet \left(1-\beta^2\right) \bullet G - \frac{m^*}{2} \bullet \left(1-e^2\right) \bullet \left(\vec{n} \bullet \vec{v}_{12}\right)^2, \quad (48)$$

with:

$$G = \left(\vec{n} \times \vec{v}_{12}\right)^2 + \left(\vec{n} \times \vec{\Omega}_{12}\right)^2 - 2 \bullet \left(\vec{n} \times \vec{v}_{12}\right) \bullet \vec{\Omega}_{12}, \quad (49)$$

$$\vec{v}_{12} = \vec{v}_1 - \vec{v}_2, \quad (50)$$

$$\vec{\Omega}_{12} = \frac{d_1}{2} \bullet \vec{\omega}_1 + \frac{d_2}{2} \bullet \vec{\omega}_2. \quad (51)$$

6. Results and discussion

6.1. Dry collisions

86 equal sized collisions between 1.5 mm particles and 54 unequal sized collisions between 1.5 mm and 1 mm sized particles under dry conditions were evaluated. The equal sized collisions are divided into two series with different collision velocities. The characteristic velocity values of the collisions are displayed in Fig. 29. In each of the three series of dry collision measurements, the slip velocities at the contact point and therefore the total kinetic energy on impact were kept approximately constant. The collision angle was changed, whereby the velocity components in the normal and tangential directions changed. The first series of the equal sized collisions, consisting of 56 individual measurements, was carried out at a low impact energy of 3.59 ± 0.70 μJ and a slip velocity of 1.15 ± 0.12 m/s, which is why it is labeled v↓ in the following figures. The second series of equal sized collisions, consisting of 30 individual measurements, was carried out at a higher impact energy of 10.37 ± 0.24 μJ and slip velocity of 1.88 ± 0.03 m/s, which is why it is labeled v↑ in the following figures. The series of the unequal sized collisions was carried out at a slip velocity of 1.75 ± 0.17 m/s and thus at a similar velocity level of the higher velocity series of measurements of the equal sized collisions. At the same time, the impact energy level of 4.56 ± 0.89 μJ is similar to the low velocity series of the equal sized collisions due to the lower mass of the smaller particle. The smaller mass and moment of inertia of the 1 mm particles leads to a higher scattering of the collision parameters in the unequal sized collisions due to their higher sensitivity to random parameter fluctuations in the experiment. This is also reflected in the initial rotation, which in an ideal case would be zero. While the initial rotation speed for the 1.5 mm particles is only 32.84 ± 40.94 1/s on average, the average value for the 1 mm particles is around twice as high at 67.32 ± 47.55 1/s. The collision conditions and resulting model parameters are summarized in

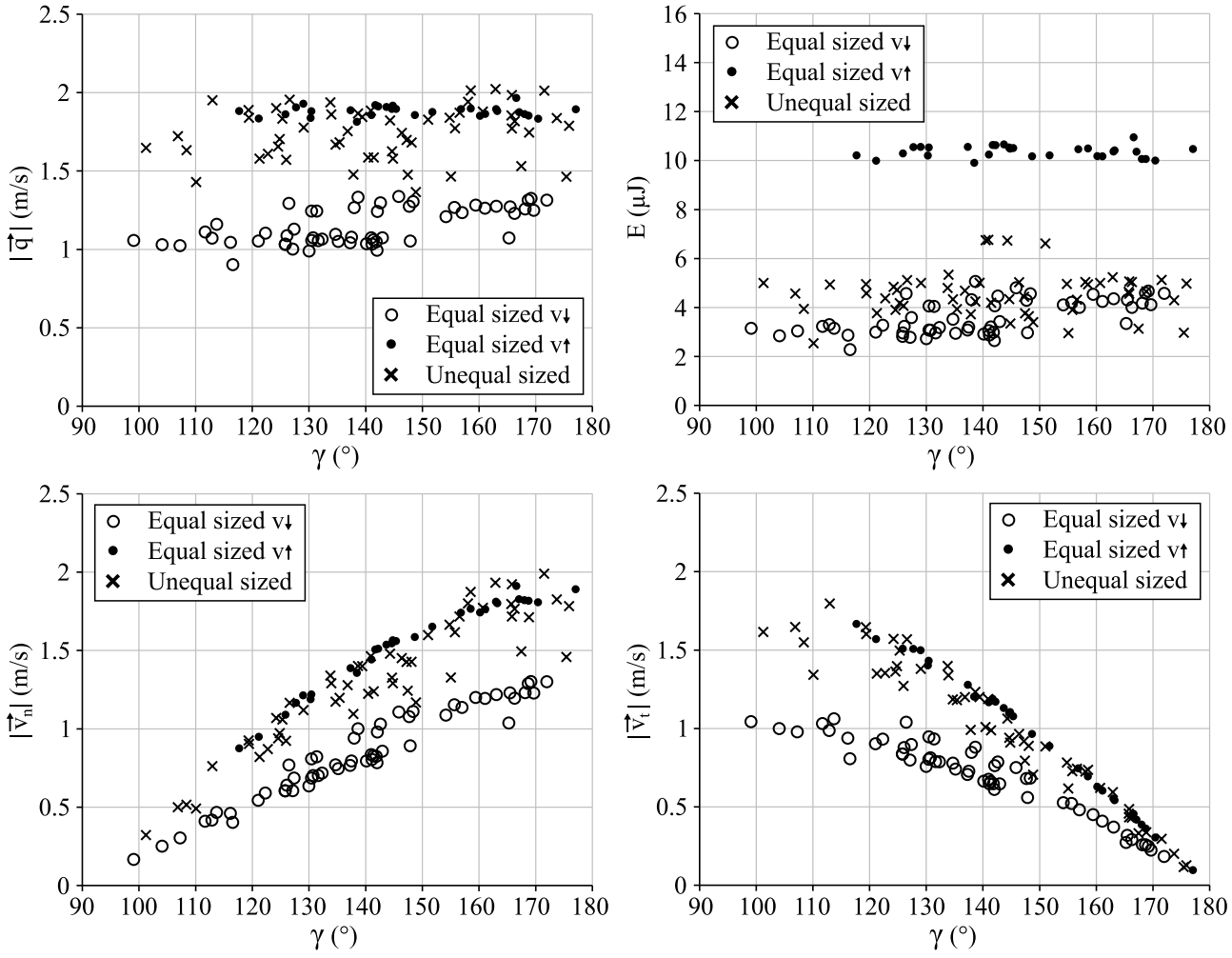

Fig. 29. Impact velocities and energy data of the evaluated dry collision experiments against the impact angle. Total impact slip velocity (top left). Total kinetic impact energy (top right). Total normal velocity at impact (down left). Total tangential velocity at impact (down right).

Table 5
Model parameters and collision properties.

Variable	Value	Unit
e	0.998	–
β_0	0.406	–
μ_0	0.109	–
γ_0	151.63	°
γ	$99.1 \leq \gamma \leq 177.1$	°
$\lvert\vec{v}_n\rvert$	$0.167 \leq \lvert\vec{v}_n\rvert \leq 1.991$	m/s
$\lvert\vec{v}_t\rvert$	$0.097 \leq \lvert\vec{v}_t\rvert \leq 1.797$	m/s
$\lvert\vec{q}\rvert$	$0.902 \leq \lvert\vec{q}\rvert \leq 2.023$	m/s
E	$2.285 \leq E \leq 10.951$	μJ

Table 5. The parameters were determined using data from both equal and unequal sized particle collisions. The model parameters were determined by parallel minimization of the root mean squared error for the curves of e, β, μ and Ψ_2.

Fig. 30 shows the plot of Ψ_2 against Ψ_1 as suggested by Foerster et al. [48] after equation (38) and (39) across all measurements, both for the equal sized particle collisions and for the unequal sized collisions in comparison to the model prediction after equation (40). Considering the whole range of measured values, the model predicts a hook-shaped progression. The first region, with Ψ_1 less than the limit value of 0.54, is the region of rolling particle contact. Here, Ψ_2 shows a linear decreasing curve according to equation (40) for $\gamma > \gamma_0$. In the region of rolling contact, the measured values follow the model prediction with very good accuracy and low scatter. A significant different behavior of the collisions depending on the size pairing or collision velocity is not evident. Above the limit value of 0.54 for Ψ_1, the region of the sliding contact is located. Here, Ψ_2 shows a linear increasing curve according to equation (40) for $\gamma \leq \gamma_0$. In this region, the values over all measurement series also follow the model prediction, but the scatter is considerably higher. The scatter is equally high for all measurement series. A systematically different course or a significantly different scatter depending on size pairing and collision velocity cannot be clearly identified.

The coefficient of friction shows a similar behavior. The course of the friction coefficient as a function of the collision angle is shown in Fig. 31. The theoretical curve is plotted according to equation (45), the measured values were determined according to equation (44). The exchanged momentum required for equation (44) can be determined from the measured motion data using the following equation:

$$\vec{J} = m_1 \bullet \left(\vec{v}_1' - \vec{v}_1\right) = m_2 \bullet \left(\vec{v}_2 - \vec{v}_2'\right). \tag{52}$$

The term $\vec{n} \times \vec{J}$ can in turn be determined according to the following equation:

$$\vec{n} \times \vec{J} = \frac{2 \bullet I_1}{d_1} \bullet \left(\vec{\omega}_1 - \vec{\omega}_1'\right) = \frac{2 \bullet I_2}{d_2} \bullet \left(\vec{\omega}_2 - \vec{\omega}_2'\right). \tag{53}$$

$\vec{J}$ and $\vec{n} \times \vec{J}$ can be calculated according to equation (52) and (53) for both particles and should be equal for both particles. Due to slight scatter in the measurements, this is not exactly the case, even though the values are often very close to each other. Therefore, the mean values from the data of the two particles are used in the following. In the region of rolling contact, there is a very good agreement between model and measurement with only slight scatter, similar to Fig. 30. In the region of

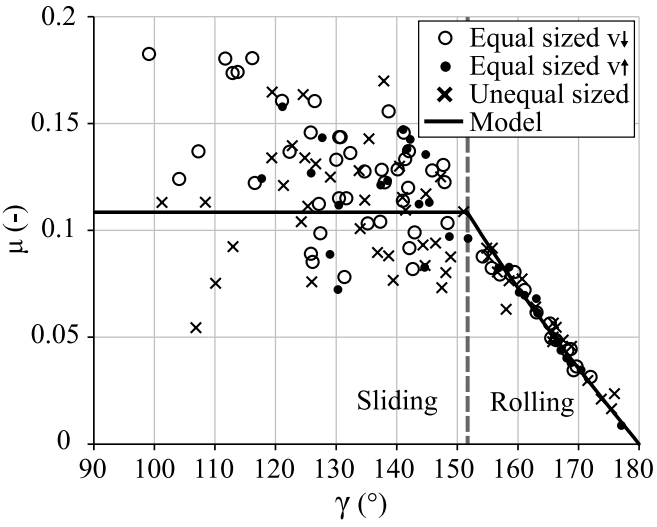

Fig. 31. Friction coefficient in dependence of the collision angle.

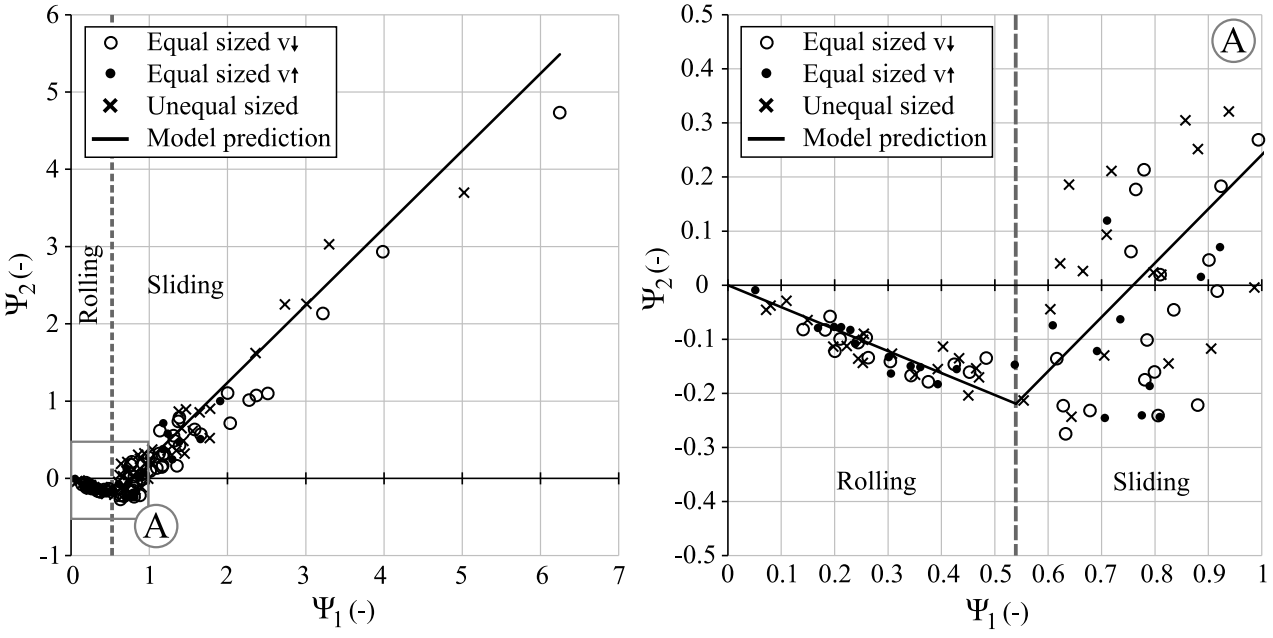

Fig. 30. Plot of Ψ_2 over Ψ_1. Comparison of measured and model predicted values for all datapoints (left). Close-up of the section A (right).

the sliding contact, there is a strong fluctuation of the measurements around the value predicted by the model. The strong scatter in the sliding contact region in Fig. 30 and Fig. 31 may be due to the complexity of the friction between the colliding surfaces. In the region of the sliding contact, the tangential force or momentum is limited by Coulomb's law of friction. The coefficient of friction thus determines the magnitude of the tangential momentum exchanged. The coefficient of friction depends on local properties of the collision surfaces, such as the surface structure [105]. Due to the high Young's modulus of the material, the contact area is expected to be very small, making local differences in surface structure significant. As previously observed in Fig. 30 for the plot of Ψ_2 over Ψ_1, no clear difference in the course and scatter between the measurement series can be identified for the coefficient of friction as well.

Fig. 32 shows the course of the tangential restitution coefficient β as a function of the collision angle as a comparison of the theoretical course according to equation (43) with the measured values according to equation (41). The data of all measurement series basically follows the theoretical curve. There is no difference between the measurement series. This also mainly applies to the scatter in the measurement data, which shows a significant scatter in both the rolling and sliding contact regime, in contrast to the previously considered curves. One outlier in the unequal sized collision series at a collision angle of $\gamma = 147^{\circ}$ is particularly noticeable. This value is approximately 0.5 smaller than the model prediction. Considering the theoretically possible value range of $-1 \leq \beta \leq 1$, this represents a remarkable error. Already in Fig. 31 a few outliers of unequally sized collisions occur, even in the rolling contact region that was previously depicted so precisely. The fact that the unequal sized collisions in some cases show a greater scatter than the equal sized collisions is due to the smaller particles. As can be seen in Table 1, the manufacturer's size and shape specifications for the 1 mm particles are not as precise as those for the 1.5 mm particles. This means that greater deviations in sphericity are to be expected than with the 1.5 mm particles, even if the manufacturing accuracy of the 1 mm particles is nevertheless extremely high. A second reason is the surface roughness. As mentioned in the chapter on materials, both particle variants have been prepared with the same surface treatment and therefore have a comparable surface roughness. Sommerfeld et al. [22] as well as Krull et al. [32] used particle–wall collisions to show that surface roughness leads to a strong increase in the scattering of motion after the collision. Sommerfeld et al. [22] also showed that the influence of roughness increases at smaller particle size to roughness ratios. In the rolling contact regime, the results are in contrast to the results of Labous et al. [49]. There, for collision investigations of nylon spheres with a diameter of 25.4 mm and comparable collision velocities, a tendency to a re-drop of β was found at high collision angles. This cannot be confirmed here. It should be noted, however, that the particle size and thus the impact energy is much lower in the current study and the Young's modulus of the material used here is about 100 times higher. As with the studies by Labous et al. [49], the results show an increase in scattering of β when approaching a collision angle of 180°.

According to the model, the coefficient of restitution in the normal direction should remain constant over the collision angle and assume values between zero and one. In our case, it is 0.998, just below one. The order of magnitude was confirmed by control measurements of the normal coefficient of restitution of 1.5 mm particles against a glass plate with dimensions 80 mm x 80 mm x 10 mm (L x W x H) for impact velocities between 0.52 m/s and 2.03 m/s. Across 75 individual tests, an impact velocity-independent coefficient of restitution in the normal direction of 0.984 with a standard deviation of ± 0.022 was obtained. The particle behavior can therefore be classified as almost ideally elastic.

As shown in Fig. 33, measured values and model parameters are close to each other and, moreover, no strong dependence on the collision angle is visible over a wide angular range. Again, all series of measurements show the same basic behavior. The agreement is particularly good again in the rolling contact region. The scattering increases in the sliding contact region, as in Fig. 30 and Fig. 31. In the case of the restitution coefficient in the normal direction, there are some significant outliers in the unequal sized collisions over the entire collision angle range. This reinforces the assumption that the higher roughness in relation to the particle diameter and the lower sphericity can lead to strong scatter. Although not as strong and mainly in the sliding contact region, there are also some deviations in the slower equal sized collisions. This could be due to a velocity-dependent effect in the presence of roughness. According to the experimental and simulation studies of Montaine et al. [31] on dry particle–wall collisions, in the presence of roughness, a lower impact velocity in the normal direction leads to a higher fluctuation of the normal coefficient of restitution. Since the normal component of impact velocity decreases with increasing impact angle in our experiments, this may explain why these deviations tend to occur at higher collision angles. Even in the equal sized collision at a higher speed, there was a unique outlier with a value that was significantly too low. Such random errors cannot be ruled out due to, for example, breaking or plastic deformation of asperities. In addition, despite our efforts to apply the rotation markings in such a way that the surface structure and material properties on the surface are only minimally influenced, it cannot be ruled out that a direct impact on a rotation marker will cause damping or chipping. This in turn inevitably leads to

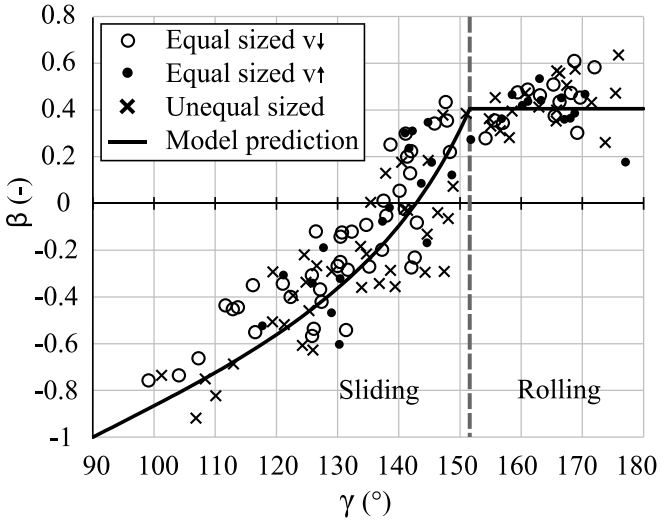

Fig. 32. Tangential coefficient of restitution in dependence of the collision angle.

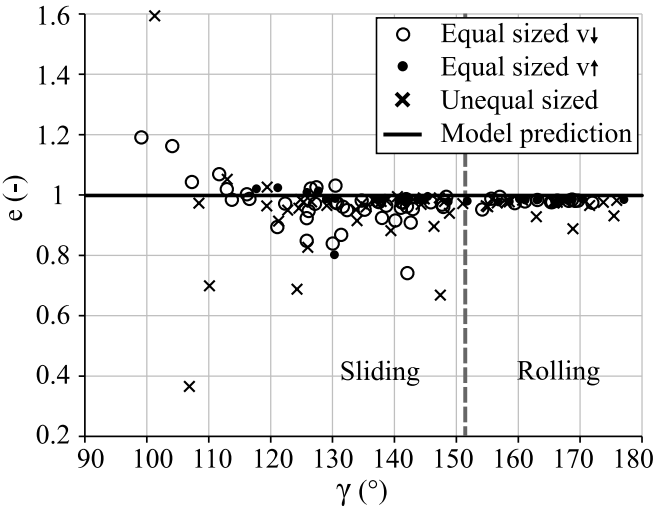

Fig. 33. Coefficient of restitution in normal direction over collision angle.

increased energy loss, also in the form of a too small restitution coefficient. Interestingly, measured values above one occur. This is the case exclusively in the region of sliding contact. While some values in the range of $105^{\circ} \leq \gamma \leq 130^{\circ}$ are only very slightly above one, which could be attributed to the measurement tolerance for such a high coefficient of restitution, the measured values are clearly above one for an angle $\gamma < 105^{\circ}$. The phenomenon of a coefficient of restitution greater than one has already been observed experimentally by Louge et al. [14] in collisions of a sphere against an inclined plate and by Chatterjee et al. [30] in collisions of thin circular disks against a wall. In addition, Kuninaka and Hayakawa [106–108] have been able to qualitatively support this phenomenon and the experimental observations in several 2D simulation studies. Accordingly, this only occurs in the case of sliding contact, in the case of very oblique collisions, i.e. low collision angles. The reason for this is the local deformation of the contact zone and the associated shift in the normal vector [14,106–108]. Since the model used is a hard sphere model, i.e. the momentum exchange is considered instantaneous without temporal resolution and neither deformation nor overlapping of the particles is allowed, such possible effects are not covered by the model.

The authors are not aware of any previous observation of this phenomenon in free, binary particle collisions. In contrast to previous investigations, the current investigation focusses on collisions of particles of the same material with a very high Young's modulus. The sphere used by Louge et al. [14] had a significantly higher Young's modulus than the target plate, which experimentally and simulated [108] revealed a steady increase of the normal coefficient of restitution with increasing collision angle. Chatterjee et al [30] used an inverse relationship, where the Young's modulus of the disc was significantly smaller than the Young's modulus of the target wall. Experimentally and simulation based [106] an almost constant normal coefficient of restitution was found there, which suddenly increases from a collision angle of less than approx. 105°, similar to our measurements.

Louge et al [14] have shown that in sliding contact collisions, a restitution coefficient below one is not a condition for energy loss in a collision. In Fig. 34 the efficiency of the collisions is plotted as a parity diagram. Model-based values and our measured values are compared here. The collision efficiency is defined as the ratio of kinetic energy after the collision to before the collision according to Equation (47). The energy difference predicted by the model can be calculated using Equations (48) to (51). Kinetic energy must always be lost due to a collision, so the efficiency must always be less than one. Fig. 34 shows that the measurements always fulfill this condition, which confirms the physical reasonableness despite the normal coefficient of restitution being sometimes higher than one for strongly oblique collisions.

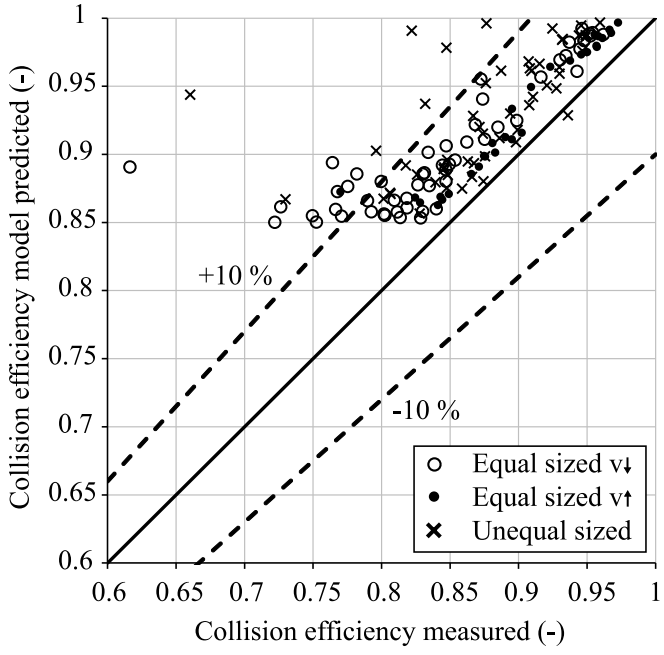

Fig. 34. Parity plot of the collision efficiency.

Fig. 34 also shows that the model underestimates the energy loss with the fitted model parameters. The measurements show a systematically higher energy loss due to the collision than predicted by the model. The reason for this lies in the model assumption of an ideal smooth, homogeneous sphere. It has already been explained that this does not correspond to reality. Manufacturing tolerances ensure an almost, but never ideal, spherical shape. The surface roughness leads to a changed collision geometry. The model assumes that the centers of mass of the spherical particles and the collision point lie on a straight line. This is not necessarily the case due to the non-ideal spherical shape and surface roughness. This means that the mechanisms for converting translational energy into rotational energy and vice versa change, which inevitably leads to errors in the prediction. As reported by Krull et al. [32], roughness tends to lead to an increased loss of kinetic energy in a collision under dry conditions, which is consistent with our results. At the microscale, many possible collision scenarios can occur that are not covered by the currently used model. This also includes the possibility of plastic deformation or breakage of the roughness, as well as possible influence by the applied rotation markings, which could explain the two extreme outliers. In addition to the energy loss predicted by the model, there is a random roughness and non-sphericity induced loss or error.

For the system variables considered so far, it was shown that the model can reproduce the basic course with a certain degree of scatter. However, conclusions about the correct prediction of the motion of the individual collision partners are only possible indirectly. Therefore, the translational and rotational motion of the individual particles will be checked for agreement with the model prediction in the following. For this purpose, the velocity vectors of the translational motion and the rotation are compared with the model prediction according to magnitude and direction. The directional comparison is performed by determining the angles between the predicted and measured vectors. Fig. 35 shows the comparison of the amounts of the translational velocity vectors as a parity plot for every particle. It shows an overall good agreement with only very few measurements outside a tolerance of ± 10 %.

Table 6 shows the angular deviation of the velocity vectors as 25 %, 50 %, and 75 % quantiles broken down by size pairing and particle size. A good agreement of the direction of translational motion over all measurement series is shown at a deviation of about 1° or less for 50 % of the respective measured values.

Fig. 36 shows the parity plots of the rotational velocities after the collision divided into collisions with rolling and sliding contact. An agreement in principle between measured and predicted values is given for rolling and sliding contact. The scatter of the values is clearly more significant for the rotation than for the translational velocity measurement in both contact regimes. Nevertheless, there is a clear difference in the scatter between rolling and sliding contact. As has already been observed in the analysis of the curves presented so far, the scattering in the rolling contact regime is significantly lower. According to the measurements, roughness seems to have a stronger influence on the collision behavior in sliding contacts.

In Table 7, the angular deviations of the rotation vectors are shown as quantiles, as previously illustrated in Table 6 for the translational velocity. While the deviation of the angle for rotation is comparably small for the equal sized collision pairings, as in the translational velocity analysis, the deviation is significantly increased for the unequal sized collision pairings. Here, angular deviations of up to 4.55° occur for 50 % of the measurements while the deviations for the equal sized collisions is only around 1.5° or less for 50 % of the measurements. As the small particles in unequal sized collisions are less well resolved in the camera images, a certain degree of increased measurement inaccuracy

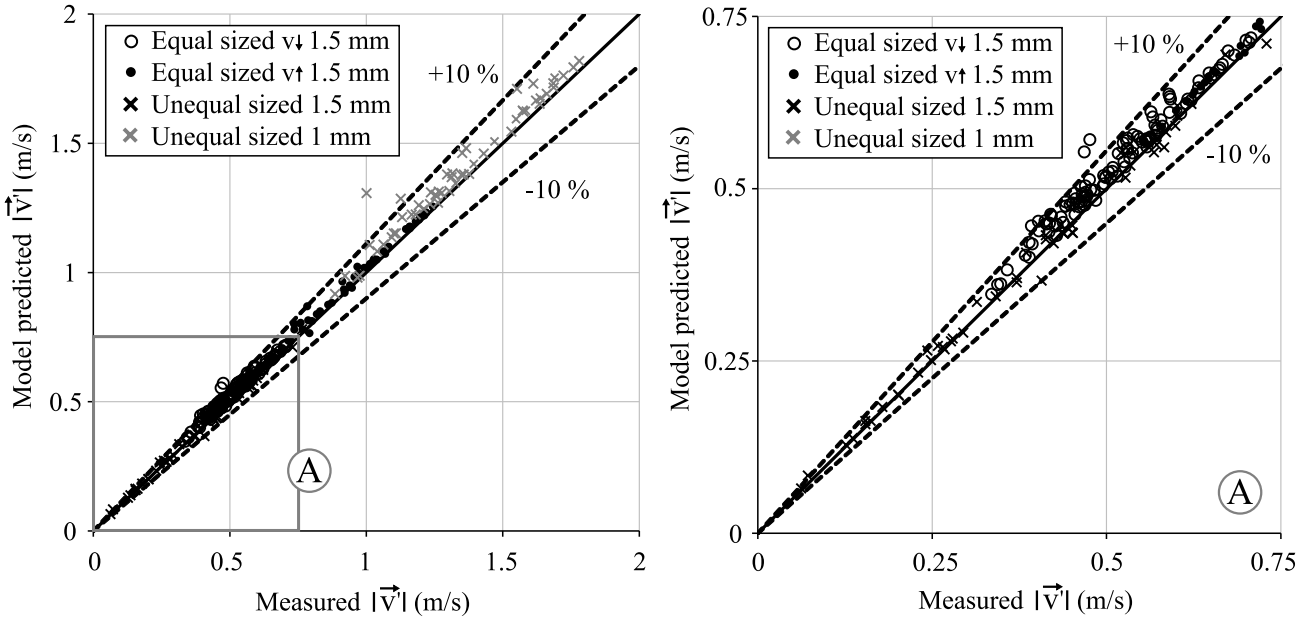

Fig. 35. Parity plot of the magnitude of the rebound velocity vectors for all datapoints (left). Close-up of the section A (right).

could be assumed for these. However, as the deviations of the better resolved large particles in the unequal sized collisions are very similar to those of the small particles, no significant influence of the measurement accuracy can be observed. This observation again supports the theory that the roughness influence of the smaller particles is stronger for the same roughness depth. According to the measurement data, the roughness in the ranges and conditions investigated here has a particularly strong effect on the deviation and scattering of the rotational movement.

In summary, the observations indicate that the model used can reproduce the basic outcome of the collisions investigated with limitations. All series of measurements follow the basic course of the model prediction without any systematic, detectable differences between them. Within the collision conditions investigated here, no clear influence of the collision speed or impact energy on the model parameters can be identified. Secondary influences, such as an increased scattering of the restitution coefficient at low normal velocities, are nevertheless recognizable. A systematic difference in the prediction accuracy for unequal sized collisions compared to equal sized collisions could not be determined within the scope of the study. The unequal sized collisions could be predicted with the same model parameters as the equal sized collisions without recognizable systematic deviations. All experimental observations made are under the influence of a non-negligible scatter, which is due to surface roughness and non-idealities of the assumed particle shape. The scatter and thus the influence of roughness is less significant in the rolling contact regime than in the sliding one. In the case of the collisions carried out here with no or very low initial rotation, the difference between the contact regimes becomes particularly clear in the case of rotation. While the prediction accuracy of the translational velocity in magnitude and direction was found to be very good across both collision regimes, the rotation shows a significantly low scatter in the rolling compared to the sliding contact regime. In general, however, the observed scatter in the rotation after the collision is significantly higher than the scatter of the translational motion. Although there is no systematic difference in the behavior of unequal sized collisions compared to equal sized collisions within the performed conditions, there is still a tendency for unequal sized collisions to have an increased scattering. This can be attributed to the increased ratio of roughness depth to particle diameter for the smaller particles. In agreement with observations from Krull et al. [32], a roughness-induced, systematic underestimation of the loss of kinetic energy due to the collision could be observed. Breakage of the asperities, as well as possible influences of the applied rotational markings, can lead to seemingly random outliers with significantly increased energy loss due to the collision. The model used does not represent surface roughness or non-idealities of the spherical shape. In order to include these, model extensions such as those suggested from Montaine et al. [31] and Glielmo et al. [109] could be considered.

6.2. Wet collisions

For a direct comparison between dry and wetted collisions, two series of measurements of wetted collisions between equal sized particles with different liquid layer thicknesses were performed. One particle was wetted, the second remained dry. The particles used are the same 1.5 mm zirconium oxide spheres as used in the dry collisions, with the same surface roughness. The fluid used in both cases is a silicone oil with a dynamic viscosity of 18.9 mPa•s at *25 °C*. The first series of measurements, consisting of 60 collisions, was carried out with an increased liquid layer thickness within a range of 150.0 ± 10.0 µm, which is why this series is labeled σ↑ in the following figures. The second series of measurements, consisting of 26 collisions, was performed with a smaller liquid layer thickness within the range of 85.7 ± 14.0 µm and is marked σ↓ in the following figures. The relative collision speed at the contact point was kept almost constant at 1.19 ± 0.04 m/s for the first and 1.22 ± 0.05 m/s for the second series, which is similar to the dry measurement series with the lower speed. The initial rotation of both particles was neglectable small at 13.72 ± 11.3 1/s, averaged over all measurements.

In contrast to dry collisions, additional forces occur in wetted collisions due to the liquid, which influences the movement of the particles. On the one hand, viscous damping forces occur that counteract the approach and separation of the particles due to the displacement and deformation of the liquid [110]. On the other hand, attractive capillary forces act due to the concave form of the liquid bridge [111]. The ratio of viscous to capillary forces is described using the dimensionless capillary number Ca [71]:

$$Ca = \frac{3 \bullet \eta \bullet \left| \vec{v}_n \right| \bullet r^*}{\gamma \bullet \sigma}, \tag{54}$$

where r^* is the reduced radius:

Table 6
Angle deviation of the rebound velocity vectors.

Quantile	Equal sized (1.5 mm)	Unequal sized (1.5 mm)	Unequal sized (1 mm)
25 %	0.50°	0.52°	0.48°
50 %	1.28°	0.99°	0.87°
75 %	2.55°	2.30°	2.44°

$$r^* = \frac{r_1 \bullet r_2}{r_1 + r_2}. \tag{55}$$

The higher the capillary number, the more dominant the viscous damping forces are compared to the capillary forces. According to Davis [112], capillary forces can be considered neglectable at Ca > 1000 for linear collisions, whereas studies by Donahue et al. [73] show that capillary forces are generally relevant for oblique collisions. With the capillary numbers in the range between 3.7 and 17.7 over both series of measurements carried out here, a significant influence of both forces is to be expected, regardless of whether an oblique or head-on collision is occurring.

In addition, previous studies used the Stokes number in normal direction St_n as another dimensionless parameter to compare wetted collisions. This parameter describes the ratio of inertial forces to viscous forces in the normal direction [56,71,74,113]:

$$St_n = \frac{\left|\vec{v}_n\right| \bullet m^*}{6 \bullet \pi \bullet \eta \bullet r^{*2}}. \tag{56}$$

Fig. 37 shows the impact conditions of the collisions for both series of measurements.

As the movement of the particles through the liquid layer cannot be adequately recorded due to the insufficient temporal resolution of the measurements, the evaluation of the measurement data is limited to

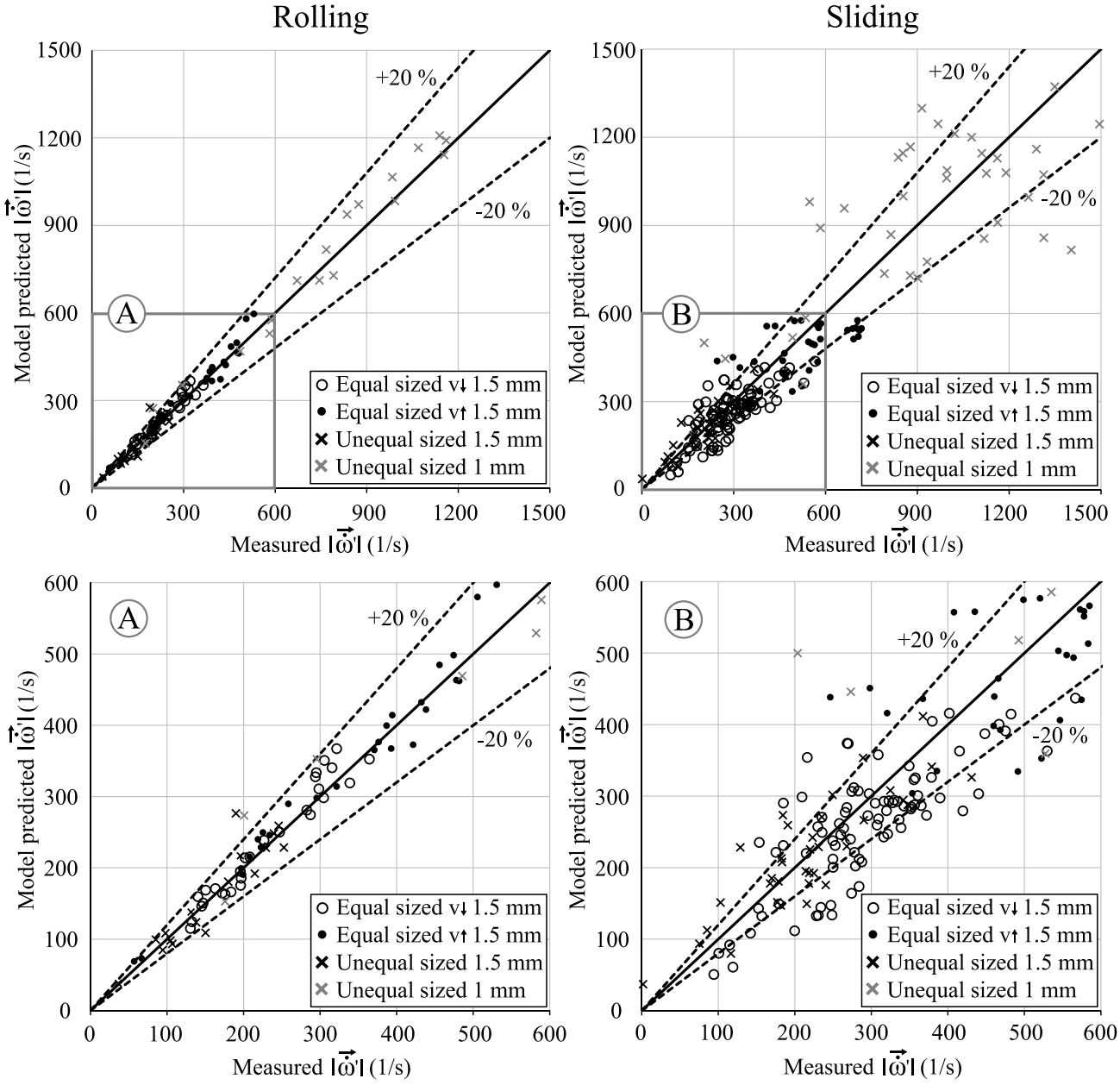

Fig. 36. Parity plot of the magnitude of the rebound rotation vectors divided into collisions with rolling and sliding contact. Rolling contact, total view (top left). Sliding contact, total view (top right). Rolling contact, close-up of the section A (down left). Sliding contact, close-up of the section B (down right).

Table 7
Angle deviation of the rebound rotation vectors.

Quantile	Equal sized (1.5 mm)	Unequal sized (1.5 mm)	Unequal sized (1 mm)
25 %	0.95°	2.50°	2.38°
50 %	1.48°	4.55°	4.10°
75 %	2.54°	10.01°	7.28°

effective values before and after the collision. For this purpose, the liquid layer is initially assumed to be a rigid, homogeneously distributed, resistance-free layer around the particle for determining the collision data. It is also assumed that it does not change as a result of the collision, i.e. no liquid is exchanged between the wet and dry particle, no liquid bridge is formed and no liquid splits off in the form of a satellite droplet. The additional mass and the additional moment of inertia of the liquid layer with moistened particles is taken into account. Due to the assumption that the liquid layer is rigid, it is also assumed that the liquid follows the particle rotation directly without a velocity gradient within the liquid layer. As with dry collisions, the point of collision is defined as the contact between the surfaces of the particles.

The plot of Ψ_2 against Ψ_1 in Fig. 38 shows that the wetted collisions follow the same basic trend as the dry collisions under the collision conditions considered. The two regimes of rolling and sliding contact can also be observed for wetted collisions. For small values of Ψ_1, the rolling contact regime, the trend for Ψ_2 is steadily decreasing up to a limit value of Ψ_1, from which Ψ_2 steadily increases in the sliding contact regime. No significant difference can be seen between both measurement series in this plot. Compared with the model trend for dry collisions, shown in this and all subsequent figures as a solid black line, there is a clear reduction in the limit value of Ψ_1 for the transition from the rolling to the sliding contact regime. In turn, this means an increase in the limit angle γ_0. In other words, a noticeably earlier transition to the sliding contact regime in the case of oblique collisions is observed. Another significant difference to the dry collisions lies in the scatter of the measured values. The scatter of the measured values in the rolling contact regime is relatively low for both dry and wetted collisions. The scatter of the measured values for the wetted collisions in the sliding contact regime is comparably low as in the rolling contact regime, in contrast to the dry collisions, which have a significantly higher scatter in the sliding contact regime. The reason for the earlier transition to the sliding contact regime and the reduced scattering of the data can be found in the effect of the liquid as a lubricant. The type of friction between the particle surfaces thus changes from pure dry surface friction to liquid supported mixed or elastohydrodynamic friction [114]. The friction is thus reduced and the influence of the roughness profile of the solids is decreased.

Due to the very similar trend of the wetted and dry collision data, an attempt is made to adjust the parameters of the model for the dry collisions to the measured values of the wetted collisions. The adjustment is made separately for each of the two wet measurement series. The model remains unchanged. The resulting adjusted model parameters and the associated collision parameters are listed in Table 8 and compared with the values of the dry collisions. The model curve adapted to the measurement series with increased liquid layer thickness is shown in all figures as a black, dashed line, the model curve adapted to the measurement series with lower liquid layer thickness as a gray, dotted line. By adjusting the model parameters, the plot of Ψ_2 over Ψ_1 shows that the model can reproduce the course to a good approximation. Just like the measurements, the model curves of the wetted collisions show no significant difference in this graph. After adjusting the model parameters, the shifted limit angle for the transition from the rolling to the sliding contact regime becomes clear. The limit angle has increased from the original 151.6° for the dry collisions to around 161.8° for the wetted collisions.

Nevertheless, there are differences in the model parameters and in the collision behavior. Fig. 39 shows the course of the measured restitution coefficients in the normal direction over the collision angle. In comparison, the measured restitution coefficients in the normal direction of the wetted collisions are systematically and significantly lower than those of the dry collisions. This is in line with expectations due to the additional resisting forces caused by the liquid and is consistent with the observations of previous studies [57,64–66]. The collisions with a higher liquid layer thickness also exhibit a lower restitution coefficient in the normal direction and thus a higher loss of kinetic energy than with a smaller liquid layer thickness. This is consistent with the observations of previous studies on wetted collisions between particle and wall, such as by Buck et al. [52]. This correlation is also reflected in the fitted model parameters. The fitted restitution coefficient in the normal direction for the model is 0.754 for the case of increased liquid layer thickness and higher at 0.814 for the case of low liquid layer thickness. However, both are significantly below the value of the dry collisions of 0.998. The model assumes a constant coefficient of restitution in the normal direction. Previous studies on wetted collisions between particles and the wall [50,55,57,64,66] or between particles in a pendular setup [75] have shown that the coefficient of restitution in the normal direction depends on the impact velocity in the normal direction and thus on the Stokes number in the normal direction. Lower impact velocities in the normal direction and thus also lower Stokes numbers lead to lower restitution coefficients in the normal direction, which can lead to agglomeration below a critical velocity or Stokes number. This relationship is highly non-linear. This change in the coefficient of restitution is very pronounced close to the critical impact velocity or critical Stokes number [52,75]. At significantly higher normal velocities and Stokes numbers than the critical ones, the curve flattens out considerably. In the measurements carried out, the normal component of the impact velocity and thus also the Stokes number in the normal direction decreases the more oblique the collision is, i.e. the smaller the collision angle. An increasing trend of the restitution coefficient with increasing collision angle is therefore to be expected. This trend cannot be clearly identified from the measured values of both series of measurements. Although Stokes number and normal velocity at collision are not constant in the present measurements, they are of a similar order of magnitude over the entire range under consideration. It can therefore be assumed that all collisions carried out here are far away from agglomeration, which means that there is only a weak dependence on impact velocity and Stokes number in the normal direction. Thus, the assumption of a constant restitution coefficient for the narrow parameter range investigated here is fulfilled to a first approximation.

The wet collision measurements of the coefficient of restitution in the tangential direction and the coefficient of friction are shown in Fig. 40. In both curves, there is no clearly recognizable difference between the measurement series. Compared with the course of dry collisions, the differences are significant and clear for both the tangential coefficient of restitution and the coefficient of friction. The significantly lower scatter of the measured values of the wetted collisions in both graphs over the entire collision angle range compared to the measurements of the dry collisions is directly remarkable.

The measured values of the restitution coefficient in the tangential direction show an increasing curve with increasing collision angle in the sliding contact regime. The qualitative progression of the measured value curves in this regime is similar to the progression of the dry collisions. However, the values of the wet collisions are systematically below the values of the dry collisions. During the transition from the sliding to the rolling contact regime, a change in the course of the curve is recognizable, as with the dry collisions. While an almost constant value is formed in the rolling contact regime in the dry collisions, only a flattening of the curve slope occurs in the wetted collisions. There is a clear trend that the tangential restitution coefficient continues to increase with increasing collision angle. This behavior in the rolling contact regime is not reproduced by the model even after adjusting the

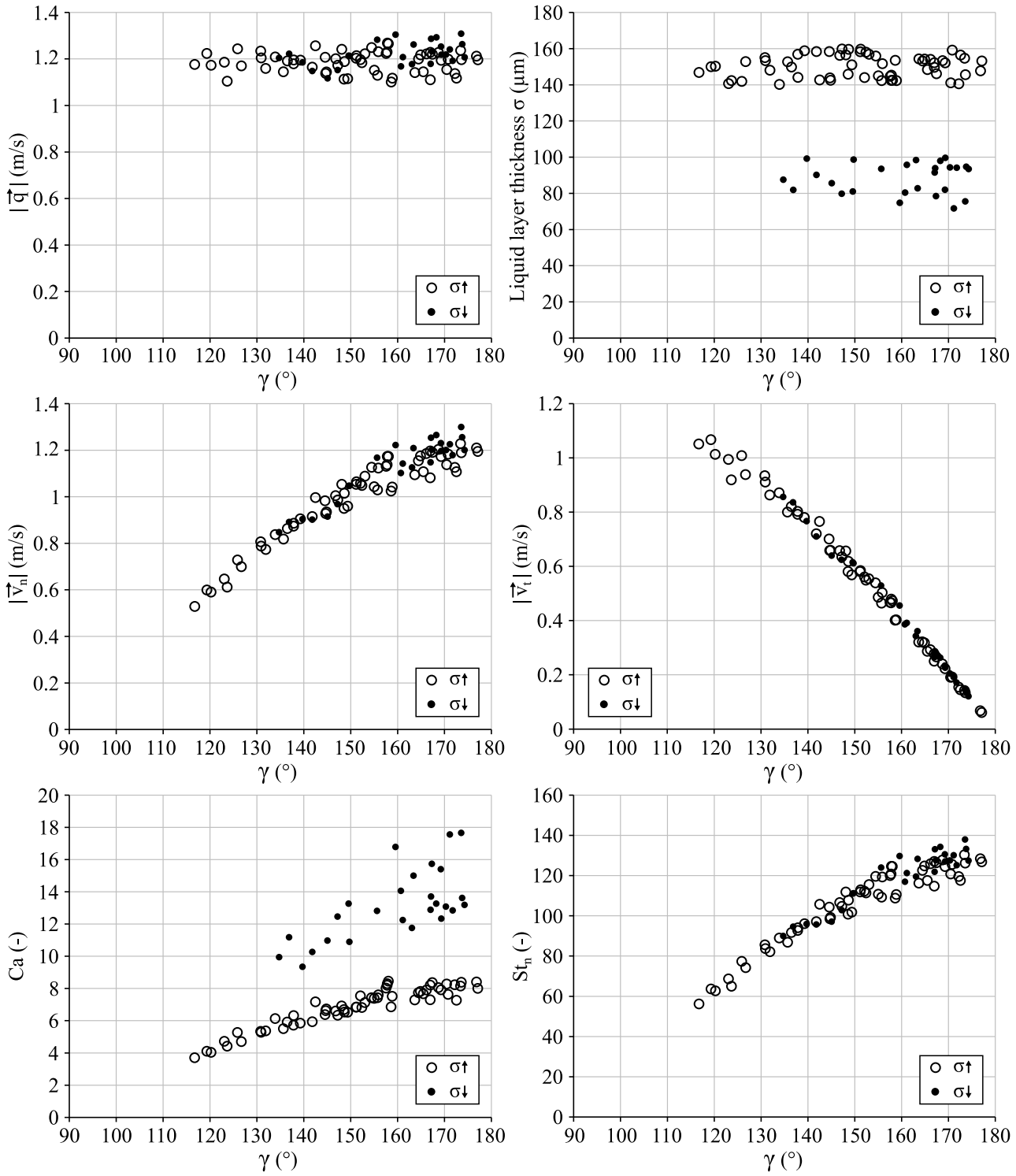

Fig. 37. Impact conditions of the evaluated wet collision experiments against the impact angle. Total impact slip velocity (top left). Liquid layer thickness (top right). Total normal velocity at impact (middle left). Total tangential velocity at impact (middle right). Capillary number of the collision (down left). Stokes number in normal direction at impact (down right).

model parameters to the wetted collisions.

At high collision angles, the measured values increase beyond the determined model parameter β_0, which is intended to represent the maximum tangential coefficient of restitution. However, the curve trend in the sliding contact regime can be reproduced to a good approximation after the parameter adjustment. The adjusted model parameter of the assumed maximum tangential restitution coefficient β_0 differs only slightly between the wetted collision measurement series with 0.436 for the case with lower liquid layer thickness and with 0.427 for the case with higher liquid layer thickness. Both values are higher than the value of 0.406 determined for the dry collision measurement series. Nevertheless, the difference in this model parameter between dry and wetted collisions can be considered small overall. It is difficult to compare the measured values with experimental information from previous studies. Wetted, binary interparticle collisions have so far been carried out in a pendulum setup, whereby the tangential restitution coefficient was

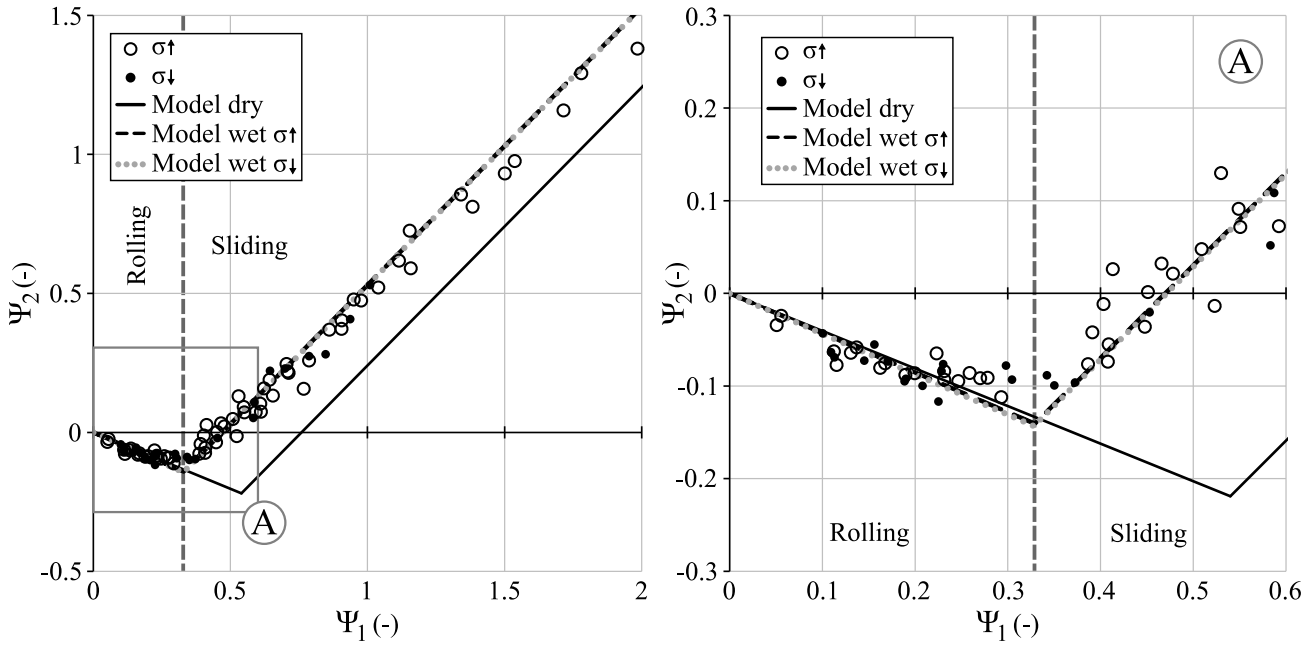

Fig. 38. Plot of Ψ_2 over Ψ_1. Comparison of measured and model predicted values for all datapoints for wet collisions (left). Close-up of the section A (right).

often not considered [72–74]. In the study of Yang et al. [75], the tangential movement was analyzed, but not compared with dry collisions. In addition, these investigations were carried out in a fully immersed liquid environment. Comparative studies of dry to wetted particle–wall collisions usually consider translational motion in the tangential direction and rotation separately [53,54]. The definition of the tangential restitution coefficient in these studies is different and therefore not directly comparable. Buck et al. [53] additionally defined a combined tangential restitution coefficient with a reversed sign in comparison with the current study. However, the collision angle was defined solely on the basis of the translational velocity vector, without including the initial rotation. This means that the measurements of Buck et al. [53] with initial rotation are not directly comparable. The comparable measured values of Buck et al. [53] without initial rotation show a strong scatter. Nevertheless, the mean values of the measurements of Buck et al. [53] confirm the tendency observed in the present study for the oblique, wetted collisions to have smaller values of the tangential restitution coefficient compared to the dry collisions.

The qualitative course of the coefficient of friction of the wetted collisions corresponds to that of the dry collisions in both contact regimes. In addition to the significantly lower scatter of the measured values, it is noticeable that the measured values in the slipping contact regime are significantly lower than those of the dry collisions. This is also reflected in the adjusted model parameters. While the coefficient of friction determined for the dry collisions is 0.109, it is significantly reduced for the wetted collisions to 0.074 and 0.077 for the measurements with lower and higher liquid layer thicknesses respectively. The difference in the coefficient of friction between the series of measurements of the wetted collisions is only minimal. The same applies to the curve approximated by the model. In the rolling contact regime, the measured values of the wetted collisions are slightly higher than those of the dry collisions. After adjusting the model parameters, the trend is reproduced very well here. In the sliding contact regime, the almost constant friction coefficient is slightly underestimated after the model parameter adjustment. This again indicates a systematic error in the model. The observed reduction of the friction coefficient in wetted collisions is consistent with previous observations from the literature [54] and supports the assumption of the lubricating effect of the liquid.

Despite the clear systematic limitations of the model used, the friction coefficient and the normal and tangential restitution coefficients for the narrow parameter range of the measurements considered here are still in acceptable agreement. This is also reflected in the direct comparison of the measured and predicted individual particle movements, as well as in the total loss of kinetic energy. Fig. 41 shows the direct comparison of the magnitudes of the measured and predicted translational and rotational motion vectors, as well as the energy loss in the form of the collision efficiency. For a closer look at the processes in the two contact regimes, the values in Fig. 41 are divided into the rolling and sliding contact.

The translational speed of both series of measurements could be reliably reproduced by the model in both contact regimes within a tolerance of ± 10 %. The scatter of the measured values is low in both contact regimes and comparable to that of the dry collisions. The rotational speed of both series of measurements is well reproduced within a higher tolerance of ± 20 % in both contact regimes with only very few outliers. The scatter in the rotational measurements is thus higher than in the translational speed measurements, like previously observed for dry collisions. However, in the sliding contact regime in particular, there is a significantly lower overall scatter in the measured values compared to the dry collisions. A systematic deviation can be recognized in the rolling contact regime. At low rotational speeds up to approx. 125 1/s, the model tends to underestimate the rotational speed after the impact. Above this value, a reversed tendency can be observed. As the measurements were carried out to a good approximation without initial rotation, low rotational speeds after the impact occur in the rolling contact regime with almost head-on collisions, i.e. very high collision angles close to 180°. The more oblique the collision in the rolling contact regime, i.e. the smaller the collision angle, the higher the rotational speeds. Looking at the trend of the tangential restitution coefficient in Fig. 40 in the rolling contact regime, a correspondence of the trends can be observed. In the slipping contact regime, in turn, the trend of the tangential restitution coefficient can be reproduced well, which also leads to no recognizable systematic deviation in the predictions of the rotational speed. A direct comparison of the measured rotational velocities of the wetted collisions with the dry collisions of the same size and impact velocity reveals a significant reduction in the resulting rotational velocity after the collision. In the dry collisions with very comparable collision parameters, maximum rotational speeds of up to over 500 1/s occurred, whereas in the wetted collisions a rotational speed of 300 1/s was only slightly exceeded once. This reduction in

Table 8
Comparison of the model parameters and collision properties between dry and wet collisions.

Variable	Value dry	Value wet σ↓	Value wet σ↑	Unit
e	0.998	0.814	0.754	–
β_0	0.406	0.436	0.427	–
μ_0	0.109	0.074	0.077	–
γ_0	151.63	161.84	161.78	°
γ	$99.1 \leq \gamma \leq 177.1$	$134.7 \leq \gamma \leq 174.3$	$116.7 \leq \gamma \leq 177.1$	°
$\lvert\vec{v}_n\rvert$	$0.167 \leq \lvert\vec{v}_n\rvert \leq 1.991$	$0.848 \leq \lvert\vec{v}_n\rvert \leq 1.300$	$0.529 \leq \lvert\vec{v}_n\rvert \leq 1.228$	m/s
$\lvert\vec{v}_t\rvert$	$0.097 \leq \lvert\vec{v}_t\rvert \leq 1.797$	$0.121 \leq \lvert\vec{v}_t\rvert \leq 0.856$	$0.061 \leq \lvert\vec{v}_t\rvert \leq 1.067$	m/s
$\lvert\vec{q}\rvert$	$0.902 \leq \lvert\vec{q}\rvert \leq 2.023$	1.221 ± 0.050	1.188 ± 0.043	m/s
σ	0	85.7 ± 14.0	150.0 ± 10.0	μm

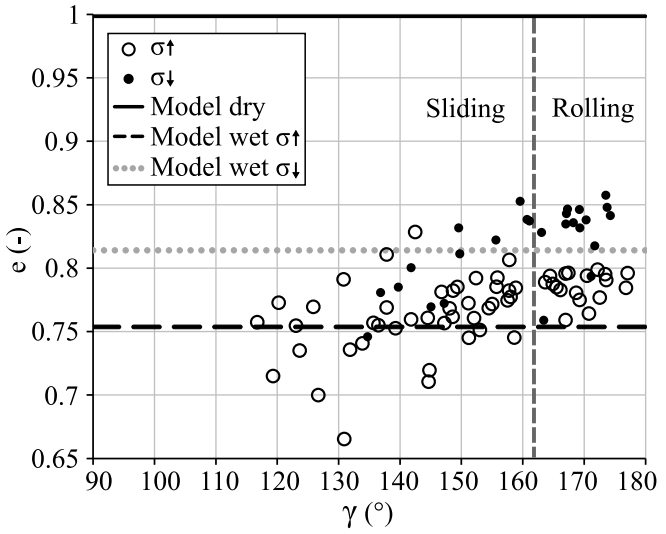

Fig. 39. Coefficient of restitution in normal direction for wet collisions over collision angle.

rotational speed after the impact in wetted collisions compared to dry collisions is consistent with former studies of oblique particle–wall collisions [54,59,67].

The consideration of the collision efficiency, which compares the total kinetic energy after the collision with the total kinetic energy before the collision, shows a significantly greater loss compared to dry collisions. Due to the fundamentally lower normal restitution coefficients and the lower tangential restitution coefficients over long distances compared to dry collisions, this is the logical consequence. In both contact regimes, the prediction accuracy of the model for both measurement series remains within a tolerance of ± 10 %, with one exception. The systematic underestimation of the model in the rolling contact regime is remarkable. Due to the high collision angle in the rolling contact regime, almost head-on collisions are occurring. This means that the coefficient of restitution in the normal direction dominates the description of the total energy loss. The comparison with the course of the normal restitution coefficient in Fig. 39 shows that the model parameter in the rolling contact regime is also systematically below the measured values. The difference in the normal coefficients of restitution between the two series of measurements becomes apparent again when considering the collision efficiency in the rolling contact regime.

Just as important as the prediction of the magnitudes of the vectoral velocities is the correct prediction of their directions. To assess the model's ability to predict the velocity directions, Table 9 summarizes the angular deviations between model and measurement for both translational and rotational motion. The deviations are shown as 25 %, 50 % and 75 % quantiles for every measurement series of wetted collisions. No significant difference between the measurement series can be observed. For the translational velocity, 50 % of the measurements are below an angular deviation of 1.3° or 1.4°, which corresponds to the level of the dry measurement series. In the case of rotation, 50 % of the measurements are below an angular deviation of approximately 2.5°, which is on average even better than for the dry collision experiments. This is due to the significantly lower scatter in the wetted collisions. Overall, the angular deviations can be classified as very low.

In summary, it can be concluded that, for the first time, free, wetted interparticle collisions were successfully carried out, fully measured and directly compared with dry collisions. The series of measurements carried out initially cover a very narrow range of collision conditions, which is why only initial trends can be analyzed. Nevertheless, the trends are consistent with previous observations from prior studies. The comparison of the measured values with a parameter-adjusted model, which was also used for the prediction of dry collisions, shows both partially consistent trends and systematic deviations. Dependencies, such as those of the restitution coefficient in the normal direction on the collision velocity in the normal direction, have not yet been taken into account. Other studies have already provided suggestions and approaches for predicting the restitution coefficient in the normal direction for wet collisions [50,57,59,60,66,68,115–118]. It is also necessary to identify, quantify and model the influences of the liquid layer on the tangential coefficient of restitution and the coefficient of friction and to integrate them into the collision model used in this study or an alternative one. A reliable confirmation or falsification of the previous prediction models of the restitution coefficient in the normal direction, as well as a modeling for the prediction of the other two parameters, is not yet possible due to the current data situation. For this, as well as to determine the range of validity of the collision model used or to identify a better model, further extensive experimental studies are required that cover a wide range of collision conditions. Despite the systematic deviations of the model from the measured data, the collision model used allows a good prediction accuracy of the particle movements after the collision in the narrow collision condition range investigated here. The measurements were carried out under collision conditions that are classified as far away from particle agglomeration. Thus, the current data situation does not allow any reliable statement about the prediction accuracy near the agglomeration regime.

7. Conclusion

An experimental setup was designed that allows free binary collisions of spherical particles to be performed. The range of functions has been significantly extended compared to previous experiments of free particle collisions [34,47–49]. These include the strong reduction of the minimum, fully measurable particle diameter to 1 mm, the possibility to collide particles with unequal diameters, the stereoscopic recording of the collisions with two highspeed cameras and the possibility to perform wetted collisions. Evaluation methods and algorithms based on digital image analysis were established and verified for the measurement of particle motion in all spatial directions, including rotation, and for the

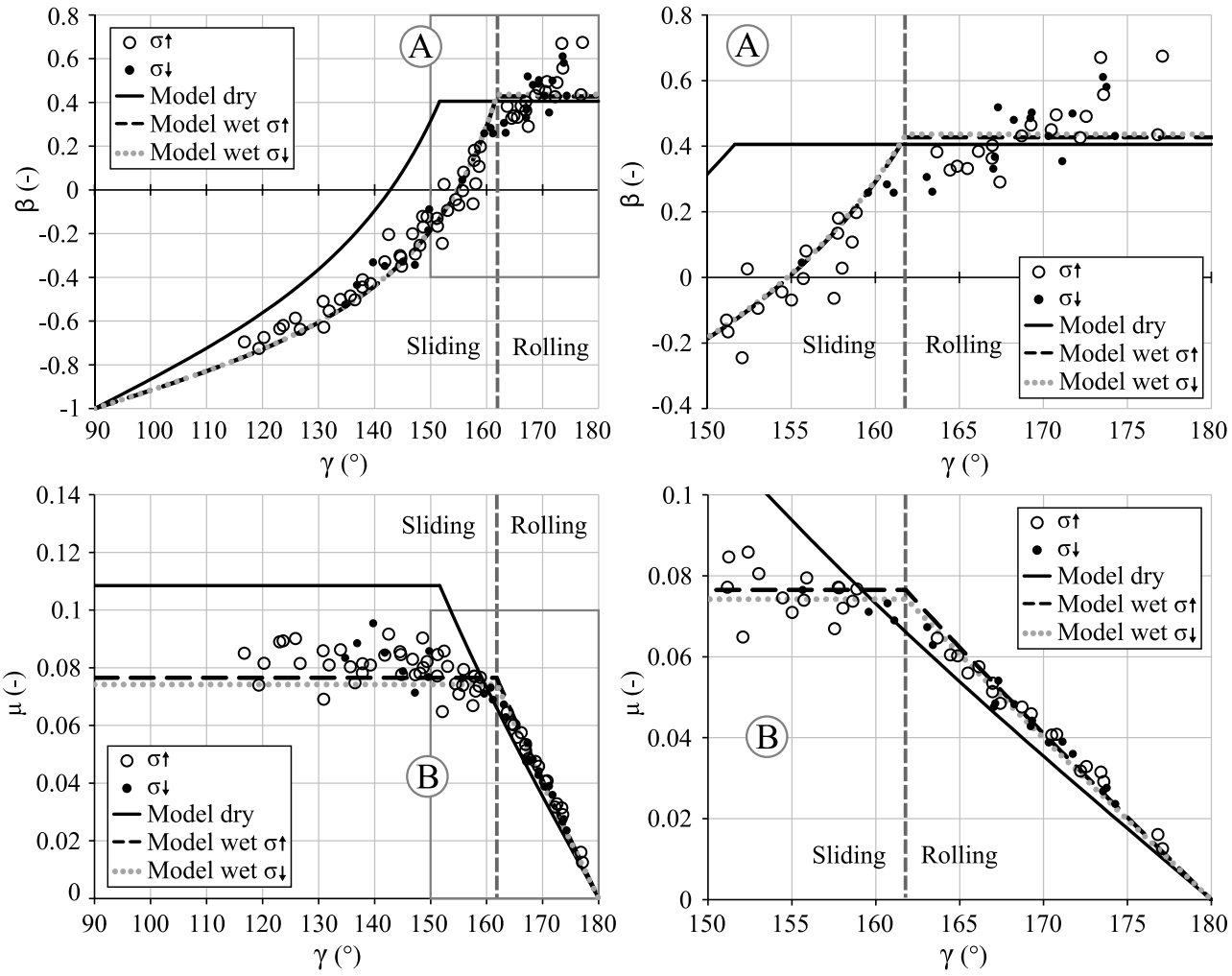

Fig. 40. Tangential coefficient of restitution and friction coefficient of wet collisions over the collision angle. Tangential coefficient of restitution, total view (top left). Tangential coefficient of restitution, close-up of the section A (top right). Friction coefficient, total view (down left). Friction coefficient, close-up of the section B (down right).

measurement of the amount of liquid on moistened particles, satisfying the high precision requirements of this experiment. In the case of the rotation analysis, it was possible to identify and eliminate distortion effects that would otherwise lead to strong deviations, especially, but not exclusively, for the measurement of wetted particles. Guaranteeing a reliable measurement of rotation, while simultaneously measuring the amount of liquid on wet particles using grayscale images constituted a major challenge. The authors were able to show that this problem could be solved using a Convolutional Neuronal Network for semantic segmentation, where the neural network was trained exclusively on animated, artificially generated image data.

The comparison of a large number of dry particle collision data, both between equal and unequal sized particles, over a wide range of collision angles with a three-parameter collision model according to Walton [76,77] showed a reasonable agreement. Thus, on the one hand, the collision parameters for the investigated zirconium oxide particles could be determined. On the other hand, the independence of the collision model and its parameters from particle size pairings could be confirmed.

As known from previous studies [14,30,106–108], we were able to confirm that the restitution coefficient in normal direction can become larger than one for very oblique dry binary interparticle collisions. Nevertheless, the total kinetic energy of the system always decreased. This observation occurred regardless of the size pairing of the collision partners.

Measurement series of wetted collisions enabled a direct comparison with the collision dynamics of dry collisions. Despite the limited range of collision conditions in these measurements under wetted conditions, initial trends could be derived regarding the restitution coefficients in the normal and tangential directions, as well as the friction coefficient. These trends are consistent with observations from the literature. It could be shown that the model used for dry collisions can also be used to describe wetted collisions with restrictions after parameter adjustment. Nevertheless, systematic deviations between measurements and model predictions could be identified. Further model comparisons and model adjustments are therefore necessary in the future. Similarly, a significant extension of the experimental investigation of wetted collisions to a wide range of collision conditions is necessary to identify the reliability and limitations of potential wetted collision models. The experimental setup presented enables the future execution of these measurements of wetted, binary particle collisions. It is thus possible to examine in detail the influence of the liquid on the collision behavior up to and including agglomeration. The investigation of the behavior of the liquid, such as liquid bridge formation, liquid bridge rupture, satellite drop formation and liquid exchange between dry and wet particles are further possible applications.

Funding

This work was funded by the German Research Foundation (DFG) via HE 4526/28-1.

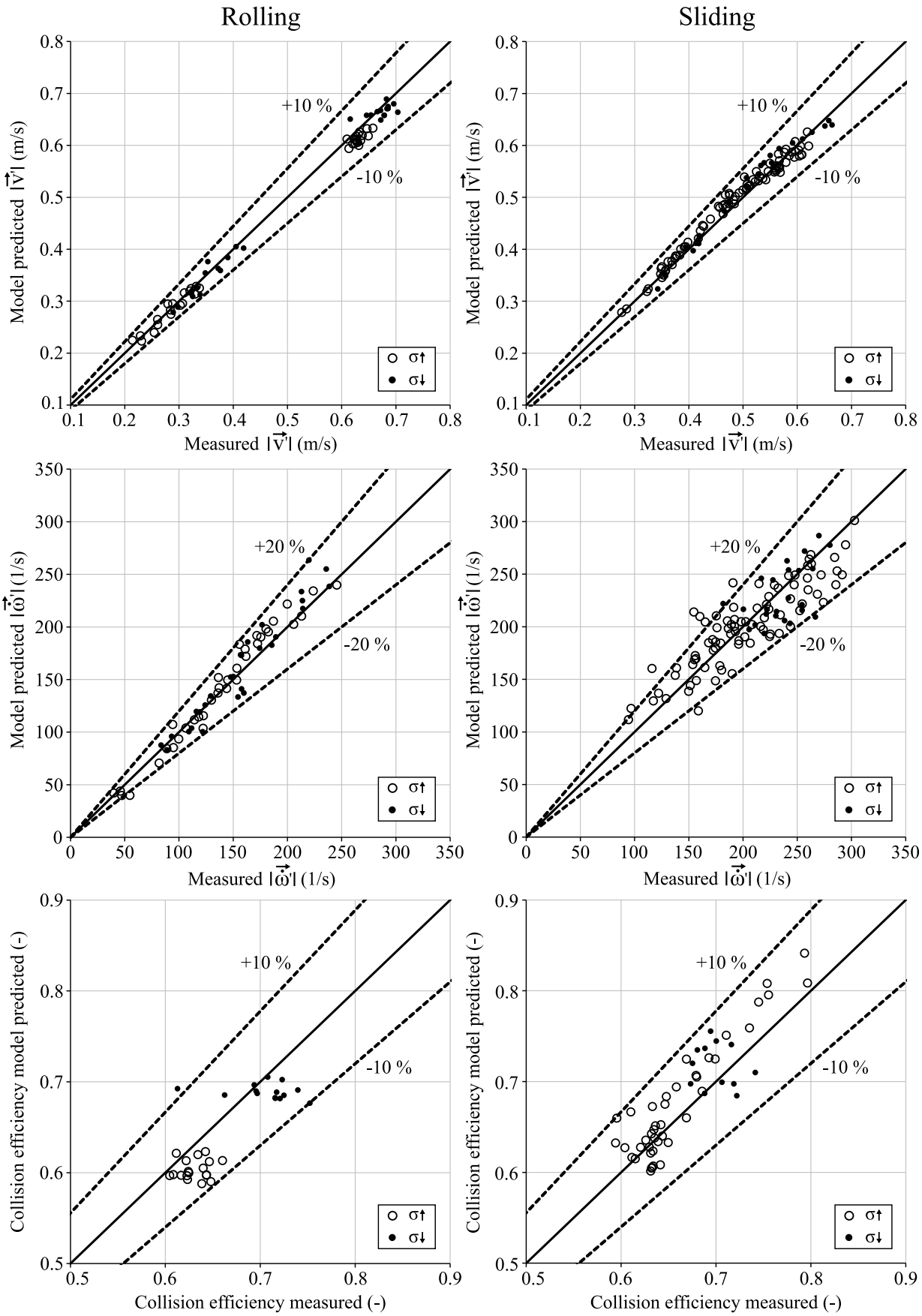

Fig. 41. Parity plots of the magnitude of the post-collisional tranlational velocity (top row), rotation (middle row) and collision efficiency (down row) divided in rolling (left column) and sliding (right column) contact regime.

Table 9
Angle deviation of the rebound velocity and rotation vectors for wet collisions.

Quantile	Velocity vector (σ↑)	Velocity vector (σ↓)	Rotation vector (σ↑)	Rotation vector (σ↓)
25 %	0.82°	0.93°	1.55°	1.43°
50 %	1.30°	1.40°	2.51°	2.59°
75 %	2.24°	2.00°	4.39°	4.11°

CRediT authorship contribution statement

Falk Bunke: Writing – review & editing, Writing – original draft, Visualization, Validation, Software, Methodology, Investigation, Formal analysis, Data curation, Conceptualization. **Swantje Pietsch-Braune:** Supervision, Resources, Project administration, Funding acquisition, Conceptualization. **Stefan Heinrich:** Supervision, Resources, Project administration, Funding acquisition, Conceptualization.

Declaration of competing interest

The authors declare that they have no known competing financial interests or personal relationships that could have appeared to influence the work reported in this paper.

Data availability

Data will be made available on request.

Appendix

Appendix A:. Particle collision examples

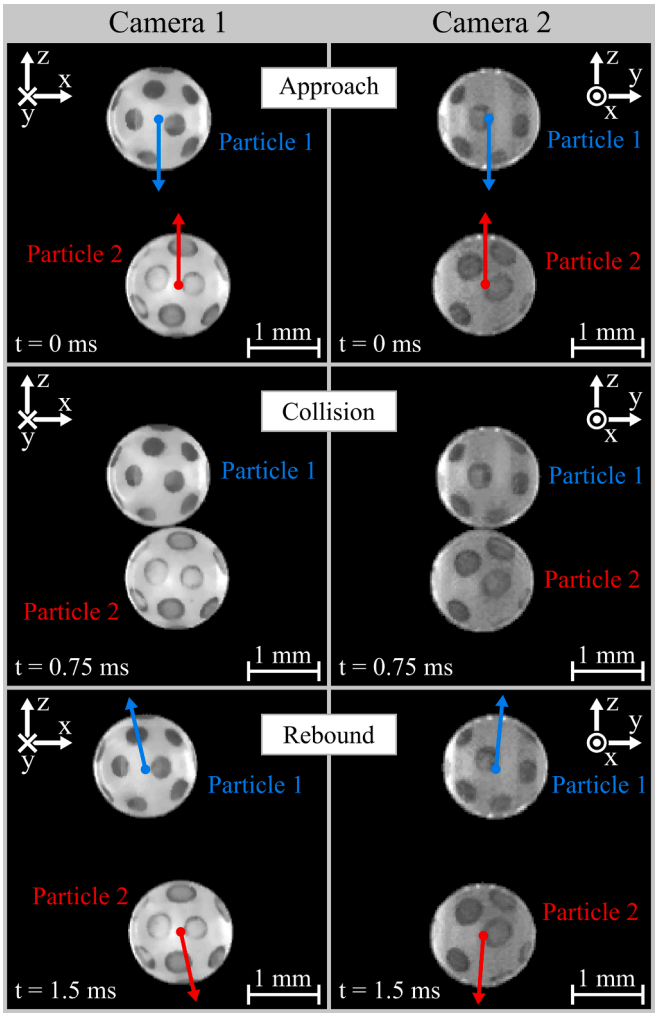

Fig. A1. Free binary collision of two spherical equal sized ZrO2 particles with a diameter of 1.5 mm out of the perspective of two perpendicular highspeed cameras.

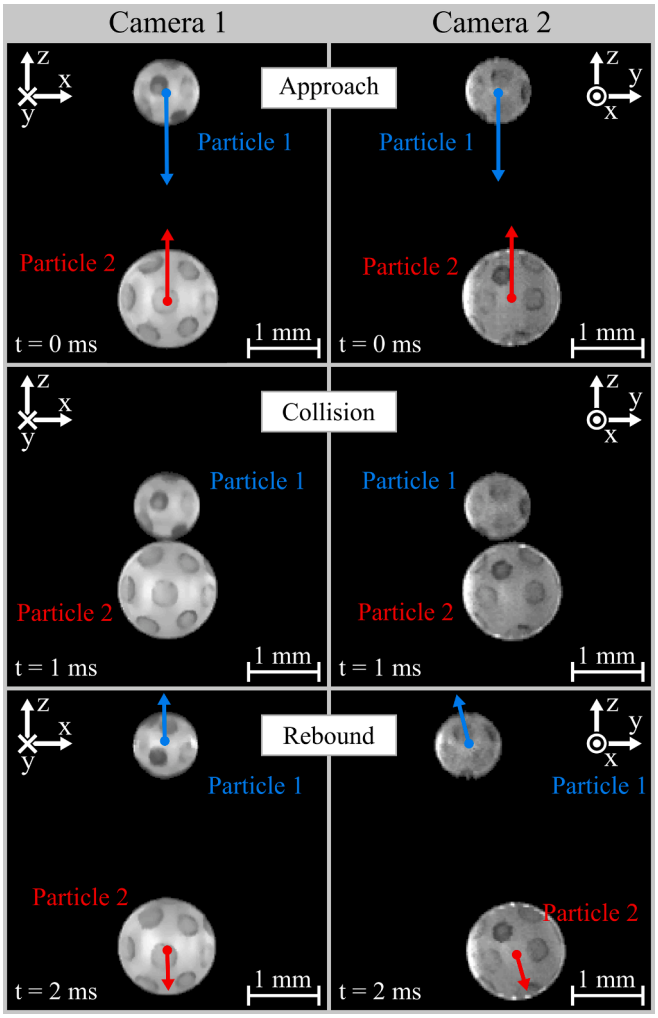

Fig. A2. Free binary collision of two spherical unequal sized ZrO2 particles with a diameter of 1 mm and 1.5 mm out of the perspective of two perpendicular highspeed cameras.

Appendix B:. Correction of rotation marker distortion caused by liquid layer onto particles

The aim of the correction is to bring the distorted rotation markers, which are detected in the images of wet particles, into the undistorted perspective. Undistorted means here first of all into the perspective, which would be present if the particle is dry. To do this, the pixels from the image of the moistened particle that represent a rotation marker are first identified. The position of each of these detected pixels will be corrected. To do this, each pixel is either moved radially to the optical center of the particle or removed entirely if it is not visible in the corrected view. The process is shown in Fig. B1.

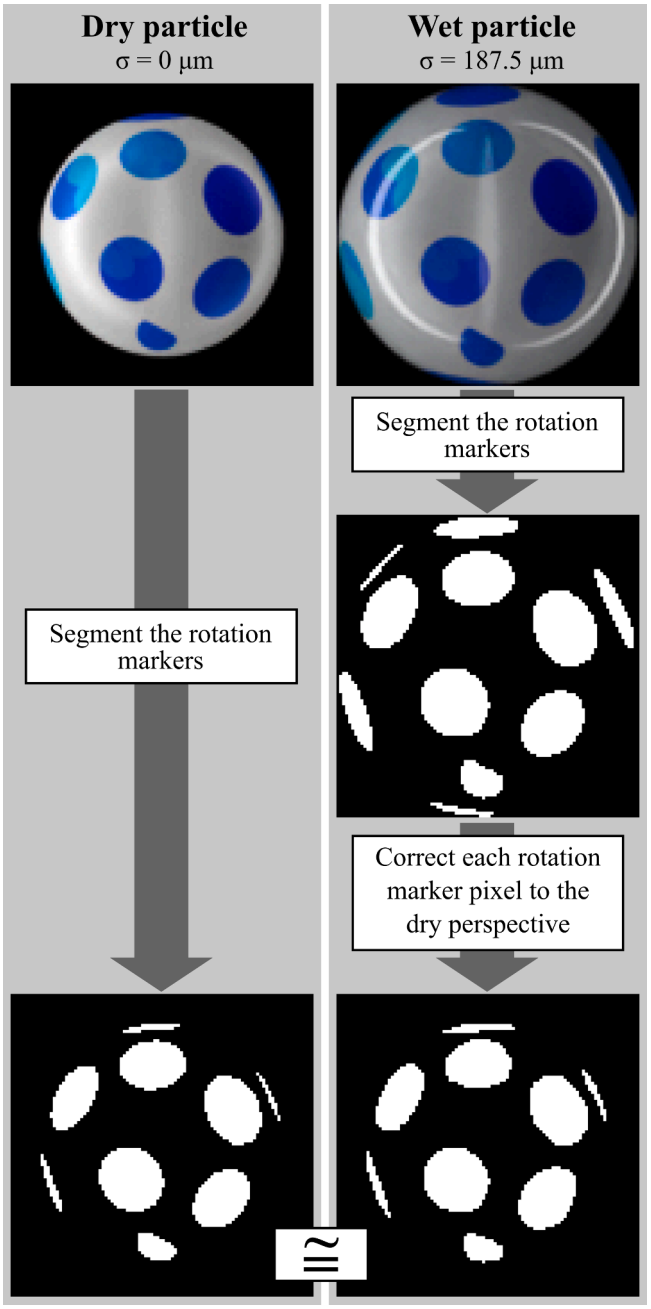

Fig. B1. Sequence of correction and comparison of final results between dry particle (left) and wet particle (right). The particle diameter is 1.5 mm, the liquid layer in the right figure corresponds to 187.5 µm. The liquid has a refractive index of 1.4.

The direct, optical comparison of the identified rotation marks between dry particle and corrected perspective from a moistened particle confirms the performance.

Fig. B2 illustrates the procedure in more detail for a single pixel. The pixel belonging to the rotation marker is shifted along the connecting line between its position $\vec{O}_1$ and the optical particle center $\vec{M}$ towards the particle center. The pixel at the previous position $\vec{O}_1$ loses its assignment and the pixel that is closest to the new coordinate $\vec{O}_2$ is labeled as a rotation marker. The new coordinate results to:

$$\vec{O}_2 = \vec{M} + (\vec{O}_1 - \vec{M}) \bullet \left(\frac{r_2}{r_1}\right). \tag{B1}$$

Thereby the radial distance between particle center and distorted pixel position r_1 can be easily determined:

$$r_1 = \left|\vec{O}_1 - \vec{M}\right|. \tag{B2}$$

The smaller, radial distance of the corrected pixel to the particle center r_2, must be calculated from the radius of the dry particle R, the liquid layer

thickness σ and the refractive index n_{liquid} of the liquid. To understand the calculation, we consider the cross-section of the particle along the radial line connecting $\vec{O}_1$ and $\vec{M}$, shown in Figure B 2 with the intersection line $A-A$.

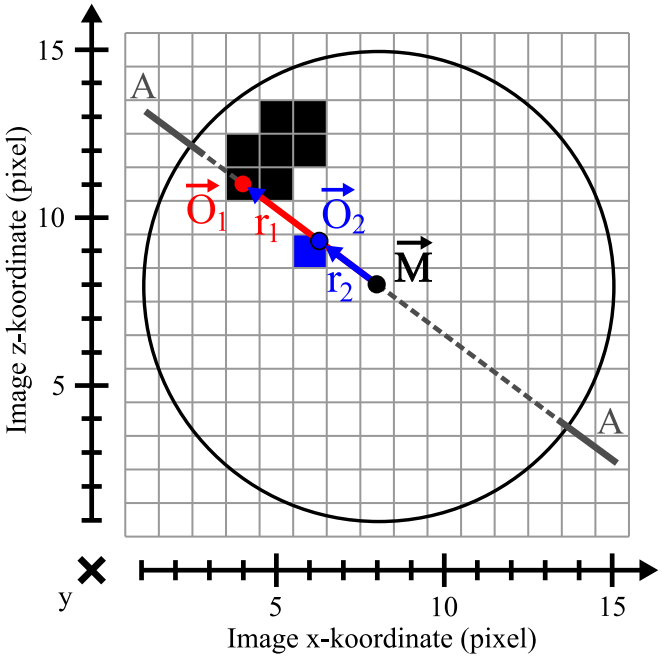

Fig. B2. Schematic camera view of a moistened particle with pixels identified as rotation markers (black). Example of correction based on one pixel. The corrected pixel assignment is shown in blue. The camera perspective represents the x-z plane, the y-corrdinate projects into the image.

Fig. B3 shows the cross section. A new, two-dimensional coordinate system is created consisting of the radial part of the pixel positions and the depth coordinate, here y, which is not visible in the camera perspective. For simplicity, the coordinate origin is placed in the particle centroid.

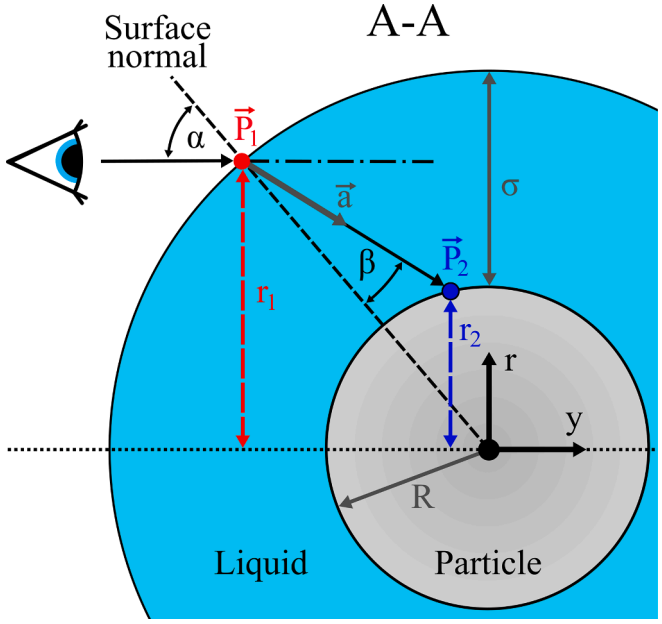

Fig. B3. Cross-sectional view along section line A-A from Fig. B2.

The camera view, represented as a visual line, runs parallel to the y-axis until it meets the liquid layer at point $\vec{P}_1$:

$$\vec{P}_1 = \begin{pmatrix} P_{1,y} \\ P_{1,r} \end{pmatrix} = \begin{pmatrix} -\cos(\alpha) \bullet (R+\sigma) \\ r_1 \end{pmatrix}, \tag{B3}$$

and forms the entrance angle α with the surface normal:

$$\alpha = arcsin\left(\frac{r_1}{R+\sigma}\right). \tag{B4}$$

The point $\overrightarrow{P}_1$ corresponds to the point $\overrightarrow{O}_1$ in the new coordinate system. According to Snell's law of refraction, the visual line is refracted at the liquid surface and emerges from the phase boundary at angle β:

$$\beta = arcsin\left(\frac{r_1}{(R+\sigma) \bullet n_{liquid}}\right). \tag{B5}$$

The resulting direction vector can be determined as follows:

$$\overrightarrow{a} = \begin{pmatrix} a_y \\ a_r \end{pmatrix} = \begin{pmatrix} \cos(\alpha-\beta) \\ -\sqrt{1-cos^2(\alpha-\beta)} \end{pmatrix}. \tag{B6}$$

With its help, the coordinates of point $\overrightarrow{P}_2$ result in:

$$\overrightarrow{P}_2 = \begin{pmatrix} P_{2,y} \\ P_{2,r} \end{pmatrix} = \begin{pmatrix} P_{2,y} \\ r_2 \end{pmatrix} = \overrightarrow{P}_1 + \lambda \bullet \overrightarrow{a}. \tag{B7}$$

The length factor λ is derived from the condition that point $\overrightarrow{P}_2$ lies on the particle contour, which is described by:

$$R^2 = {P_{2,y}}^2 + {P_{2,r}}^2. \tag{B8}$$

Combining equations (B 7) and (B 8) results in the following quadratic equation:

$$0 = \lambda^2 + \lambda \bullet p + q, \tag{B9}$$

with:

$$p = \frac{2 \bullet \left(\overrightarrow{P}_1 \bullet \overrightarrow{a}\right)}{|\overrightarrow{a}|^2}, \tag{B10}$$

and:

$$q = \frac{\left|\overrightarrow{P}_1\right|^2 - R^2}{|\overrightarrow{a}|^2}. \tag{B11}$$

λ has two potential outcomes, where the actual λ is the smaller of the two outcomes:

$$\lambda = min(\lambda_1, \lambda_2). \tag{B12}$$

Finally, from equation (B 7) r_2, but also $\overrightarrow{P}_{2,y}$ is determined, which is used as a test variable. A positive value for $\overrightarrow{P}_{2,y}$ means that the point is on the non-visible side of the particle and is only visible in the uncorrected image due to refraction in the curved liquid layer. In this case, the pixel is not corrected by shifting. The assignment of the pixel to the rotation marker is removed without replacement. Vice versa, if $\overrightarrow{P}_{2,y}$ is less than or equal to zero, the point is visible. Then the correction is made according to equation (B1).

References

[1] M.S. van Buijtenen, N.G. Deen, S. Heinrich, S. Antonyuk, J.A. Kuipers, A discrete element study of wet particle–particle interaction during granulation in a spout fluidized bed, The, Can. J. Chem. Eng. 87 (2009) 308–317, https://doi.org/10.1002/cjce.20144.

[2] S. Antonyuk, S. Heinrich, J. Tomas, N.G. Deen, M.S. van Buijtenen, J.A. M. Kuipers, Energy absorption during compression and impact of dry elastic-plastic spherical granules, Granul. Matter 12 (2010) 15–47, https://doi.org/10.1007/s10035-009-0161-3.

[3] Y.S. Cheong, M.J. Adams, A.F. Routh, M.J. Hounslow, A.D. Salman, The production of binderless granules and their mechanical characteristics, Chem. Eng. Sci. 60 (2005) 4045–4053, https://doi.org/10.1016/j.ces.2005.02.033.

[4] H. Dong, M.H. Moys, Experimental study of oblique impacts with initial spin, Powder Technol. 161 (2006) 22–31, https://doi.org/10.1016/j.powtec.2005.05.046.

[5] W. Goldsmith, Impact, Arnold, 1960.

[6] D.A. Gorham, A.H. Kharaz, The measurement of particle rebound characteristics, Powder Technol. 112 (2000) 193–202, https://doi.org/10.1016/S0032-5910(00)00293-X.

[7] D.B. Hastie, Experimental measurement of the coefficient of restitution of irregular shaped particles impacting on horizontal surfaces, Chem. Eng. Sci. 101 (2013) 828–836, https://doi.org/10.1016/j.ces.2013.07.010.

[8] S.C. Hunter, Energy absorbed by elastic waves during impact, J. Mech. Phys. Solids 5 (1957) 162–171, https://doi.org/10.1016/0022-5096(57)90002-9.

[9] A.H. Kharaz, Da Gorham, A.D. Salman, Accurate measurement of particle impact parameters, Measurement Science and Technology 10 (1999) 31. https://doi.org/10.1088/0957-0233/10/1/009.

[10] A.H. Kharaz, D.A. Gorham, A study of the restitution coefficient in elastic-plastic impact, Philos. Mag. Lett. 80 (2000) 549–559, https://doi.org/10.1080/09500830050110486.

[11] A.H. Kharaz, D.A. Gorham, A.D. Salman, An experimental study of the elastic rebound of spheres, Powder Technol. 120 (2001) 281–291, https://doi.org/10.1016/S0032-5910(01)00283-2.

[12] M.G. Koller, H. Kolsky, Waves produced by the elastic impact of spheres on thick plates, Int. J. Solids Struct. 23 (1987) 1387–1400, https://doi.org/10.1016/0020-7683(87)90004-7.

[13] T. Li, J. Zhang, W. Ge, Simple measurement of restitution coefficient of irregular particles, China Particuology 2 (2004) 274–275, https://doi.org/10.1016/S1672-2515(07)60074-8.

[14] M.Y. Louge, M.E. Adams, Anomalous behavior of normal kinematic restitution in the oblique impacts of a hard sphere on an elastoplastic plate, Phys. Rev. E 65 (2002) 21303, https://doi.org/10.1103/PhysRevE.65.021303.

[15] C. Mangwandi, Y.S. Cheong, M.J. Adams, M.J. Hounslow, A.D. Salman, The coefficient of restitution of different representative types of granules, Chem. Eng. Sci. 62 (2007) 437–450, https://doi.org/10.1016/j.ces.2006.08.063.

[16] M.C. Marinack Jr, R.E. Musgrave, C.F. Higgs III, Experimental investigations on the coefficient of restitution of single particles, Tribol. Trans. 56 (2013) 572–580, https://doi.org/10.1080/10402004.2012.748233.
[17] T. Oesau, P. Grohn, S. Pietsch-Braune, S. Antonyuk, S. Heinrich, Novel approach for measurement of restitution coefficient by magnetic particle tracking, Adv. Powder Technol. 33 (2022) 103362, https://doi.org/10.1016/j.apt.2021.11.014.
[18] C.V. Raman, On some applications of Hertz's theory of impact, Phys. Rev. 15 (1920) 277, https://doi.org/10.1103/PhysRev.15.277.
[19] J. Reed, Energy losses due to elastic wave propagation during an elastic impact, J. Phys. D Appl. Phys. 18 (1985) 2329, https://doi.org/10.1088/0022-3727/18/12/004.
[20] R. Seifried, W. Schiehlen, P. Eberhard, Numerical and experimental evaluation of the coefficient of restitution for repeated impacts, Int. J. Impact Eng 32 (2005) 508–524, https://doi.org/10.1016/j.ijimpeng.2005.01.001.
[21] F. Shaffer, H. Massah, J. Sinclair, M. Shahnam, Measurement of time-averaged particle-wall collision properties using particle tracking velocimetry, CRADA PC93-006, final report.
[22] M. Sommerfeld, N. Huber, Experimental analysis and modelling of particle-wall collisions, Int. J. Multiph. Flow 25 (1999) 1457–1489, https://doi.org/10.1016/S0301-9322(99)00047-6.
[23] R. Sondergaard, K. Chaney, C.E. Brennen, Measurements of solid spheres bouncing off flat plates 0021–8936 (1990), https://doi.org/10.1115/1.2897079.
[24] D. Tabor, A simple theory of static and dynamic hardness, Proceedings of the Royal Society of London, in: Series A. Mathematical and Physical Sciences 192, 1948, pp. 247–274, https://doi.org/10.1098/rspa.1948.0008.
[25] H. Tang, R. Song, Y. Dong, X. Song, Measurement of restitution and friction coefficients for granular particles and discrete element simulation for the tests of glass beads, Materials 12 (2019) 3170, https://doi.org/10.3390/ma12193170.
[26] J.H. Vincent, Experiments on impact, Proc. Camb. Philos. Soc. (1900) 332–357.
[27] L. Wang, W. Zhou, Z. Ding, X. Li, C. Zhang, Experimental determination of parameter effects on the coefficient of restitution of differently shaped maize in three-dimensions, Powder Technol. 284 (2015) 187–194, https://doi.org/10.1016/j.powtec.2015.06.042.
[28] I. Yardeny, D. Portnikov, H. Kalman, Experimental investigation of the coefficient of restitution of particles colliding with surfaces in air and water, Adv. Powder Technol. 31 (2020) 3747–3759, https://doi.org/10.1016/j.apt.2020.07.018.
[29] K. Yu, D. Tafti, Impact model for micrometer-sized sand particles, Powder Technol. 294 (2016) 11–21, https://doi.org/10.1016/j.powtec.2016.02.014.
[30] J. Calsamiglia, S.W. Kennedy, A. Chatterjee, A. Ruina, J.T. Jenkins, Anomalous frictional behavior in collisions of thin disks, 0021-8936 (1999). https://doi.org/10.1115/1.2789141.
[31] M. Montaine, M. Heckel, C. Kruelle, T. Schwager, T. Pöschel, Coefficient of restitution as a fluctuating quantity, Phys. Rev. E 84 (2011) 41306, https://doi.org/10.1103/PhysRevE.84.041306.
[32] F. Krull, J. Mathy, P. Breuninger, S. Antonyuk, Influence of the surface roughness on the collision behavior of fine particles in ambient fluids, Powder Technol. 392 (2021) 58–68, https://doi.org/10.1016/j.powtec.2021.06.051.
[33] T.G. Drake, Granular flow: physical experiments and their implications for microstructural theories, J. Fluid Mech. 225 (1991) 121–152, https://doi.org/10.1017/S0022112091001994.
[34] A. Lorenz, C. Tuozzolo, M.Y. Louge, Measurements of impact properties of small, nearly spherical particles, Exp. Mech. 37 (1997) 292–298, https://doi.org/10.1007/BF02317421.
[35] R. Cross, Multiple collisions of two steel balls in a Newton's cradle, Eur. J. Phys. 39 (2018) 25001, https://doi.org/10.1088/1361-6404/aa9163.
[36] C.M. Donahue, C.M. Hrenya, A.P. Zelinskaya, K.J. Nakagawa, Newton's cradle undone: Experiments and collision models for the normal collision of three solid spheres, Phys. Fluids 20 (2008), https://doi.org/10.1063/1.3020444.
[37] D.D. Durda, N. Movshovitz, D.C. Richardson, E. Asphaug, A. Morgan, A. R. Rawlings, C. Vest, Experimental determination of the coefficient of restitution for meter-scale granite spheres, Icarus 211 (2011) 849–855, https://doi.org/10.1016/j.icarus.2010.09.003.
[38] J. Hlosta, D. Žurovec, J. Rozbroj, Á. Ramírez-Gómez, J. Nečas, J. Zegzulka, Experimental determination of particle–particle restitution coefficient via double pendulum method, Chem. Eng. Res. Des. 135 (2018) 222–233, https://doi.org/10.1016/j.cherd.2018.05.016.
[39] S. Hutzler, G. Delaney, D. Weaire, F. MacLeod, Rocking Newton's cradle, Am. J. Phys 72 (2004) 1508–1516, https://doi.org/10.1119/1.1783898.
[40] G. Kuwabara, K. Kono, Restitution coefficient in a collision between two spheres, Jpn. J. Appl. Phys. 26 (1987) 1230, https://doi.org/10.1143/JJAP.26.1230.
[41] H. Minamoto, S. Kawamura, Effects of material strain rate sensitivity in low speed impact between two identical spheres, Int. J. Impact Eng 36 (2009) 680–686, https://doi.org/10.1016/j.ijimpeng.2008.10.001.
[42] A.B. Stevens, C.M. Hrenya, Comparison of soft-sphere models to measurements of collision properties during normal impacts, Powder Technol. 154 (2005) 99–109, https://doi.org/10.1016/j.powtec.2005.04.033.
[43] Y. Tatara, N. Moriwaki, Study on impact of equivalent two bodies: coefficients of restitution of spheres of brass, lead, glass, porcelain and agate, and the material properties, Bulletin of JSME 25 (1982) 631–637, https://doi.org/10.1299/jsme1958.25.631.
[44] G. Weir, S. Tallon, The coefficient of restitution for normal incident, low velocity particle impacts, Chem. Eng. Sci. 60 (2005) 3637–3647, https://doi.org/10.1016/j.ces.2005.01.040.
[45] H. Minamoto, S. Kawamura, Moderately high speed impact of two identical spheres, Int. J. Impact Eng 38 (2011) 123–129, https://doi.org/10.1016/j.ijimpeng.2010.09.005.
[46] F.W. van Name Jr, Experiment for Measuring the Coefficient of Restitution, Am. J. Phys 26 (1958) 386–388, https://doi.org/10.1119/1.1996166.
[47] R. Chandramohan, M.S. Powell, Measurement of particle interaction properties for incorporation in the discrete element method simulation, Miner. Eng. 18 (2005) 1142–1151, https://doi.org/10.1016/j.mineng.2005.06.004.
[48] S.F. Foerster, M.Y. Louge, H. Chang, K. Allia, Measurements of the collision properties of small spheres, Phys. Fluids 6 (1994) 1108–1115, https://doi.org/10.1063/1.868282.
[49] L. Labous, A.D. Rosato, R.N. Dave, Measurements of collisional properties of spheres using high-speed video analysis, Phys. Rev. E 56 (1997) 5717–5725, https://doi.org/10.1103/PhysRevE.56.5717.
[50] S. Antonyuk, S. Heinrich, N. Deen, H. Kuipers, Influence of liquid layers on energy absorption during particle impact, Particuology 7 (2009) 245–259, https://doi.org/10.1016/j.partic.2009.04.006.
[51] B. Buck, S. Heinrich, Collision dynamics of wet particles: Comparison of literature models to new experiments, Adv. Powder Technol. 30 (2019) 3241–3252, https://doi.org/10.1016/j.apt.2019.09.033.
[52] B. Buck, Y. Tang, N.G. Deen, J. Kuipers, S. Heinrich, Dynamics of wet particle–wall collisions: Influence of wetting condition, Chem. Eng. Res. Des. 135 (2018) 21–29, https://doi.org/10.1016/j.cherd.2018.05.014.
[53] B. Buck, Y. Tang, S. Heinrich, N.G. Deen, J.A. Kuipers, Collision dynamics of wet solids: rebound and rotation, Powder Technol. 316 (2017) 218–224, https://doi.org/10.1016/j.powtec.2016.12.088.
[54] B. Crüger, S. Heinrich, S. Antonyuk, N.G. Deen, J.A. Kuipers, Experimental study of oblique impact of particles on wet surfaces, Chem. Eng. Res. Des. 110 (2016) 209–219, https://doi.org/10.1016/j.cherd.2016.01.024.
[55] B. Crüger, V. Salikov, S. Heinrich, S. Antonyuk, V.S. Sutkar, N.G. Deen, J. A. Kuipers, Coefficient of restitution for particles impacting on wet surfaces: An improved experimental approach, Particuology 25 (2016) 1–9, https://doi.org/10.1016/j.partic.2015.04.002.
[56] R.H. Davis, D.A. Rager, B.T. Good, Elastohydrodynamic rebound of spheres from coated surfaces, J. Fluid Mech. 468 (2002) 107–119, https://doi.org/10.1017/S0022112002001489.
[57] F. Gollwitzer, I. Rehberg, C.A. Kruelle, K. Huang, Coefficient of restitution for wet particles, Phys. Rev. E 86 (2012) 11303, https://doi.org/10.1103/PhysRevE.86.011303.
[58] S. Hogekamp, M. Stang, H. Schubert, Jet agglomeration and dynamic adhesion forces, Chem. Eng. Process. 33 (1994) 313–318, https://doi.org/10.1016/0255-2701(94)02001-9.
[59] J. Ma, D. Liu, X. Chen, Experimental study of oblique impact between dry spheres and liquid layers, Phys. Rev. E 88 (2013) 33018, https://doi.org/10.1103/PhysRevE.88.033018.
[60] V.S. Sutkar, N.G. Deen, J.T. Padding, J.A. Kuipers, V. Salikov, B. Crüger, S. Antonyuk, S. Heinrich, A novel approach to determine wet restitution coefficients through a unified correlation and energy analysis, AIChE J 61 (2015) 769–779, https://doi.org/10.1002/aic.14693.
[61] J. Fu, M.J. Adams, G.K. Reynolds, A.D. Salman, M.J. Hounslow, Impact deformation and rebound of wet granules, Powder Technol. 140 (2004) 248–257, https://doi.org/10.1016/j.powtec.2004.01.012.
[62] P. Mueller, S. Antonyuk, M. Stasiak, J. Tomas, S. Heinrich, The normal and oblique impact of three types of wet granules, Granul. Matter 13 (2011) 455–463, https://doi.org/10.1007/s10035-011-0256-5.
[63] P. Müller, S. Antonyuk, J. Tomas, S. Heinrich, Investigations of the restitution coefficient of granules, in: Micro-Macro-interaction. In Structured media and Particle Systems, Springer, 2008, pp. 235–241.
[64] A.A. Kantak, J.E. Galvin, D.J. Wildemuth, R.H. Davis, Low-velocity collisions of particles with a dry or wet wall, Microgravity-Science and Technology 17 (2005) 18–25, https://doi.org/10.1007/BF02870971.
[65] T. Müller, F. Gollwitzer, C.A. Krülle, I. Rehberg, K. Huang, Scaling of the normal coefficient of restitution for wet impacts, in: AIP Conference Proceedings, American Institute of Physics, pp. 787–790.
[66] T. Müller, K. Huang, Influence of the liquid film thickness on the coefficient of restitution for wet particles, Phys. Rev. E 93 (2016) 42904, https://doi.org/10.1103/PhysRevE.93.042904.
[67] J. Ma, D. Liu, X. Chen, Rotational behavior of dry spheres obliquely impacting on liquid layers, Powder Technol. 270 (2015) 418–423, https://doi.org/10.1016/j.powtec.2014.08.042.
[68] R.H. Davis, A.A. Kantak, Oblique collisions and rebound of spheres from a wetted surface, J. Fluid Mech. 509 (2004) 63–81, https://doi.org/10.1017/S0022112004008900.
[69] M. Danczyk, L. Fullard, D. Holland, An investigation of collisions of liquid coated particles, in: EPJ Web of Conferences, EDP Sciences, p. 8002.
[70] C.M. Donahue, C.M. Hrenya, R.H. Davis, Stokes's cradle: Newton's cradle with liquid coating, Phys. Rev. Lett. 105 (2010) 34501, https://doi.org/10.1103/PhysRevLett.105.034501.
[71] C.M. Donahue, C.M. Hrenya, R.H. Davis, K.J. Nakagawa, A.P. Zelinskaya, G. G. Joseph, Stokes' cradle: normal three-body collisions between wetted particles, J. Fluid Mech. 650 (2010) 479–504, https://doi.org/10.1017/S0022112009993715.
[72] C.M. Donahue, W.M. Brewer, R.H. Davis, C.M. Hrenya, Agglomeration and de-agglomeration of rotating wet doublets, J. Fluid Mech. 708 (2012) 128–148, https://doi.org/10.1017/jfm.2012.297.
[73] C.M. Donahue, R.H. Davis, A.A. Kantak, C.M. Hrenya, Mechanisms for agglomeration and deagglomeration following oblique collisions of wet particles, Phys. Rev. E 86 (2012) 21303, https://doi.org/10.1103/PhysRevE.86.021303.

[74] O. Punch, M. Danczyk, M. Hawken, D.J. Holland, A comparison of pendulum experiments and discrete-element simulations of oblique collisions of wet spheres, AIChE J 69 (2023) e17989.
[75] F.-L. Yang, M.L. Hunt, Dynamics of particle-particle collisions in a viscous liquid, Phys. Fluids 18 (2006), https://doi.org/10.1063/1.2396925.
[76] O.R. Walton, Granular solids flow project: Quarterly report, January–March 1988, United States, 1988.
[77] O.R. Walton, Numerical simulation of inelastic, frictional particle-particle interactions, Particulate Two-Phase Flow 25 (1993) 884–911.
[78] Kugel Pompel, Data sheet for zirconium oxide spheres, 2023. https://www.kugelpompel.at/de/info/downloads.html (accessed 4 September 2023).
[79] Wacker-Chemie GmbH, Data sheet Wacker silicone oils, 2023. https://www.hellermanntyton.at/binaries/content/assets/downloads/at/datenblatter/01-wacker-silikone/siliconefluidsakde.pdf (accessed 4 September 2023).
[80] T.J. Atherton, D.J. Kerbyson, Size invariant circle detection, Image Vis. Comput. 17 (1999) 795–803, https://doi.org/10.1016/S0262-8856(98)00160-7.
[81] K. Hentschel, Das Brechungsgesetz in der Fassung von Snellius: Rekonstruktion seines Entdeckungspfades und eine Übersetzung seines lateinischen Manuskriptes sowie ergänzender Dokumente, Arch. Hist. Exact Sci. 55 (2001) 297–344, https://doi.org/10.1007/s004070000026.
[82] A. Trujillo-Pino, K. Krissian, M. Alemán-Flores, D. Santana-Cedrés, Accurate subpixel edge location based on partial area effect, Image Vis. Comput. 31 (2013) 72–90, https://doi.org/10.1016/j.imavis.2012.10.005.
[83] C. Ericson, Real-time collision detection, Crc Press, 2004.
[84] J. Kennedy, R. Eberhart, Particle swarm optimization, in: Proceedings of ICNN'95 - International Conference on Neural Networks, Perth, WA, Australia, IEEE, 1995, pp. 1942–1948.
[85] E. Mezura-Montes, C.A. Coello Coello, Constraint-handling in nature-inspired numerical optimization: Past, present and future, Swarm Evol. Comput. 1 (2011) 173–194, https://doi.org/10.1016/j.swevo.2011.10.001.
[86] M.E.H. Pedersen, Good parameters for particle swarm optimization, Hvass Lab, Copenhagen, Denmark, 2010, pp. 1551–3203. Tech. Rep. HL 2010,.
[87] J. Kogan, A new computationally efficient method for spacing n points on a sphere, Rose-Hulman Undergraduate Mathematics Journal 18 (2017) 5.
[88] D. Vranek, Fast and Accurate Circle-Circle and Circle-Line 3D Distance Computation, Journal of Graphics Tools 7 (2002) 23–31, https://doi.org/10.1080/10867651.2002.10487552.
[89] O. Ronneberger, P. Fischer, T. Brox, U-Net: Convolutional Networks for Biomedical Image Segmentation, in: N. Navab, J. Hornegger, W.M. Wells, A. F. Frangi (Eds.), Medical Image Computing and Computer-Assisted Intervention – MICCAI 2015, Springer International Publishing, Cham, 2015, pp. 234–241.
[90] S.K. Devalla, P.K. Renukanand, B.K. Sreedhar, G. Subramanian, L. Zhang, S. Perera, J.-M. Mari, K.S. Chin, T.A. Tun, N.G. Strouthidis, T. Aung, A.H. Thiéry, M.J.A. Girard, DRUNET: a dilated-residual U-Net deep learning network to segment optic nerve head tissues in optical coherence tomography images, Biomed, Opt. Express 9 (2018) 3244–3265, https://doi.org/10.1364/BOE.9.003244.
[91] A. Hänsch, M. Schwier, T. Gass, T. Morgas, B. Haas, V. Dicken, H. Meine, J. Klein, H.K. Hahn, Evaluation of deep learning methods for parotid gland segmentation from CT images, J. Med. Imaging 6 (2019) 11005, https://doi.org/10.1117/1.JMI.6.1.011005.
[92] V. Kumar, J.M. Webb, A. Gregory, M. Denis, D.D. Meixner, M. Bayat, D. H. Whaley, M. Fatemi, A. Alizad, Automated and real-time segmentation of suspicious breast masses using convolutional neural network, PLoS One 13 (2018) e0195816.
[93] B. Norman, V. Pedoia, S. Majumdar, Use of 2D U-Net convolutional neural networks for automated cartilage and meniscus segmentation of knee MR imaging data to determine relaxometry and morphometry, Radiology 288 (2018) 177–185, https://doi.org/10.1148/radiol.2018172322.
[94] V. Pedoia, B. Norman, S.N. Mehany, M.D. Bucknor, T.M. Link, S. Majumdar, 3D convolutional neural networks for detection and severity staging of meniscus and PFJ cartilage morphological degenerative changes in osteoarthritis and anterior cruciate ligament subjects, J. Magn. Reson. Imaging 49 (2019) 400–410, https://doi.org/10.1002/jmri.26246.
[95] Q. Zheng, H. Delingette, N. Duchateau, N. Ayache, 3-D Consistent and Robust Segmentation of Cardiac Images by Deep Learning With Spatial Propagation, IEEE Trans. Med. Imaging 37 (2018) 2137–2148, https://doi.org/10.1109/TMI.2018.2820742.
[96] Q. Tao, W. Yan, Y. Wang, E.H.M. Paiman, D.P. Shamonin, P. Garg, S. Plein, L. Huang, L. Xia, M. Sramko, Deep learning–based method for fully automatic quantification of left ventricle function from cine MR images: a multivendor, multicenter study, Radiology 290 (2019) 81–88, https://doi.org/10.1148/radiol.2018180513.
[97] G. Tong, Y. Li, H. Chen, Q. Zhang, H. Jiang, Improved U-NET network for pulmonary nodules segmentation, Optik 174 (2018) 460–469, https://doi.org/10.1016/j.ijleo.2018.08.086.
[98] F.G. Venhuizen, B. van Ginneken, B. Liefers, M.J. van Grinsven, S. Fauser, C. Hoyng, T. Theelen, C.I. Sánchez, Robust total retina thickness segmentation in optical coherence tomography images using convolutional neural networks, Biomed, Opt. Express 8 (2017) 3292–3316, https://doi.org/10.1364/BOE.8.003292.
[99] J. Wang, J. Lu, G. Qin, L. Shen, Y. Sun, H. Ying, Z. Zhang, W. Hu, A deep learning-based autosegmentation of rectal tumors in MR images, Med. Phys. 45 (2018) 2560–2564, https://doi.org/10.1002/mp.12918.
[100] R. Bernstein, Digital image processing of earth observation sensor data, IBM J. Res. Dev. 20 (1976) 40–57, https://doi.org/10.1147/rd.201.0040.
[101] S. Gite, A. Mishra, K. Kotecha, Enhanced lung image segmentation using deep learning, Neural Comput. & Applic. (2022), https://doi.org/10.1007/s00521-021-06719-8.
[102] N. Maw, J.R. Barber, J.N. Fawcett, The oblique impact of elastic spheres, Wear (1975) 101–114, https://doi.org/10.1016/0043-1648(76)90201-5.
[103] S. Luding, Granular materials under vibration: Simulations of rotating spheres, Phys. Rev. E 52 (1995) 4442, https://doi.org/10.1103/PhysRevE.52.4442.
[104] A. Santos, G.M. Kremer, V. Garzó, Energy production rates in fluid mixtures of inelastic rough hard spheres, Prog. Theor. Phys. Suppl. 184 (2010) 31–48, https://doi.org/10.1143/PTPS.184.31.
[105] D.A. Hanaor, Y. Gan, I. Einav, Static friction at fractal interfaces, Tribol. Int. 93 (2016) 229–238, https://doi.org/10.1016/j.triboint.2015.09.016.
[106] H. Hayakawa, H. Kuninaka, Theory of the inelastic impact of elastic materials, Phase Transit. 77 (2004) 889–909, https://doi.org/10.1080/01411590410001690936.
[107] H. Kuninaka, H. Hayakawa, Simulation for the oblique impact of a lattice system, J. Phys. Soc. Jpn. 72 (2003) 1655–1663, https://doi.org/10.1143/JPSJ.72.1655.
[108] H. Kuninaka, H. Hayakawa, Anomalous behavior of the coefficient of normal restitution in oblique impact, Phys. Rev. Lett. 93 (2004) 154301, https://doi.org/10.1103/PhysRevLett.93.154301.
[109] A. Glielmo, N. Gunkelmann, T. Pöschel, Coefficient of restitution of aspherical particles, Phys. Rev. E 90 (2014) 52204, https://doi.org/10.1103/PhysRevE.90.052204.
[110] K. Washino, E.L. Chan, T. Matsumoto, S. Hashino, T. Tsuji, T. Tanaka, Normal viscous force of pendular liquid bridge between two relatively moving particles, J. Colloid Interface Sci. 494 (2017) 255–265, https://doi.org/10.1016/j.jcis.2017.01.088.
[111] H.J. Cho, N.B. Lu, M.P. Howard, R.A. Adams, S.S. Datta, Crack formation and self-closing in shrinkable, granular packings, Soft Matter 15 (2019) 4689–4702, https://doi.org/10.1039/C9SM00731H.
[112] R.H. Davis, Simultaneous and sequential collisions of three wetted spheres, J. Fluid Mech. 881 (2019) 983–1009, https://doi.org/10.1017/jfm.2019.784.
[113] M. Danczyk, T. Meaclem, M. Mehdizad, D. Clarke, P. Galvosas, L. Fullard, D. Holland, Influence of contact parameters on Discrete Element method (DEM) simulations of flow from a hopper: Comparison with magnetic resonance imaging (MRI) measurements, Powder Technol. 372 (2020) 671–684, https://doi.org/10.1016/j.powtec.2020.06.002.
[114] R.C. Dorf (Ed.), The engineering handbook: Tribology: Friction, wear, and lubrication, 2nd ed., CRC Press LLC, Boca Raton, United States, 2005.
[115] G. Barnocky, R.H. Davis, Elastohydrodynamic collision and rebound of spheres: Experimental verification, Phys. Fluids 31 (1988) 1324–1329, https://doi.org/10.1063/1.866725.
[116] R.H. Davis, B.T. Good, D.A. Rager, Elastohydrodynamic rebound of spheres from coated surfaces, J. Fluid Mech. 468 (2002) 107–119, https://doi.org/10.1017/S0022112002001489.
[117] R.H. Davis, J.-M. Serayssol, E.J. Hinch, The elastohydrodynamic collision of two spheres, J. Fluid Mech. 163 (1986) 479–497, https://doi.org/10.1017/S0022112086002392.
[118] B.J. Ennis, G. Tardos, R. Pfeffer, A microlevel-based characterization of granulation phenomena, Powder Technol. 65 (1991) 257–272, https://doi.org/10.1016/0032-5910(91)80189-P.